Microwave LIGA-MEMS Variable Capacitors

A Thesis Submitted to the

College of Graduate Studies and Research

in Partial Fulfillment of the Requirements for the Degree of

Master of Science

in the Department of Electrical Engineering

University of Saskatchewan

Saskatoon, Saskatchewan

by

Darcy Haluzan

PERMISSION TO USE

In presenting this thesis in partial fulfillment of the requirements for a Postgraduate degree from the University of Saskatchewan, I agree that the Libraries of this University may make it freely available for inspection. I further agree that permission for copying of this thesis in any manner, in whole or in part, for scholarly purposes may be granted by the professor or professors who supervised my thesis work or, in their absence, by the Head of the Department or the Dean of the College in which my thesis work was done. It is understood that any copying or publication or use of this thesis or parts thereof for financial gain shall not be allowed without my written permission. It is also understood that due recognition shall be given to me and to the University of Saskatchewan in any scholarly use which may be made of any material in my thesis.

Requests for permission to copy or to make other use of material in this thesis in whole or in part should be addressed to:

Head of the Department of Electrical Engineering
University of Saskatchewan
Saskatoon, Saskatchewan, Canada
S7N 5A9

ABSTRACT

Microelectromechanical systems (MEMS) devices have been increasing in popularity for radio frequency (RF) and microwave communication systems due to the ability of MEMS devices to improve the performance of these circuits and systems. This interdisciplinary field combines the aspects of lithographic fabrication, mechanics, materials science, and RF/microwave circuit technology to produce moving structures with feature dimensions on the micron scale (micro structures). MEMS technology has been used to improve switches, varactors, and inductors to name a few specific examples. Most MEMS devices have been fabricated using planar micro fabrication techniques that are similar to current IC fabrication techniques. These techniques limit the thickness of individual layers to a few microns, and restrict the structures to have planar and not vertical features.

One micro fabrication technology that has not seen much application to microwave MEMS devices is LIGA, a German acronym for X-ray lithography, electroforming, and moulding. LIGA uses X-ray lithography to produce very tall structures (hundreds of microns) with excellent structural quality, and with lateral feature sizes smaller than a micron. These unique properties have led to an increased interest in LIGA for the development of high performance microwave devices, particularily as operating frequencies increase and physical device size decreases. Existing work using LIGA for microwave devices has concentrated on statically operating structures such as transmission lines, filters, and couplers. This research uses these unique fabrication capabilities to develop dynamically operating microwave devices with high frequency performance.

This thesis documents the design, simulation, fabrication, and testing of MEMS variable capacitors (varactors), that are suitable for fabrication using the LIGA process. Variable capacitors can be found in systems such as voltage-controlled oscil-

lators, filters, impedance matching networks and phase shifters. Important figures-of-merit for these devices include quality factor (Q), tuning range, and self-resonant frequency. The simulation results suggest that LIGA-MEMS variable capacitors are capable of high Q performance at upper microwave frequencies. Q-factors as large as 356 with a nickel device layer and 635 with a copper device layer, at operational frequency, have been simulated. The results indicate that self-resonant frequencies as large as 45 GHz are possible, with the ability to select the tuning range depending on the requirements of the application. Selected capacitors were fabricated with a shorter metal height for an initial fabrication attempt. Test results show a Q-factor of 175 and a nominal capacitance of 0.94 pF at 1 GHz. The devices could not be actuated as some seed layer metal remained beneath the cantilevers and further etching is required. As such, LIGA fabrication is shown to be a very promising technology for various dynamically operating microwave MEMS devices.

ACKNOWLEDGEMENTS

I would like to thank my supervisor, Dr. David M. Klymyshyn, for his guidance, assistance, patience, and support throughout this project.

I would also like to thank the personnel at the Institute for Microstructure Technology (IMT), Forschungszentrum Karlsruhe in Germany for making possible the fabrication of the devices. In particular, the contributions of Dr. Sven Achenbach were invaluable to the project.

I would also like to thank NSERC and TRLabs for providing financial assistance for the project. In addition, TRLabs provided personnel and research equipment that was greatly appreciated. In particular, I would like to thank Garth Wells, for his contributions to the testing of the devices.

Finally, I would like to thank my family and friends for their support throughout this research.

TABLE OF CONTENTS

LIST OF FIGURES

LIST OF TABLES

LIST OF ABBREVIATIONS

a	beam acceleration
a_n	amplitude of incident wave at the n^{th} port
A	capacitor plate area
b_n	amplitude of reflected wave at the n^{th} port
C	capacitance
CAD	computer aided design
CPW	coplanar waveguide
d	distance between plates; density
DXRL	deep X-ray lithography
E	elastic modulus; electric field intensity
EM	electromagnetic
$\acute{E}$	effective modulus
f_R	mechanical resonant frequency
f	frequency
F	force
FE	finite element
FEM	finite element method
FZK	Forschungszentrum Karlsruhe
g	acceleration due to gravity [9.81 m/s^2]
GSG	ground-signal-ground
h	beam height
H	magnetic field intensity
HF	hydrofluoric
HFSS	high frequency structure simulator

I	moment of inertia; current; identity matrix
IC	integrated circuit
IMT	Institute for Microstructure Technology
ISS	impedance standard substrate
l	beam length
LIGA	German acronym for lithografie, galvanoformung, abformung
M	beam mass
MEMS	microelectromechanical systems
MUMPS	multi-user MEMS process
n	number of ports
P	power
PMMA	polymethyl methacrylate
q_T	charge on capacitor top plate
q_B	charge on capacitor bottom plate
Q	quality factor
R	resistance
RF	radio frequency
S	scattering matrix
SEM	scanning electron microscope
SOLT	short-open-load-through
S-N	stress amplitude versus number of cycles to failure
TS	tensile strength
U	potential energy
v	Poisson's ratio
V	voltage
V_n^+	incident voltage wave at port n
V_n^-	reflected voltage wave at port n
V_{pi}	pull-in voltage
VCO	voltage-controlled oscillator
w	beam width

y_{max}	maximum beam deflection
YS	yield strength
Z	impedance
Z_{0n}	characteristic impedance (real) of the nth port
ϵ_o	permittivity of free space [8.854×10^{-12} F/m]
ϵ_r	relative permittivity
ρ	resistivity [Ω m]
μ	beam mass per unit length
μ_r	relative permeability
ω	angular frequency [rad/s]

1. INTRODUCTION

1.1 Motivation

The significant performance advantages of microwave microelectromechanical systems (MEMS) devices compared to traditional non-MEMS devices has led to an increase in attention in recent years. Examples of these devices used in radio frequency (RF) circuits include switches, variable capacitors, and inductors found in systems such as voltage-controlled oscillators (VCOs), filters, and phase shifters. They have been developed to replace their on-chip solid-state counterparts, and certain off-chip components. In the case of variable capacitors, conventional solid-state varactors are made in silicon or gallium arsenide using either p-n or Schottky-barrier junction structures. These devices have room for improvement in all figure-of-merit categories. They often suffer from a small tuning ratio (typically 30% or less), excessive resistive loss caused by large series resistance and, thus, a low quality factor (Q) (typically in the low 10s), and a low electrical self-resonance, due to large parasitics, especially when made on silicon substrates [1].

The use of MEMS devices promises high integration. This is attractive since it has the potential to reduce cost, size, and power consumption. In the case of MEMS variable capacitors, a main advantage is the potential for high Q-factors at high frequencies. At frequencies approaching X-band (8 - 12 GHz) the capacitance value required for most applications can become very small (0.1 - 0.3 pF). Passive components such as a tunable capacitor are rarely used at these high frequencies. With current technologies lumped-element approaches are abandoned for distributed-element or microwave approaches. With the miniaturization capabilities of MEMS technologies, MEMS variable capacitors have the potential to appear

lumped at frequencies into the X-band and beyond.

The LIGA (German acronym for Röntgenlithographie, Galvanoformung, Abformung - in English, X-ray lithography, electroforming and moulding) fabrication process appears to be very well suited for RF MEMS devices. The fine resolution patterning possible using LIGA allows the designer to produce very accurate structures. Combining this with the deep resist penetration of LIGA potentially allows one to design beams and gaps that are very tall and narrow. Aspect ratios on the order of 100:1 have been demonstrated. When designing variable capacitors that are electrostatically actuated, this is beneficial since actuation voltages decrease with a reduction of either the beam width or the gap size. LIGA is also not restricted to thin metal layers, as are most other MEMS processes. The use of thick metal conductors will reduce the resistance, which leads to devices with higher Q. The thick metal layers allow for a potential decrease in lateral (electrical) size due to the use of the vertical dimension for some applications including capacitors. Most current MEMS processes are based upon the use of a silicon substrate, which is lossy at higher frequencies. Since LIGA is not restricted to silicon substrates, microwave appropriate substrates can be utilized, which leads to a reduction in parasitics and leads to a higher electrical self-resonance. These strengths found in the LIGA process should lead to MEMS variable capacitors with low actuation voltages, high Q-factors, and high self-resonant frequencies.

1.2 Variable Capacitor Figures-Of-Merit

There are many different specifications that can be used to evaluate the performance of a variable capacitor. The most important electrical parameters are the unbiased nominal capacitance, tuning ratio, tuning voltage/current, equivalent series resistance or quality factor, and associated inductance or electrical self-resonance.

The unbiased nominal capacitance is the value of capacitance without the application of any tuning signal. This value depends on the requirements of the desired application and the frequency of interest. Required capacitance values for typical impedance values can range from 10 pF for applications around 100 MHz, to 0.1 pF

for applications approaching millimeter wave.

The tuning ratio is the ratio of maximum capacitance to minimum capacitance. Some applications require only a small tuning ratio to fine-tune an impedance value, most applications require a ratio of at least 2:1 [1].

For a voltage-controlled capacitor, the tuning voltage is the potential required to tune the capacitor through its entire range of values. In most cases, this voltage range is required to be as small as possible, so that it is compatible with system control signals.

The value of the equivalent series resistance determines the quality factor. The Q-factor can be expressed as

$$Q = \frac{1}{\omega CR}. \tag{1.1}$$

For an electrical reactive component the Q-factor is typically expressed as the ratio of the imaginary portion of the impedance to the real portion.

The associated parasitic inductance and the self-resonant frequency are also important device parameters. This inductance together with the tunable capacitance will resonate at a frequency known as the self-resonant frequency. At frequencies greater than this the capacitor behaves inductively. The inductance must be kept as low as possible so that the self-resonant frequency is much higher than the frequency the capacitor is intended for. As a general rule of thumb the self-resonant frequency should be at least double the operational frequency [1].

1.3 Introduction to MEMS

MEMS (microelectromechanical systems) is a name given to encompass the emerging field of microsystems. The "micro" in the name implies that the dimensions of the devices are in the micrometer scale. The "electro" infers that there is electricity or electronics involved. This aspect is usually used as a control mechanism. The "mechanical" term is used to convey the notion of movement. Using the "system" term implies the connection of smaller MEMS devices to produce a useful organization.

The development of MEMS devices followed naturally from the development of integrated circuit (IC) fabrication technologies. The performance and cost gains

achieved by miniaturizing electrical circuits has led to an interest in miniaturizing devices that rely on mechanics, optics, fluidics, etc. This drive has led to the devices and technologies that the acronym MEMS has come to encompass.

One of the major factors that has led the MEMS drive is integration. MEMS technology promises the ability to integrate mechanical devices such as certain types of sensors, with the electronics that are required to control and analyze the information from these devices. This integration of all required components onto the same substrate is beneficial from many perspectives. As with integrated circuit development, the obvious advantages are an increase in performance and a decrease in cost.

These advantages extend beyond the fields of Electrical and Mechanical Engineering. These devices have found promise in such diverse fields as biomedics, microfluidics, and optics. MEMS devices currently find success in many established products. Examples of these that have found widespread use include inkjet printer heads, microaccelerometers, and micromirrors for optical switching.

MEMS devices have many obstacles to overcome. The major problems are design, fabrication, integration, packaging, and reliability. MEMS design is challenging in that it often encompasses multiple physics domains simultaneously. The designer must find ways to analyze complex interactions between these different domains. For some of these problems computer aided design (CAD) software can be used. In most cases simulation software does not take into account all of the factors that determine the complete operation of the structure at once. Fabrication of MEMS devices is expensive and not standardized. There are many different methods that can be employed to develop a MEMS device. This is also a problem that affects integration. Integration becomes more difficult when there are multiple methods to produce structures. Packaging is an area of ongoing MEMS research due to the diversity of MEMS devices. Since these devices can be used in many different fields the packaging often needs to reflect the unique requirements of the MEMS device. Since MEMS devices contain moving parts, reliability is often a major design concern. Most MEMS materials were not historically used as structural materials

and are therefore receiving increased attention.

All true MEMS devices have one thing in common, actuation. Actuation refers to the act of affecting or transmitting mechanical motion, forces, and work by a device or system on its surroundings in response to the application of a bias voltage or current [2]. The most common types of actuators are electrostatic and thermal and examples are shown in Figure 1.1. Other types such as magnetic, piezoelectric, shape memory alloys, and hydraulic find occasional uses. They are not used more frequently due to the requirement of exotic materials, which cannot easily be incorporated into many MEMS processes.

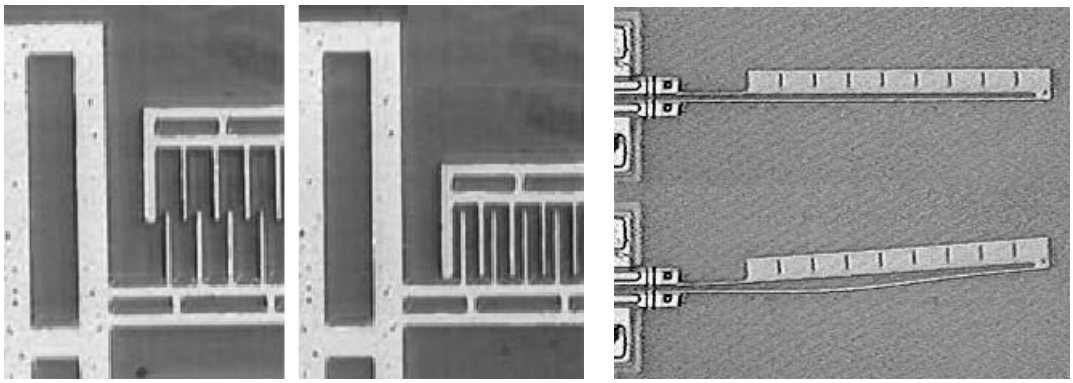

(a) Electrostatic [1] (b) Thermal [3]

Figure 1.1: Electrostatic and thermal actuators.

Electrostatic actuators have found widespread use due to their simplicity, fast response, and low power consumption. In their simplest form they are two metal structures separated by an air gap. A bias voltage is applied between the metal structures, which results in a separation of charges between them. This produces an electrostatic force that can be used to decrease the gap between the plates. An example of an electrostatic actuator is shown in Figure 1.1(a) [1].

Thermal actuators are often used because they can produce large deflections using a low voltage. The main disadvantages of thermal actuators are that they are power inefficient and react slowly, clearly not desirable qualities for RF MEMS

circuits. Thermal actuators often become quite hot which can be unfavorable from a reliability point of view. They operate on the principle of unequal expansion due to thermal heating. An example of a thermal actuator is shown in Figure 1.1(b) [3]. A current is passed through the thin and thick arms of the actuator. The thin arm will reach a higher temperature than the thick arm, which will cause it to expand more than the thick arm. This results in a displacement of the entire actuator.

1.4 Existing MEMS Variable Capacitor Designs

Most existing MEMS capacitor designs feature parallel plates, where the capacitance is varied by changing the gap between the plates [4], [5], [6]. Traditionally, these plates are limited to planar geometries and lie parallel to the substrate. These devices are constructed from layers that are typically thinner than 5 μm. They are actuated electrostatically, or thermally. Most of these devices have been fabricated using silicon-based thin film processes such as the multi-user MEMS process (MUMPS). Most planar parallel plate designs have focused on the lower end of the microwave frequency range (1 - 3 GHz) with capacitance values between approximately 1 and 4 pF.

An alternate configuration is a lateral comb structure [7], [8]. In this geometry, adjusting the overlap of the capacitor fingers changes the capacitance. The direction of actuation is perpendicular to the actuation in parallel plate type capacitors. Device layers as thick as 80 μm have been reported [8]. These layers were constructed using a highly refined deep silicon etch. Lateral comb capacitors have been targeted for frequencies in the 100 MHz to 1 GHz frequency range with capacitance values between approximately 1 and 10 pF.

MEMS parallel plate and lateral comb capacitors are designed to operate at the lower end of the microwave frequency range. A variation of the parallel plate configuration called a shunt mounted design is capable of operation at higher frequencies [9], [10]. These capacitors are capable of high Q (greater than 100) operation and are designed for the 10 - 40 GHz frequency range with capacitance values between 0.1 and 0.3 pF. In this distributed approach, coplanar waveguide (CPW)

transmission lines are used. A bridge is created over the centre conductor and the two air gaps. A change in air gap between the bridge and the centre conductor changes the capacitance.

To the author's knowledge there are no existing MEMS parallel plate or lateral comb capacitors that are designed for the 3 - 10 GHz frequency region with Q-factors greater than 100. It is believed that the use of thick metal layers and fine resolution patterning capable using the LIGA process will allow the development of capacitors to fill this void.

The following sections give examples of capacitors that are typical of the different styles mentioned above. These examples are the most commonly referenced devices in their style category.

1.4.1 Parallel Plate Configurations

In [4] the authors present an aluminum micromachined parallel-plate variable capacitor. The device is shown in Figure 1.2(a). A 1 μm thick sheet of aluminum is suspended in air approximately 1.5 μm above a bottom aluminum layer which is situated on top of a silicon substrate. The top plate is held by four mechani-

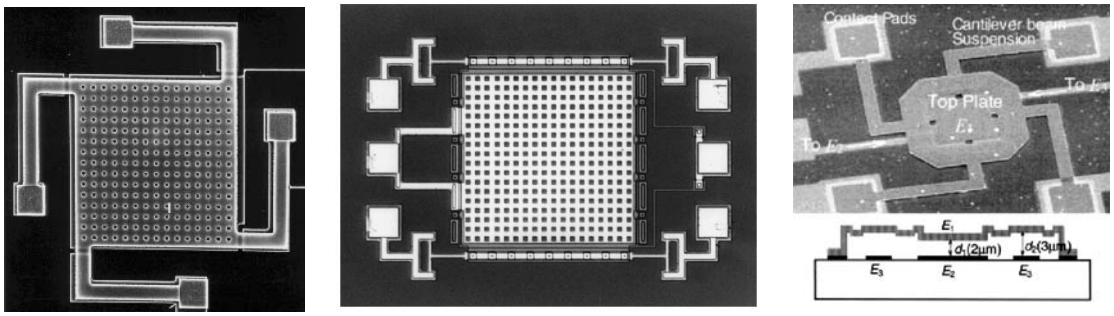

(a) Young et al. [4] (b) Dec et al. [5] (c) Jou et al. [6]

Figure 1.2: Parallel plate capacitor configurations.

cal folded-beam suspensions acting as springs. The size of the plate is 200 μm by 200 μm, with a 1.5 μm air gap, which results in a gap capacitance of approximately

200 fF. A DC bias voltage across the capacitor results in an electrostatic force, which reduces the air gap. The suspended plate can be pulled down by at most 1/3 of the original gap size before the top plate collapses onto the bottom plate. This happens because the pull-down force exceeds the mechanical restoring force. This corresponds to a theoretical 50% increase in capacitance or a 1.5:1 tuning range. Four variable capacitors were wired in parallel to achieve an 800 fF gap capacitance. The nominal capacitance is substantially larger due to fixed parasitics. With a 5.5 V tuning voltage, the capacitance can be varied between 2.11 pF and 2.46 pF. This corresponds to a tuning range of 16% or 1.16:1. At 1 GHz the series resistance is 1.2 Ω. This corresponds to a Q-factor of 62 at 1 GHz.

In [5] the authors present a three-plate tunable capacitor that has been designed using MUMPS, which is a standard polysilicon surface micromachining process as shown in Figure 1.2(b). The use of three parallel plates allows the capacitor to achieve a larger tuning range. The plate in the middle is grounded and can be pulled toward the top or bottom plate. With equal air gaps the theoretical tuning range is 2:1. The middle plate can be pulled 1/3 of the distance to the top or bottom plate. This corresponds to a maximum capacitance of 1.5 times nominal and a minimum capacitance of 0.75 times nominal. The actual air gaps used in the design are 0.75 μm for the upper gap and 1.5 μm for the lower gap. The capacitor has a plate size of 398 μm by 398 μm. With an air gap of 0.75 μm, this corresponds to a gap capacitance of 1.9 pF. With no bias voltage the measured nominal capacitance is 4.0 pF, which is due to the contribution of fixed parasitics. With a bias applied between the top plate and the middle plate the maximum achievable capacitance is 6.4 pF. With a bias between the middle plate and the bottom plate the minimum achievable capacitance is 3.4 pF. This corresponds to a measured tuning range of 87% or 1.87:1. The capacitor has a Q-factor of 15.4 at 1 GHz and 7.1 at 2 GHz, with a self-resonant frequency of approximately 6 GHz.

In [6] the authors present a variable capacitor capable of wide tuning range operation, shown in Figure 1.2(c). In this design the top plate is suspended as usual, but the bottom plate consists of two separate plates. One of the bottom plates and

the top plate form the variable capacitor, where as the other bottom plate and the top plate provide electrostatic actuation for capacitance tuning. If the capacitance gap is made smaller than the electrostatic actuation gap, the theoretical tuning range will be greater than a conventional parallel plate capacitor's tuning range of 50% or 1.5:1. A capacitor of this design can theoretically have an infinite tuning range if the capacitance gap is 1/3 or less the size of the electrostatic actuation gap. In reality the maximum achievable tuning range depends on other factors such as surface roughness and the curvature of the capacitor plates. The capacitor has a tuning range of 70% or 1.70:1, with a pull-in voltage of approximately 18 V. The difference between the measured and the theoretical value is due to parasitic capacitance. The measured Q-factor is 30 at 5 GHz and the self-resonant frequency is beyond 5 GHz.

1.4.2 Lateral Comb Configurations

In [7] the authors present a variable capacitor that is based on a lateral comb configuration and is shown in Figure 1.3(a). The device contains a central moveable structure that is electrically grounded. Fixed to this movable structure are electrodes on either side that contain comb fingers. These comb fingers on both sides mesh into a set of stationary fingers. These fingers form two tunable capacitors that are mechanically joined together. One capacitor is for tuning and the other is for RF signals. When a bias voltage is applied between the movable comb fingers and the stationary fingers of the tuning capacitor, the movable fingers are pulled towards the stationary fingers. This causes the movable fingers to be pulled away from the stationary fingers that form the RF capacitor, which leads to a decrease in capacitance. This configuration is preferred when one terminal is to be grounded, because RF chokes can be eliminated, since the tuning mechanism is electrically isolated from the RF path. The device consists of a single-crystal silicon device layer held onto a glass substrate using an epoxy adhesive layer. The silicon layer is between 20 and 30 μm thick, and the adhesive layer is 20 μm thick. A coating of aluminum on top of the silicon is used to reduce the equivalent series resistance. The

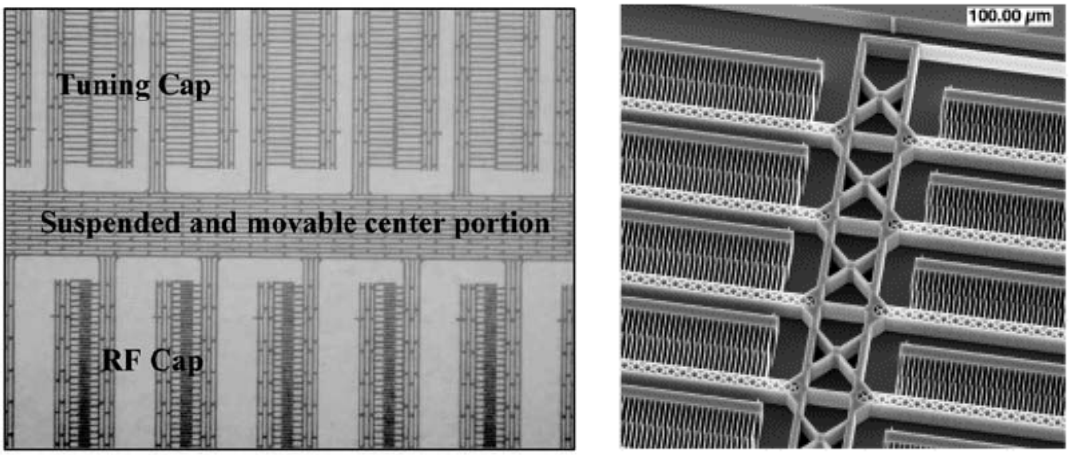

(a) Yao et al. [7] (b) Borwick et al. [8]

Figure 1.3: Lateral comb capacitor configurations.

capacitance of the device with no actuation voltage is 5.19 pF and the self resonance is 5 GHz. At 500 MHz the equivalent series resistance is 1.8 Ω, which corresponds to a Q-factor of 34. The minimum capacitance is 2.48 pF with a tuning voltage of 5 V. This corresponds to a tuning ratio of about 100% or 2:1. Interdigitated comb structure based capacitors do not have a theoretical tuning range limit.

In [8] the authors present a device that is very similar in operation to the device in [7] and is shown in Figure 1.3(b). Similar to [7] this capacitor features a thick, aluminum coated, single crystal silicon device layer suspended over a glass substrate. The previous process was improved to allow the production of thicker device layers. The device layer shown in Figure 1.3(b) is 40 μm, but layers as thick as 80 um have been produced with finger widths of 2 μm. The geometry of the device in [7] was changed to achieve a larger tuning range. In addition, both sets of stationary comb fingers are on the same side of the movable comb fingers. This results in an increase in capacitance as the bias voltage is increased. The capacitor is capable of a 740% or 8.4:1 tuning range. Although theoretically the device thickness should not affect the tuning range, the ratio of parasitic capacitance to base capacitance of the device is greatly improved with a thicker device layer. This effect has allowed the tuning ratio to be greatly increased [8]. The thicker device layer also reduced the series

resistance to less than 1 Ω. This increased the Q of the device to above 100 for frequencies up to 700 MHz and above 30 for frequencies up to 2.25 GHz.

1.4.3 Distributed Shunt Mounted Configurations

A capacitor that makes use of a parallel plate design, shunt mounted over a coplanar waveguide transmission line, is presented in [9] and is shown in Figure 1.4(a). The capacitors were developed using the silicon-MEMS foundry MUMPS process. These structures on lossy host silicon substrate were transferred to RF circuits designed on a low-loss ceramics substrate. Such a flip-chip assembly and transfer process is the key technology to assure the low-loss microwave and millimeter-wave performance [9]. The capacitor uses electro-thermal actuators to move the plate vertically

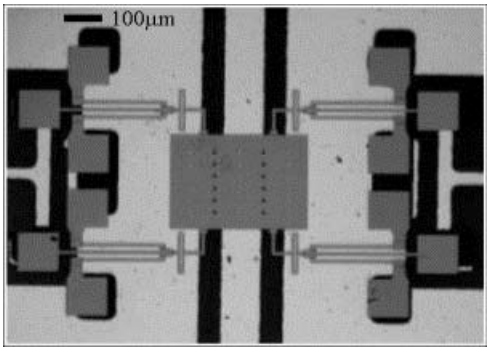

(a) Feng et al. [9]

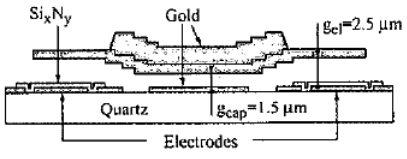

(b) Dussopt et al. [10]

Figure 1.4: Shunt mounted capacitor configurations.

to change the air gap between the plate and the CPW. The moving plate crosses over the centre conductor and gaps. The centre conductor of the 50 Ω CPW is 103 μm wide and the gaps are 48 μm. The size of the plate is 300 μm by 200 μm. The top plate is grounded through the cold arms of the actuator. The total capacitance value of the device is about 0.272 pF and the resonance frequency is above 40 GHz. The minimum Q-factor at 10 GHz was measured to be 197.

The capacitor presented in [10] also makes use of a shunt mounted design and is

shown in Figure 1.4(b). Unlike the thermally actuated capacitor in [9], this capacitor makes use of an electrostatic actuation mechanism very similar to the actuator used in [6]. It uses the principle of the actuation gap being larger than the capacitance gap to achieve an increased tuning range. In this design the capacitance area is the centre of the bridge, between the bridge and the CPW centre conductor. The two electrodes in the ground plane are used to actuate the device. The area of the plate is 140 μm by 140 μm and the gap is 1.5 μm, which leads to a gap capacitance of 116 fF. The capacitor was fabricated on a quartz substrate using an 88 Ω CPW line with dimensions of 83/133/83 μm. The capacitance values are smaller than expected due to a stress gradient in the electroplated gold which bows up the bridge, resulting in a larger air gap than expected. The capacitor has a tuning ratio of 1.46:1 over a tuning voltage of 24 V. The self-resonant frequency is 83 GHz and the Q-factor is 95-100 at 34 GHz.

1.5 LIGA Fabrication

The essential steps in the LIGA process are deep X-ray lithography (DXRL) using synchrotron radiation, followed by the electroplating of metals, followed by moulding. The acronym LIGA is derived from the German words: lithographie, galvanoformung, and abformung. In English these words are: lithography, electrodeposition, and moulding. The process was developed during the 1980's at the Nuclear Research Centre (later Research Centre Karlsruhe, Forschungszentrum Karlsruhe), in Karlsruhe, Germany, as a means to produce very small and precise separation nozzles for uranium isotopes [11], [12]. Two examples of structures fabricated using LIGA are shown in Figure 1.5 [13], [14]. The power of the LIGA process is the ability to produce very tall structures (hundreds of microns) with lateral feature sizes smaller than a micron. Structures with vertical aspect ratios greater than 100 have been realized, which is not possible using any other fabrication technique with comparable quality. The sidewalls of these tall structures are typically very vertical (greater than 89.9°) and very smooth (optical quality roughness). These unique properties have led to an interest in LIGA for the development of high performance microwave devices. Exist-

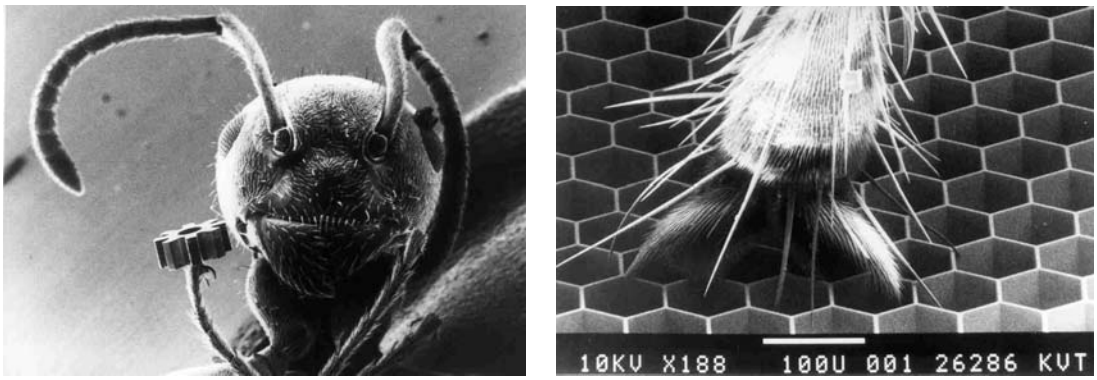

(a) Ant holding microgear [13] (b) Honeycomb structure with leg of a fly [14]

Figure 1.5: LIGA fabrication examples.

ing work using LIGA for microwave devices has concentrated on statically operating structures such as transmission lines, filters, and couplers [15], [16], [17].

In dynamically operating MEMS devices, certain entities must be free to move during actuation. In the case of variable capacitors the entity that moves is often a thin beam. If the beam is fixed along one edge it is called a cantilever beam. If it is fixed along two opposite edges it is called a fixed-fixed beam. Two possible ways a beam can be fabricated using the LIGA process are shown in Figure 1.6. In Figure 1.6(a), the cantilever beam is floating above the substrate and is fixed to a large metal piece. This can be accomplished by using the metal electroplating seed layer as a sacrificial layer. The structure shown in Figure 1.6(a) is a cantilever beam, but the sacrificial layer technique can be used to construct fixed-fixed beam structures as well. In Figure 1.6(b) one edge of the cantilever beam is attached to the substrate. This is accomplished by pre-patterning the seed layer. Fixed-fixed type beams cannot be produced using this technique.

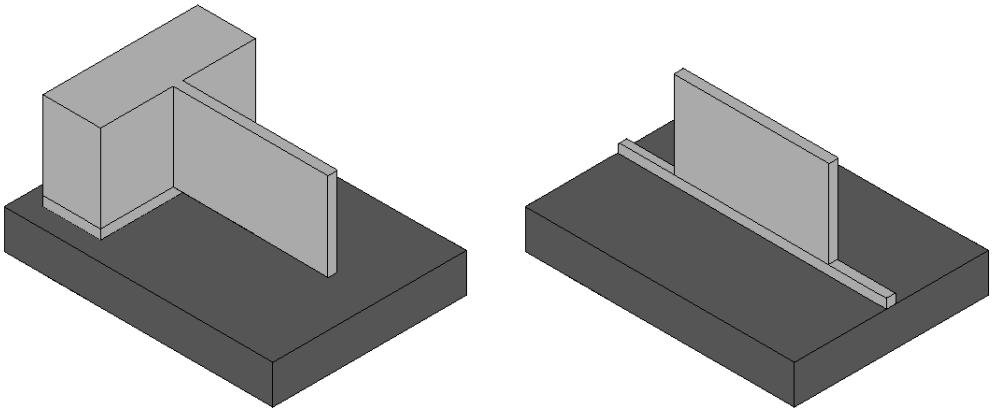

(a) Seed layer as sacrificial layer (b) Pre-patterned seed layer

Figure 1.6: LIGA beam configurations.

1.6 Objectives

The purpose of this thesis is to design, simulate and fabricate high quality, variable capacitors using the LIGA process that can be used at frequencies up to and including X-band (8 - 12 GHz). To the author's knowledge, the fabrication strengths of the LIGA process have not yet been utilized to design moving microwave MEMS devices, as current RF LIGA research has concentrated on static structures. The specific objectives of this research are:

1. Review existing MEMS variable capacitor designs and methodologies and determine if any structures or techniques are suitable for fabrication using LIGA. During this review, the fundamental design issues of MEMS devices in general will be noted.

2. Investigate a suitable actuation technique for the LIGA-MEMS variable capacitors and a method to analyze structures using this actuation technique.

3. Design variable capacitors using the actuation technique that are capable of high performance at microwave frequencies. This requires a method for analyzing the high frequency behavior of the capacitors.

4. Fabricate the capacitors, which involves creating a suitable layout of the mask for the devices.

5. Test the capacitors and determine the performance of the capacitors in all figure-of-merit categories and compare against the simulated results.

1.7 Thesis Organization

This thesis is organized into six chapters. An overview of some of the design issues regarding MEMS devices is presented in Chapter 2.

Chapter 3 is an investigation of electrostatically actuated beams. This includes a justification for their use and an examination of their operating principles. A method for analyzing these beams and an analysis of some of the more common configurations is presented.

In Chapter 4, examples of designed LIGA-MEMS variable capacitors are presented. A range of capacitors featuring various capacitance values and beam configurations are analyzed. The high frequency behavior of the devices is determined.

In Chapter 5, the steps taken in the fabrication of the capacitors are presented. In addition, the testing procedure and results are presented.

In Chapter 6, the conclusions determined from the research are presented along with suggestions for future work.

2. DESIGN ISSUES

2.1 LIGA Nickel Material Properties

The properties of a material determine how useful it will be for a particular application. Accurate material properties are essential in order to obtain accurate simulation results. These material properties determine how the simulation model will respond to a given set of imposed conditions.

The elastic modulus is a constant of proportionality that defines the linear relationship between the stress and the strain for a linearly elastic material. The stress is the force per unit area acting on the object. The strain is the elongation per unit length of the object. Poisson's ratio is the ratio of lateral strain to axial strain. The yield strength is the maximum stress that can be placed on the object before the onset of yielding (plastic deformation). The tensile strength, also called ultimate strength, is the maximum stress that can be applied to the object before fracture.

The electroplated metal most commonly used in the LIGA process is nickel. The variable capacitors will be designed and fabricated using nickel for this reason. Other metals could possibly be electroplated instead of nickel and they have their own advantages and disadvantages, but electroplating techniques for alternative metals have not been widely developed to date for LIGA. Copper, for example, has a lower resistivity and a lower elastic modulus, both of which are advantages. Copper has a lower yield strength, which is a disadvantage. Like most design decisions there are tradeoffs. The material properties of bulk nickel were taken from [18] and are listed in Table 2.1.

Some material properties of LIGA nickel were found to differ from bulk nickel [19], [20], [21]. Significant differences were found in the mechanical properties. The

Table 2.1: Material properties of bulk nickel.

Density (d) [g/cm^3]	8.902
Resistivity (ρ) [nΩ m]	68.44
Elastic Modulus (E) [GPa]	207
Poisson's Ratio (v)	0.31
Yield Strength (YS) [MPa]	59
Tensile Strength (TS) [MPa]	317

elastic modulus was found to be smaller and the yield strength and tensile strength increased over bulk nickel. This is due to the grain size of electroplated nickel being significantly smaller than that of bulk nickel [22]. Both of these findings are beneficial from a MEMS designer's perspective. The results from these findings are listed in Table 2.2.

Table 2.2: Mechanical properties of LIGA nickel.

Reference	Elastic Modulus (E) [GPa]	Yield Strength (YS) [MPa]	Tensile Strength (TS) [MPa]
Mazza [19]	202	405	782
Sharpe [20]	176	323	555
Bucheit [21]	160	277	—
Average	179	335	669

The average of these findings was used for all simulations. For the other material properties there was no discrepancy observed between bulk nickel and LIGA nickel. Therefore the values for bulk nickel will be used for these properties. A table of material properties used in simulations is shown in Table 2.3.

Table 2.3: LIGA nickel properties used in simulations.

Density (d) [g/cm^3]	8.902
Resistivity (ρ) [nΩ m]	68.44
Elastic Modulus (E) [GPa]	179
Poisson's Ratio (v)	0.31
Yield Strength (YS) [MPa]	335
Tensile Strength (TS) [MPa]	669

2.2 Beam Deflection due to Acceleration

Gravity will cause the beam to deflect. This is a potential problem if the deflection of the beam is significant. If gravity causes the capacitance to change by a significant amount then the orientation of the capacitor becomes important. This is not a desirable characteristic since this device should be able to perform adequately regardless of its physical orientation. Accelerations other than gravity will also cause the beam to deflect. The capacitor should also be able to perform under a wide range of accelerations. The device should not be limited to stationary operation. Two typical beam configurations are shown in Figure 2.1.

The cantilever beam in Figure 2.1(a) is fixed in the x-y plane at z = 0. The beam in Figure 2.1(b) is fixed in the x-y plane at z = 0 and z = l. Both beams are subject to a uniform force (F) that is caused by acceleration. The beams have length (l), width (w), and height (h). The force on the beam is determined by

$$F = Ma, \tag{2.1}$$

where M is the mass of the beam and a is the acceleration. The beam mass is

$$M = dhwl, \tag{2.2}$$

where d is the density of the beam material. The moment of inertia (I) for a beam

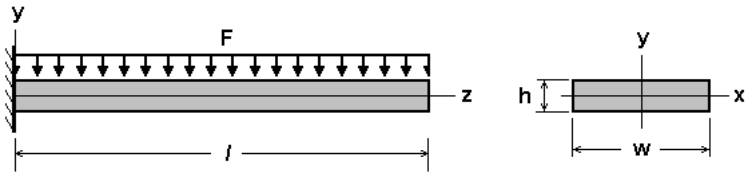

(a) Cantilever beam

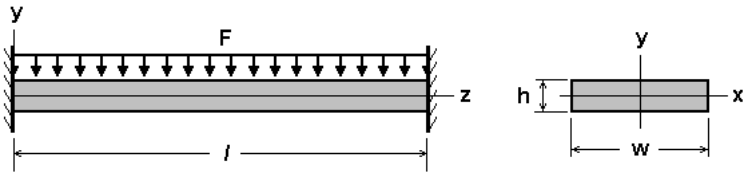

(b) Fixed-fixed beam

Figure 2.1: Beam configurations and dimensions.

with a rectangular cross section is given by [23]

$$I = \frac{wh^3}{12}. \tag{2.3}$$

Using the above equations, the maximum beam deflection can be determined. For the cantilever beam of Figure 2.1(a) the maximum deflection is [23]

$$y_{max} = \frac{-Fl^3}{8\acute{E}I}, \tag{2.4}$$

where $\acute{E}$ is the effective modulus. This deflection occurs at z = l. For the fixed-fixed beam of Figure 2.1(b) the maximum deflection is [23]

$$y_{max} = \frac{-Fl^3}{384\acute{E}I}. \tag{2.5}$$

This deflection occurs at z = $l/2$. For narrow beams ($w < 5h$), the effective modulus $\acute{E}$ is equal to Young's modulus. For wide beams ($w \geq 5h$), the effective modulus becomes the plate modulus $E/(1 - v^2)$, where v is Poisson's ratio [24].

The maximum deflections due to gravity were determined for the two beam configurations based on typical electroplated LIGA nickel material properties. The following discussion assumes that a typical LIGA beam ($h >> w$) has been oriented horizontally ($w >> h$). This would be the case if the capacitor was placed on its

side. This represents a worst case scenario and creates the maximum deflection of any orientation. The dimensions for the example are $l = 1000$ μm, $h = 6$ μm, $w = 350$ μm. The density (d) of bulk nickel is 8.902 g/cm^3. The acceleration (a) is 1 g or 9.81 m/s^2. The elastic modulus (E) is 179 GPa and Poisson's ratio (v) is 0.31. The maximum deflection for the cantilever beam structure (y_{max}) was determined to be -1.838 $\times$ 10^{-2} μm. The maximum deflection for the fixed-fixed beam structure (y_{max}) was determined to be -3.829 $\times$ 10^{-4} μm. These values are quite small, but the deflection for the cantilever beam could be significant.

Assume the beam is used as one electrode in a capacitor. The capacitor has an air gap of 3 μm, therefore the other stationary electrode is situated 3 μm below the beams in Figure 2.1. For the cantilever beam, the deflection due to gravity is 0.61% of the overall gap. The change in capacitance will be approximately 1/3 of the tip deflection, approximately 0.20%. This number could be significant depending on the application. For the fixed-fixed beam, the deflection due to gravity is 0.013% of the overall gap. The change in capacitance is approximately 0.0043%, which is not likely significant regardless of the application.

Alternatively the required acceleration can be calculated for a beam deflection of 3% (0.09 μm) of the gap. The associated change in capacitance will be approximately 1%. For the cantilever beam configuration the acceleration required is 4.9 g. For the fixed-fixed beam configuration the acceleration required is 235.1 g. In comparison, the acceleration during a space shuttle launch is 2-3 g. A fighter jet is capable of 8-9 g. The deflection of the cantilever beam can become significant during large accelerations. Accelerations capable of a significant deflection of the fixed-fixed beam are not likely to be encountered.

2.3 Stress Concerns

The stress levels present in the device during actuation must be examined. This level is important for a number of reasons. If the stress in the material is too large the device will fail. Failure can be designated as stress that exceeds the material yield strength. Beyond this, elastic deformation ceases and the material fails either

catastrophically (ceramic and glasses) or plastically (metals) [2]. If the metal deforms plastically the device will not regain its original shape once it is unloaded. This is clearly not tolerable in a MEMS device. Therefore the stress levels in the device during actuation must always be kept below the material yield strength.

In general the stress in the device during actuation should be kept at a minimum. This is important from a lifecycle perspective as well. The larger the stress in the device during actuation, the fewer number of actuation cycles the device will be able to tolerate before failure. The reliability of the device increases as the stress level during actuation decreases. The stress levels should also be reduced in areas of the device that are likely to contain tiny cracks that are formed during the fabrication of the device. These tiny cracks tend to be found in sharp corners. If the stress levels in these areas are large, failure can occur prematurely. Under a cyclic stress, components usually fail by the nucleation of a surface crack and its subsequent propagation through the component [25]. Figure 2.2 shows the fatigue curve obtained by LIGA nickel microsample fatigue tests [26].

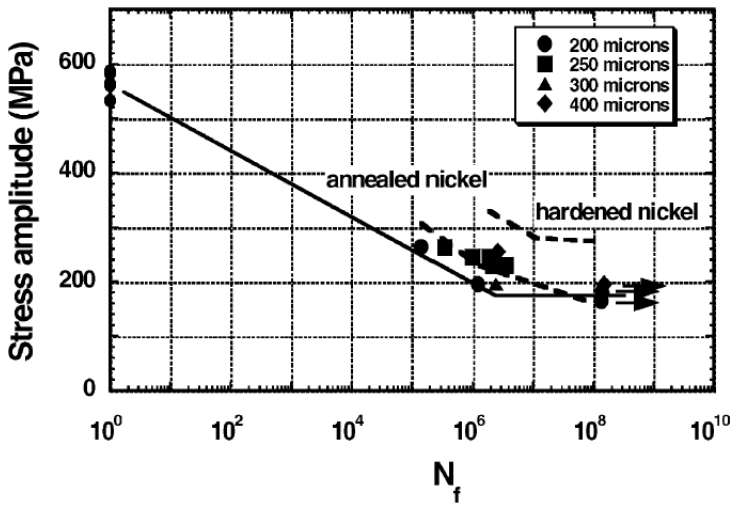

Figure 2.2: S-N curve for LIGA nickel microstructures [26].

This plot shows the stress amplitude against the number of cycles to failure, otherwise known as a S-N curve. The values shown in the legend correspond to the gage widths of the test specimens. The data for annealed nickel and hardened nickel was obtained by the author of [26] from literature values [27]. At a stress equal to the tensile strength the device fails as soon as the stress is applied. From the S-N curve we see that this is approximately 600 MPa, which is close to the tensile strength value reported in other sources and listed in Table 2.3. When the stress is less than the tensile strength it will take multiple cycles for the device to fail. An interesting feature of fatigue is that even when the stress is less than the yield strength, the material, nonetheless, still fails provided that it is cycled long enough [25]. For LIGA nickel, the yield strength is approximately 335 MPa. The S-N curve shows eventual fatigue at the yield strength as expected. Another interesting feature of the LIGA nickel S-N curve is the existence of an endurance limit. The endurance limit is the stress value at which the specimen can be cycled indefinitely and it will not fail. The endurance limit for LIGA nickel devices is 195 MPa [26]. If the MEMS device is designed to operate at a stress level below the endurance limit it can be cycled indefinitely. In the above fatigue tests, all specimens failed at a sharp corner between a beam structure and the connection piece. These observations suggest that not only the geometrical design of the MEMS structure but also the deposition conditions for LIGA nickel could have a significant effect on the fatigue life and long-term stability of the resultant MEMS structures [26].

2.3.1 Stress Levels in a Cantilever Beam

A cantilever beam was investigated during actuation to determine if the stress levels are suitable. The simulation was performed using the finite element software tool ANSYS^{TM} [28]. The geometry of the cantilever beam is shown in Figure 2.3(a), and the parameters used in the simulation are that of LIGA nickel listed previously. The overall cantilever length is 1000 μm. The cantilever width is 6 μm and the air gap between the cantilever and attracting electrode is 6 μm. The length of the attracting electrode is 925 μm.

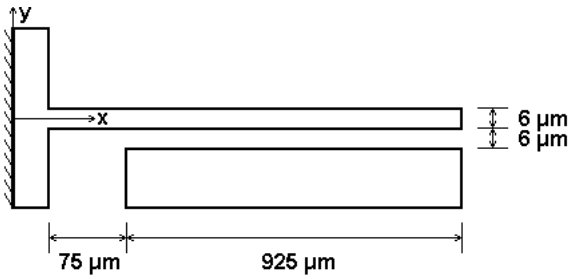

(a) Without rounded corners

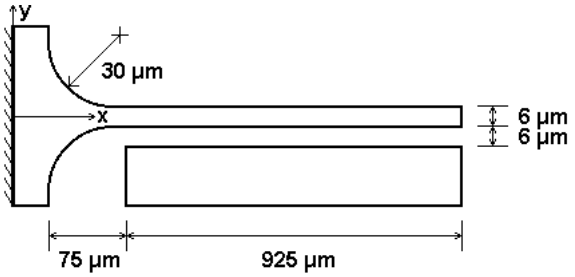

(b) With rounded corners

Figure 2.3: Stress model of a cantilever beam.

The voltage between the cantilever and the attracting electrode was increased until the deflection at the tip of the cantilever was 2 μm. Contour plots of the stress in the x-direction, y-direction, and the intensity are shown in Figure 2.4. The plots show the region where the cantilever connects to the support. This is the area of interest because the stress levels are largest here. The stress is in units of MPa.

The stress component in the x-direction is along the length of the cantilever. The maximum stress in this direction is 3.248 MPa. The stress in the x-direction decreases towards the end of the cantilever. The top edge of the cantilever is being stretched, while the bottom edge is being compressed. The middle of the cantilever in not experiencing either, therefore it is not stressed. The stress in the y-direction is concentrated in the corners where the cantilever connects to the support. The maximum stress is 1.081 MPa. This concentration of stress near a sharp corner could propagate tiny cracks produced during fabrication.

When there is more than one stress component, the components are normally

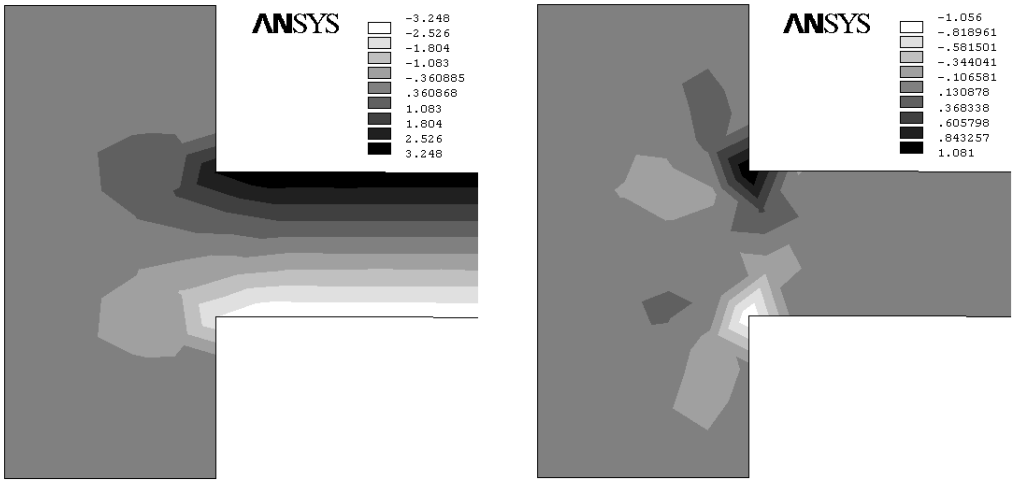

(a) X-direction

(b) Y-direction

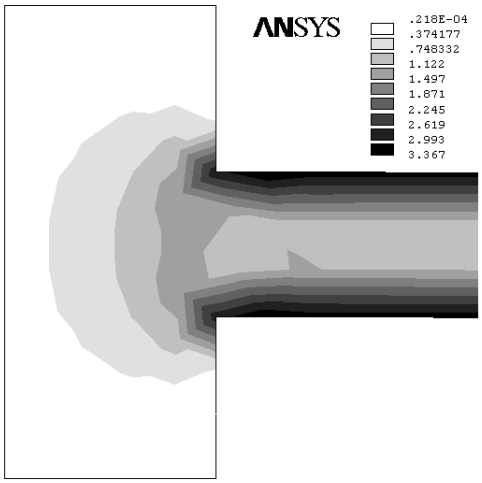

(c) Intensity

Figure 2.4: Stress components of a cantilever beam [MPa].

combined into one number to allow a comparison with an allowable valuable. ANSYS combines the stress components in the x and y directions into a value called the stress intensity. This value is derived based on the Tresca failure criterion [29]. The stress intensity is compared with the allowable value, in this case the endurance limit of 195 MPa for LIGA nickel. The maximum stress intensity in the cantilever is 3.367 MPa. This stress level is quite small. Comparing it to the endurance limit of 195 MPa for LIGA nickel it is apparent that the stress levels in this type of cantilever

structure, during small deflections, are negligible.

The structure of Figure 2.3(a) was modified to incorporate rounded corners between the cantilever and the support. The radius of the rounded corners was set to 30 μm. The modified cantilever is shown in Figure 2.3(b).

Similarly to the previous model, the voltage was increased until the deflection of the cantilever tip was 2 μm. Stress plots in the x-direction, y-direction, and intensity are shown in Figure 2.5.

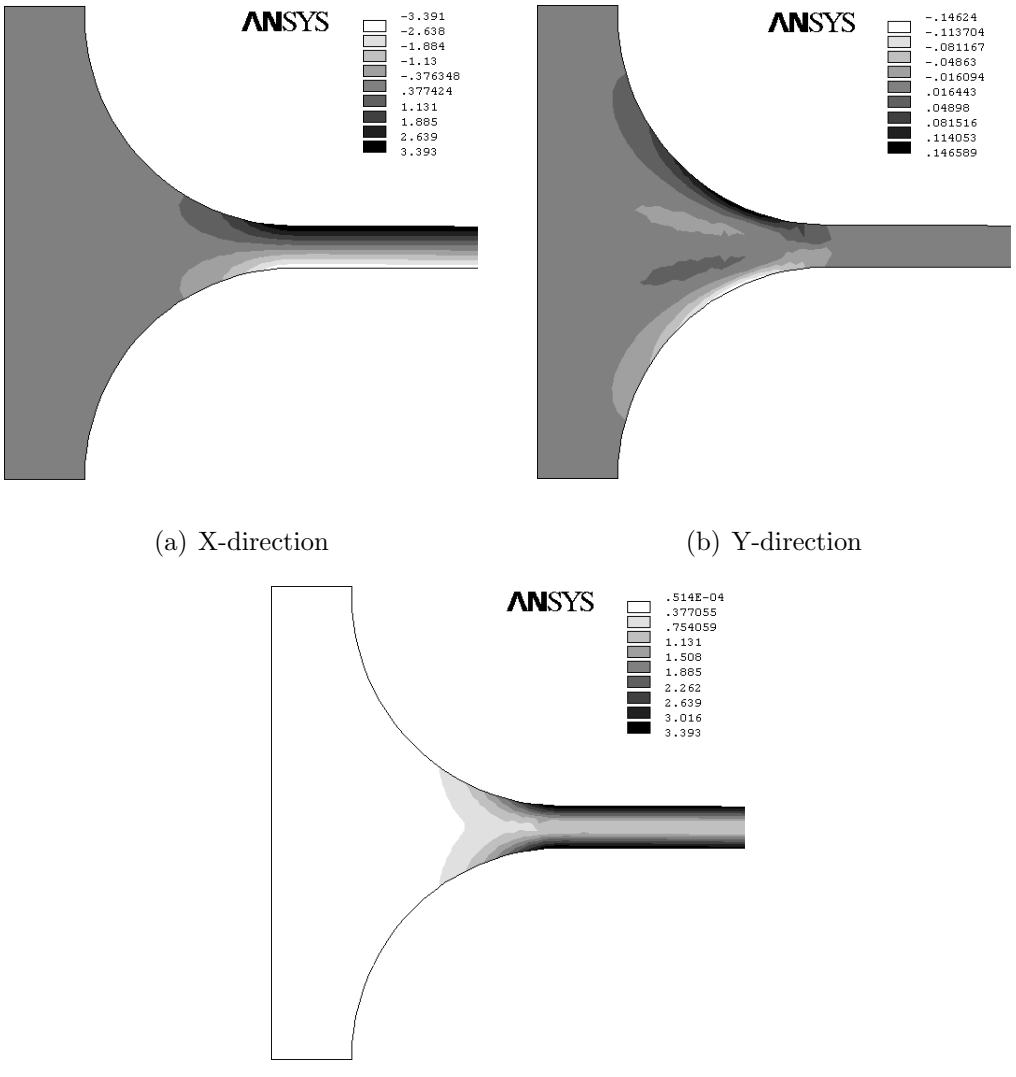

(a) X-direction

(b) Y-direction

(c) Intensity

Figure 2.5: Stress components of a cantilever beam with rounded corners [MPa].

The stress components in the x-direction are very similar to the case without rounded corners. The maximum stress is 3.393 MPa, which is slightly larger than the 3.248 MPa from the previous case. This increase in stress is due to the effective shortening of the beam. Rounding the corners with a 30 μm radius essentially reduces the length of the beam by 30 μm. For a given tip deflection, a higher stress level is expected in a shorter beam. The stress component in the y-direction is very different when the corners are rounded. The maximum stress is approximately 0.147 MPa. If this is compared to the 1.081 MPa from the previous case, the level has been reduced by a factor of approximately 7. Most importantly, there is no large stress component near a sharp corner that could propagate tiny cracks, which would cause the device to fatigue prematurely. From the stress intensity plot, the maximum stress value is 3.393 MPa. This is slightly larger than the 3.367 MPa for the cantilever without rounded corners, which is due to the effective shortening of the beam. This small increase in overall stress is justified by the reduction of stress in the y-direction.

2.3.2 Stress Levels in a Fixed-Fixed Beam

A model was created to determine the stress levels of a beam that is fixed on both ends, as shown in Figure 2.6(a). The stress levels of a fixed-fixed beam are expected to be higher than a cantilever beam, since the force required for the same displacement is much larger. The purpose is to determine if the stress levels in this type of structure are suitable for fabrication using LIGA nickel.

As before, the voltage between the beam and the attracting electrode was increased until the deflection of the beam was 2 μm. In this case the maximum deflection occurs at the centre of the beam, as opposed to the tip of the beam in the cantilever beam case. Plots of the stress in the x-direction, y-direction, and intensity are shown in Figure 2.7.

As expected the stress levels in the fixed-fixed beam are much larger than the levels found in the cantilever that is only fixed at one end. The stress levels increase by a factor of approximately 8 when both ends become fixed. Comparing the max-

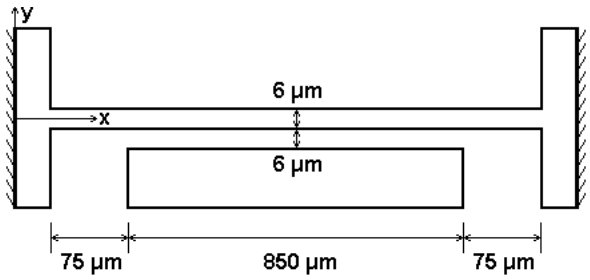

(a) Without rounded corners

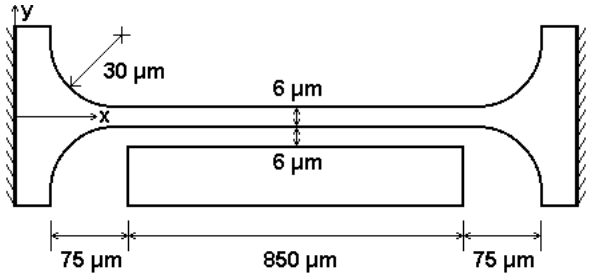

(b) With rounded corners

Figure 2.6: Stress model of a fixed-fixed beam.

imum stress intensity of 26.313 MPa to the endurance limit of 195 MPa for LIGA nickel it is apparent that this type of structure should also perform quite well during small deflections. The previous structure was modified to incorporate rounded corners and is shown in Figure 2.6(b).

Similarly to the previous model, the voltage was increased until the deflection at the centre of the beam was 2 μm. Plots of the stress in the x-direction, y-direction, and intensity are shown in Figure 2.8.

As in the previous case there is a reduction of stress in the y-direction by a factor of approximately 7. The maximum stress intensity is 28.573 MPa, which is somewhat larger than the value of 26.313 MPa for the case without rounded corners. This increase is due to the fact that the length of the beam has been effectively reduced by 60 μm. This reduction in length is larger than the cantilever beam case due to the requirement that both ends be rounded.

In all cases the stress levels were well below the 195 MPa endurance limit for

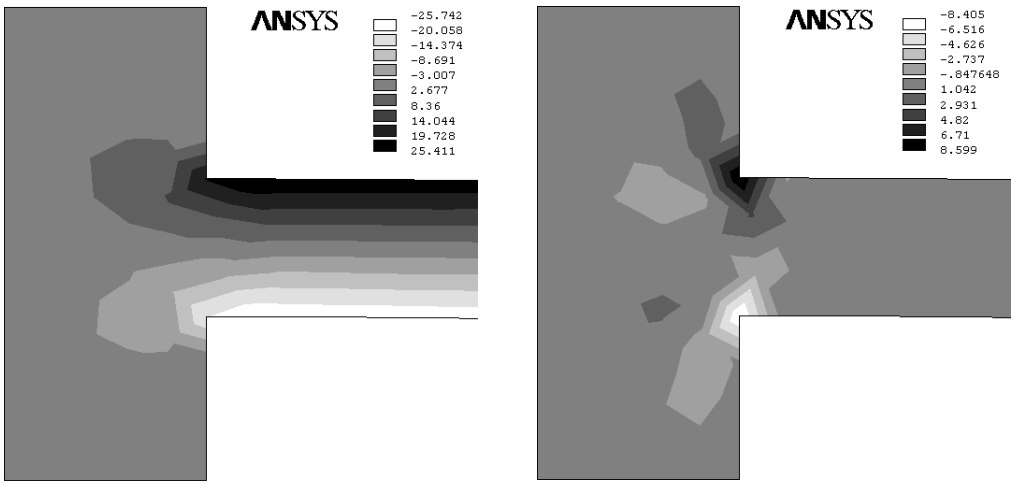

(a) X-direction (b) Y-direction

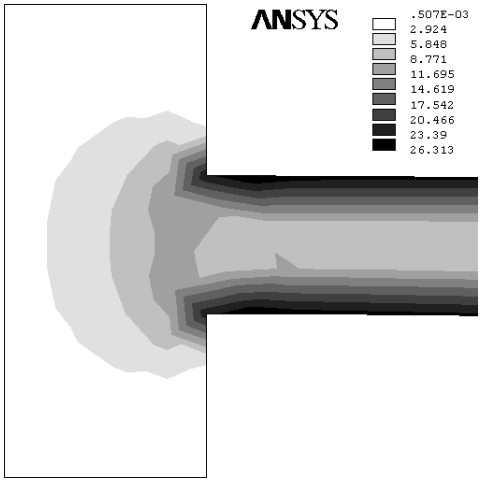

(c) Intensity

Figure 2.7: Stress components of a fixed-fixed beam [MPa].

LIGA nickel. This does not suggest that the selection of geometry for a MEMS device is arbitrary. Steps must be taken to reduce the stress levels, especially the elimination of sharp corners where tiny cracks can propagate and cause the device to fail prematurely.

In addition, the stress in the polymer resist that results due to expansion and shrinkage during development, must be taken into account. Sharp corners in the tall polymer structures will crack or possibly lift from the substrate. Therefore, there

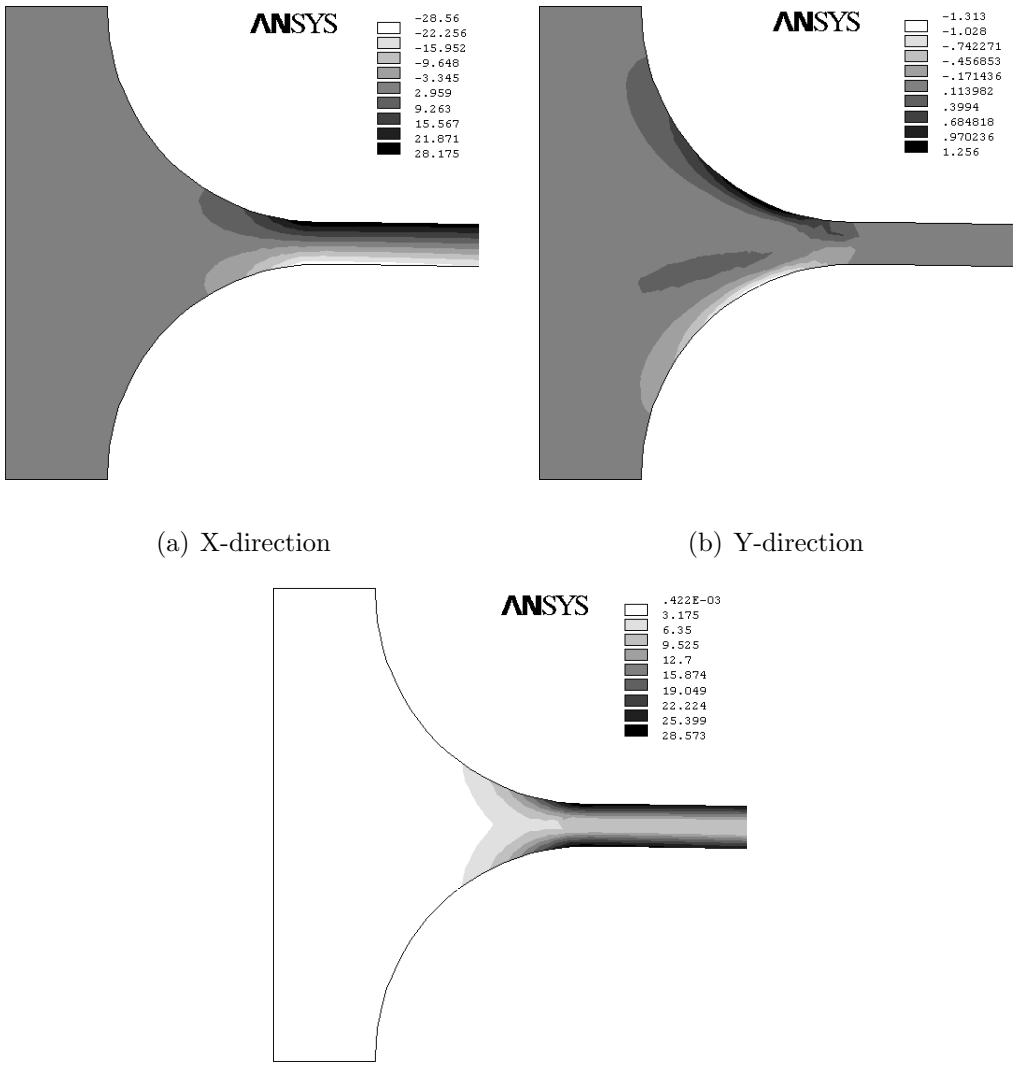

(a) X-direction

(b) Y-direction

(c) Intensity

Figure 2.8: Stress components of a fixed-fixed beam with rounded corners [MPa].

should be no sharp corners in the MEMS device at all if possible. This includes components of the MEMS device that are not involved in actuation. A rounding radius of 1 or 2 μm for static corners is usually adequate.

2.4 Breakdown of Air at Micrometer Separations

MEMS devices that feature electrostatic actuation often require large voltages applied between electrodes, which are often spaced by only a few microns. The MEMS

designer needs to know how large of a voltage can be applied, before the air between the electrodes breaks down and allows current to pass in the form of a spark.

In MEMS devices featuring micrometer separations, even a low potential difference can generate a very high electric field, leading to breakdown at low voltages. The curved line in Figure 2.9 is a Paschen Curve that theoretically relates the breakdown voltage to the separation of the electrodes. This plot is for the Paschen curve in air at atmospheric pressure. It is commonly believed that if the voltage between two electrodes in atmospheric air is below the Paschen minimum breakdown voltage of approximately 325 V, then a breakdown between the electrodes is not possible [30]. This was shown to not be the case at small separations. Data from two separate experiments Lee et al. [31] and Torres et al. [32] was compiled in [30] and is plotted in Figure 2.9.

The data reveals that for gaps greater than 4 μm the breakdown voltage is in the range of 300 - 400 V, and is consistent with Paschen's law. For gaps less than 4 μm the breakdown voltage is smaller than the values predicted by the Paschen curve and is a function of the separation of the electrodes. The two straight lines in Figure 2.9 represent the ranges of experimental data. The slopes of the two lines are 65 V/μm and 110 V/μm. The breakdown of air at micrometer separations is very similar to the breakdown of vacuum at small separations and suggests a similar breakdown mechanism may govern both cases. Since the mean free path of the electrons in air at atmospheric pressure is about 4 μm, the presence of air in very small contact gaps will only have a small effect on the breakdown process [30].

For the MEMS designer, this data reveals that one must be careful to avoid designs that require actuation voltages that are large enough to cause breakdown. During actuation of MEMS devices the gap becomes smaller as the voltage is increased. Therefore the maximum voltage and the smallest gap size are two most important parameters. From the data presented above, a value of 65 V/μm should not be exceeded to be on the safe side. This linear relationship is only valid for gaps smaller than 4 μm. For larger gaps Paschen's law provides accurate information.

The cantilever beam with rounded corners in Section 2.3.1 required a voltage of

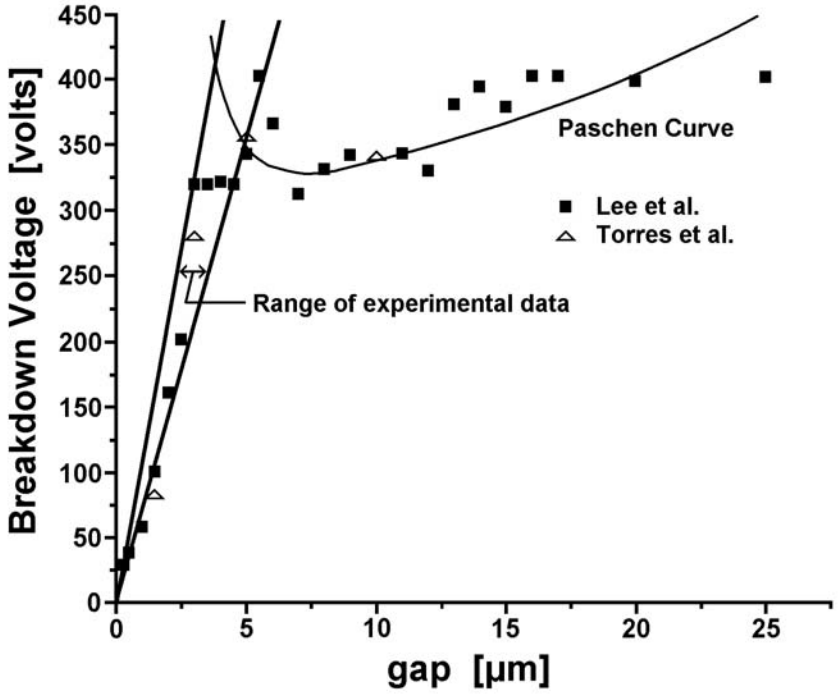

Figure 2.9: Breakdown of air at atmospheric pressure [30].

approximately 20 V for a tip deflection of 2 μm. With a tip deflection of 2 μm, the air gap at the tip would be 4 μm. This corresponds to 5 V/μm, which is significantly less than 65 V/μm. The cantilever beam without rounded corners required less voltage for a 2 μm deflection. The fixed-fixed beam with rounded corners in Section 2.3.2 required a voltage of approximately 154 V for a deflection of 2 μm. This corresponds to 38.5 V/μm, which is somewhat less than 65 V/μm. The fixed-fixed beam without rounded corners also required less voltage for a 2 μm deflection. Therefore, for these two examples, the voltage is likely not large enough to cause breakdown. In Chapter 3, a variety of beam geometries are investigated to determine the effect of changing dimensions on actuation. In many cases, during actuation, the maximum 65 V/μm is exceeded. If these geometries are to be used in practice, the beams would have to be made longer, which would reduce the required actuation voltage. Chapter 4 and Chapter 5 contains simulated and fabricated capacitors. In all cases the 65 V/μm limit has not been exceeded.

3. ELECTROSTATIC-STRUCTURAL BEAM INVESTIGATION

3.1 Background

Electrostatic beams are used as actuators in a wide variety of MEMS applications. The main principle behind their operation is deflection caused by an electrostatic force. In the case of variable capacitors, they are often used as one of the capacitor plates. This plate moves under the application of a bias voltage, which causes a change in capacitance. Electrostatic actuation is not the only actuation mechanism suitable for MEMS variable capacitors. It is definitely the most common, but other mechanisms such as thermal and electromagnetic see limited application. There are four reasons that electrostatic actuation has become so popular in MEMS design. The first reason is that it is inherently easier to design these types of actuators. Other more complicated mechanisms rely on heat transfer or magnetic interaction. The second reason is that they have comparably fast actuation rates. The actuator responds rapidly to a change in the control signal. This is a major disadvantage for thermal actuators that generally have longer actuation times due to the time needed for current induced heating. The third and possibly most important reason is that this actuator type has very low, if not zero, power consumption. This is very important from an RF MEMS point of view, where battery lifetime is a very important concern. Unlike most other actuation mechanisms, there is no current flow in an electrostatic actuator. Thermal actuators rely on current induced heating which makes them less power efficient. Thermal actuators often become quite hot which can be unfavorable from a reliability point of view. The final reason is that electrostatic actuators do not have any special material requirements. This is the major problem with electromagnetic actuators requiring magnetic components not

found in most standard manufacturing processes. Taking the above points into account, electrostatic actuation is the main candidate in the field of microwave MEMS systems.

3.2 Electrostatic-Structural Theory

Two commonly used electrostatic beam configurations are shown in Figure 3.1. These figures are two-dimensional representations of the beams. They are essentially the edges of two parallel plates running into the page. The beam in Figure 3.1(a) is a cantilever beam configuration. The cantilever (top plate) is parallel to a fixed electrode (bottom plate). The cantilever is fixed along one edge. The fixed-fixed configuration shown in Figure 3.1(b), is very similar except is has two opposite edges that are fixed. A third possibility that is sometimes seen in MEMS devices is called a membrane configuration. In this configuration all four edges of the top plate are fixed and the electrostatic force causes the maximum deflection to occur in the centre of the membrane. This method is not considered because this would require a multilevel LIGA process. It is also not desirable because actuation voltages become quite large.

The beam orientation is assumed to be perpendicular to the substrate. Vertical beams fabricated using LIGA have a beam width (w) that is much smaller than the beam height (h). The beam height is the distance the parallel plates run into the page in Figure 3.1.

Electrostatic beams are essentially parallel plate capacitors. Assuming the plates are constrained from moving, as in classic capacitors, fringing is neglected, and the dielectric is free space or air with relative permittivity ($\epsilon_r \approx 1$), the capacitance is given by

$$C = \frac{\epsilon_o A}{d}, \tag{3.1}$$

where ϵ_o is the permittivity of free space, A is the area of the plates, and d is the separation between the plates. If a voltage (V) is applied between the capacitor

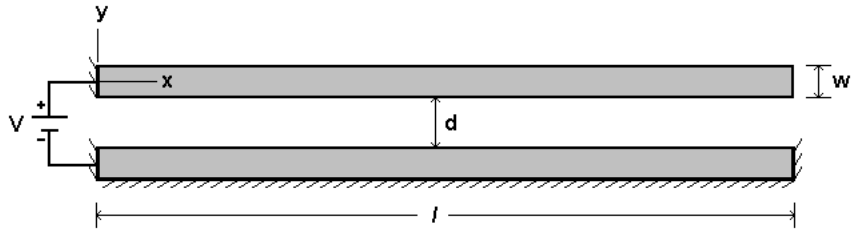

(a) Cantilever beam

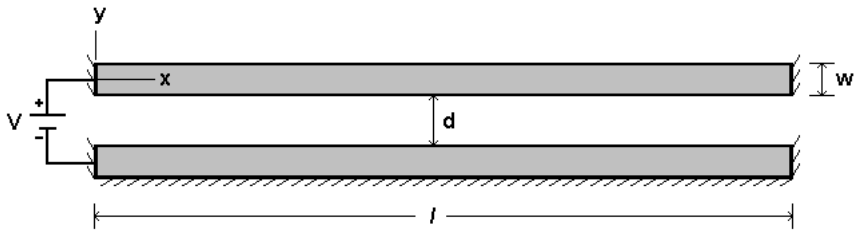

(b) Fixed-fixed beam

Figure 3.1: Electrostatic beam configurations.

plates, the potential energy of the capacitor (U) is

$$U = \frac{1}{2}CV^2. \tag{3.2}$$

This potential energy is the energy required to prevent the oppositely charged parallel plates from collapsing into each other as a result of the Coulomb force of attraction (F) [2], given by

$$F = \frac{1}{4\pi\epsilon_o}\frac{q_T q_B}{d^2}, \tag{3.3}$$

where q_T and q_B are the equal but opposite charges on the top and bottom plates respectively. This force may also be expressed as the negative of the gradient in the potential energy between the parallel plates

$$F = -\nabla U. \tag{3.4}$$

Substituting Equation 3.1 into Equation 3.2 gives

$$U = \frac{\epsilon_o A V^2}{2d}. \tag{3.5}$$

If Equation 3.5 is now substituted into Equation 3.4, the result is

$$F = \frac{\epsilon_o A V^2}{2d^2}. \tag{3.6}$$

This force is the force on either plate that is trying to pull the plates together as a result of the Coulomb force of attraction due to the separation of charges. An increase in area will cause a linear increase in force, an increase in voltage will cause a quadratic increase in force and an increase in separation distance will cause a quadratic decrease in force.

If one of the plates is configured such that it is free to move when the above force is applied then the initial gap will decrease as the applied voltage is increased. This is shown in Figure 3.2 for the two configurations mentioned previously. As the voltage is increased, the force increases, which decreases the air gap, further increasing the force. In the case of the cantilever beam, Figure 3.2(a), the force causes a maximum deflection at the tip of the cantilever. In Figure 3.2(b), the fixed-fixed beam has a maximum deflection in the middle of the beam.

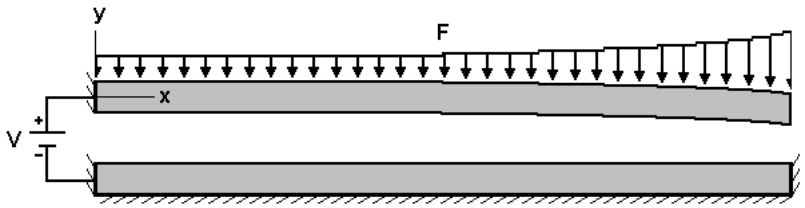

(a) Cantilever beam

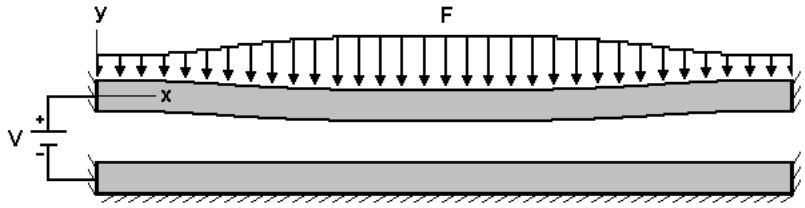

(b) Fixed-fixed beam

Figure 3.2: Electrostatic beam configurations during actuation.

For a given voltage, the deflection of the beam can be determined by solving an elastic beam equation [24]. This equation balances the electrostatic force of attraction with the mechanical restoring force. Equation 3.7 [24] is the governing

differential equation for the beams. Equation 3.7 ignores any residual stress which is sometimes present in fixed-fixed beams but not cantilever beams.

$$\acute{E}I\frac{d^4d}{dx^4} = \frac{\epsilon_o V^2 h}{2d^2}\left(1 + 0.65\frac{d}{h}\right) \tag{3.7}$$

In the above equation the moment of inertia (I) is given by $(1/12)hw^3$, where w is the width of the beam, h is the height of the beam, and $d = d(x)$ is the air gap. The factor in parenthesis on the right of the equation is a fringing field correction. For short beams ($h < 5w$), the effective modulus $\acute{E}$ is equal to Young's modulus. For tall beams ($h \geq 5w$), the effective modulus becomes the plate modulus $E/(1 - v^2)$, where v is Poisson's ratio. The above equations are typically solved using a finite difference method [24].

Solving the above equations can result in a stable or unstable solution depending on the value of the applied voltage. As the voltage is increased the beam deflects towards the bottom plate. Stable solutions are possible until the beam deflection is approximately 40% of the original gap. If the voltage is increased any further instability occurs and the beam deflects the remaining distance. This is known as pull-in, and the voltage it occurs at is the pull-in voltage V_{pi}. As the beam bends downward, the electrostatic forces become increasingly concentrated in the portion of the beam experiencing the maximum deflection. This is the tip for the cantilever beam and the centre for the fixed-fixed beam, as shown in Figure 3.2. At a particular voltage, this concentrated load causes the beam position to become unstable and it undergoes a spontaneous deflection the rest of the way [33].

By solving for beams of various sizes, a database of pull-in voltages was created, which was used to develop expressions for pull-in voltages [24]. The pull-in voltages for cantilever and fixed-fixed beams are given in Equations 3.8 and 3.9 respectively. These equations assume no residual stress is present in the beams and the air gap is much smaller than the beam height ($d << h$), which is the case for tall LIGA structures. From these equations we can see that an increase in elastic modulus, beam width, or air gap will increase the pull-in voltage, while an increase in beam length will decrease the pull-in voltage. For a given set of geometries, a fixed-fixed

beam will have a pull-in voltage that is 6.5 times larger than a cantilever beam that is fixed on only one end.

$$V_{pi} \approx 0.529\sqrt{\frac{\acute{E}w^3d^3}{\epsilon_o l^4}} \tag{3.8}$$

$$V_{pi} \approx 3.444\sqrt{\frac{\acute{E}w^3d^3}{\epsilon_o l^4}} \tag{3.9}$$

If the MEMS variable capacitor operating frequency is the same as the mechanical resonance frequency, then the variable capacitor is capable of introducing unwanted distortion at that frequency. The first mechanical resonance frequency f_R of a cantilever beam for bending oscillations is given in Equation 3.10. For a fixed-fixed beam the equation is given in 3.11 [34]. An increase in elastic modulus, or the moment of inertia will tend to increase the mechanical resonance frequency. Increasing the beam width or the beam height will increase the moment of inertia. Increasing the beam mass or length will decrease the frequency.

$$f_R = \frac{3.52}{2\pi}\sqrt{\frac{\acute{E}I}{\mu l^4}} \tag{3.10}$$

$$f_R = \frac{22.37}{2\pi}\sqrt{\frac{\acute{E}I}{\mu l^4}} \tag{3.11}$$

In the above equations μ is the mass per unit length of the beam. For typical RF MEMS variable capacitor designs, the mechanical resonant frequencies are normally at 10-100 kHz. Since the operating frequencies are at least 10000 times the mechanical bandwidth, these devices are unlikely to produce a significant amount of harmonic content [5]. This implies the RF signals will not affect the movement of the beam.

3.3 Finite Element Analysis using ANSYS

3.3.1 Motivation

MEMS devices typically fall into one of four categories [35]. The category of MEMS device to be analyzed determines what features the analysis tools require and how complex the model needs to be. Class 1 MEMS devices have no movement. Examples include micromachined static inductors and microcontainers found in MEMS fluidics devices. Strictly, these devices are not MEMS devices since they do not move, but they are micromachined and are often labeled as MEMS devices. Class 2 MEMS have movement but no contact. Examples of these types of devices are capacitors that operate in the region before pull-in, and certain thermal actuators. They can be modeled without the existence of contact surfaces, which makes analysis simpler. Class 3 MEMS have movement with contact, but no shear between surfaces. Typical devices that fall into this category are microwave MEMS switches, and capacitors that operate in the region after pull-in. These devices require contact surfaces in their models and are more complex than the previous classes. Class 4 MEMS devices require the most complex models. They have movement with contact and rubbing. An example is microgears found in gear driven MEMS systems. These devices require models that account for contact and friction. MEMS variable capacitors typically fall into classes 2 or 3 depending on their mode of operation. Therefore an analysis tool that can handle these classes of problems is required for this work.

The most accurate method to analyze coupled electrostatic-structural problems is to use full 3-D finite element (FE) simulations [36]. These solutions produce greater accuracy, but are computationally expensive. In most cases a 2-D approximation of the problem is sufficiently accurate. A 2-D approximation can only be applied if the model has constant features in one dimension. For vertical beams fabricated using LIGA, the beams must have a constant height. By analyzing beams with a range of geometries, it was found that the difference between the pull-in voltages from 2-D and 3-D simulations was no larger than 1.5% [24]. For this research this level of

error is acceptable and therefore 2-D finite element analysis is used exclusively.

There are multiple FE simulators available that are capable of performing coupled electrostatic-structural simulations. The most popular are CoventorWare^{TM} [37] and ANSYS^{TM} [28]. CoventorWare uses a coupled simulator called CoSolve-EM that was developed at the M.I.T. Microsystems Technology Laboratory. CoSolve-EM is the original coupled domain solver with published results appearing in 1995 [38]. It was created by coupling structural (ABAQUS) and electrostatic (FASTCAP) solvers that were already available. ANSYS uses a macro called ESSOLV that allows the coupling of existing separate structural and electrostatic solvers. It was shown [39] that ANSYS produces results that are virtually identical to that obtained using the CoSolve-EM simulator.

Therefore there are three apparent options to choose from when analyzing coupled electrostatic-structural problems, CoventorWare, ANSYS, or a custom developed solver. The last option would take considerable time, therefore a commercial software package was seen as the only feasible solution. It was decided that ANSYS would be used since it was already available and is becoming a popular tool for analyzing coupled physics domain FE problems.

In addition to electrostatic-structural analysis, the capacitors also require full 3-D high frequency electromagnetic (EM) analysis. Both CoventorWare and ANSYS have limited high frequency EM analysis capabilities, but another commercially available software package (Ansoft HFSS^{TM} [40]) is better suited for this class of problems. The high frequency EM analysis of the capacitors is presented in Chapter 4.

The theory of the finite element method (FEM), is not the focus of this research and therefore will not be discussed in detail. A description of the method is presented in [41], [42]. For this research commercially available software packages are used and assumed valid.

3.3.2 Description

ANSYS is a FE software package that can solve problems requiring the analysis of multiple physics domains. In the case of electrostatically actuated MEMS capacitors the two physics domains in question are the electrostatic domain and the structural domain. In order to solve an electrostatic-structural problem using ANSYS the following steps must be performed:

1. create model geometry
2. mesh the model
3. apply electrostatic constraints and write the electrostatics physics file
4. apply structural constraints and write the structural physics file
5. invoke ESSOLV macro to solve the structure
6. invoke CMATRIX macro to determine capacitance of the displaced structures

The first step is to draw the model. This includes all conductors as well as an air box that surrounds the conductors. All structural and electrostatic objects are meshed with elements. Typically, the only areas that are not meshed are conductors that cannot move. The next step is to apply electrostatic constraints. This involves applying voltages to conductors. The electrostatic elements and constraints are then written to an electrostatic physics file. Following this structural constraints are applied. This involves constraining certain areas of the structure from moving. In the case of a fixed-fixed beam, both ends of the beam are constrained. The structural elements and constraints are then written to a structural physics file. The ESSOLV macro is called to solve the coupled physics problem. This macro automates a sequential solution process. It first solves the electrostatics problem. The forces from the electrostatics problem are then applied to the structural model. The structural problem is then solved. The electrostatic mesh is then adjusted to comply with the structural solution. The macro then checks for convergence. If convergence is not met, the process repeats. Convergence of the coupled problem can

be controlled via the difference in the maximum displacement and/or the difference in electrostatic energy between iterations. Following convergence the CMATRIX macro can be used to determine the capacitance between any number of conductors in the system. CMATRIX computes the capacitance by analyzing the geometry of electrostatic (dielectric) elements.

3.3.3 Verification

To verify the simulation platform, the solution to an example problem is determined using ANSYS and the pull-in voltage is compared to the pull-in voltage predicted from Equation 3.8. The problem analyzed is a cantilever beam as shown in Figure 3.1(a). The beam material is nickel with material properties as shown in Table 2.3. The dimensions for the problem are listed in Table 3.1. This problem assumes a tall beam condition ($h \geq 5w$), and tall beams exhibit plane-strain conditions [24]. This can be handled in ANSYS by setting a key option to allow the structural elements to be modeled using plane-strain.

Table 3.1: Verification beam dimensions.

Beam Length (l)	350 μm
Beam Width (w)	3 μm
Air Gap (d)	3 μm

The 2-D cross-section model for the problem is shown in Figure 3.3. The cross-section is assumed uniform for the entire height of the structure. The narrow rectangle is the cantilever beam. The rectangle below the beam is the fixed electrode. Both conductors are enclosed in an air box.

When doing electrostatic analyses, unlike structural analyses, electric fields are typically unbounded. To accurately calculate the electric field, the effect of the open domain must be included in the electrostatic model. The model cannot extend to

Figure 3.3: Verification model geometry.

infinity and therefore must be limited in practice, while still maintaining solution accuracy. ANSYS has two methods, for 2-D models, that can be used to model the effect of open field decay. The first method is to extend the free space region, and the second is to use infinite elements. Extending the free space region is efficient in small gap models with minimal fringing. Infinite elements are efficient for large gap models with significant fringing. For 2-D models, the fringing occurs at the ends of the parallel plates. ANSYS defines a small gap to be 20 times smaller than the beam length. Since all problems encountered in this work are small gap problems, the method used is to extend the free space region. ANSYS suggests that for small gap models the free space needs to be extended approximately 2-4 times the gap size. In the above model the free space region is extended 4 times the gap size (12 μm). The outer box is given a Neumann boundary condition. This enforces that the electric field is parallel to the outer surface and equipotential lines are normal to the outer surface. The conductors within the outer box are given a Dirichlet boundary condition. This enforces that the electric field is normal to the conductor surface and equipotential lines are parallel to the conductor surface.

An enlarged view of the right side of the cantilever is shown in Figure 3.4(a). The meshed structure is shown in Figure 3.4(b). The cantilever beam is meshed using 2-D, 8-node, structural solid elements. The air region is meshed using 2-D, 6-node triangular electrostatic elements. The elements have nodes at the vertices as well as midside nodes in between the vertices. The size of the elements is specified to be 1.5 μm. ANSYS recommends using gap/2 for a coarse mesh, gap/4 for a medium mesh, and gap/6 for a fine mesh. A coarse mesh is used because the results are sufficiently accurate for verification.

The model is solved for a series of input voltages from 0 V until the solution

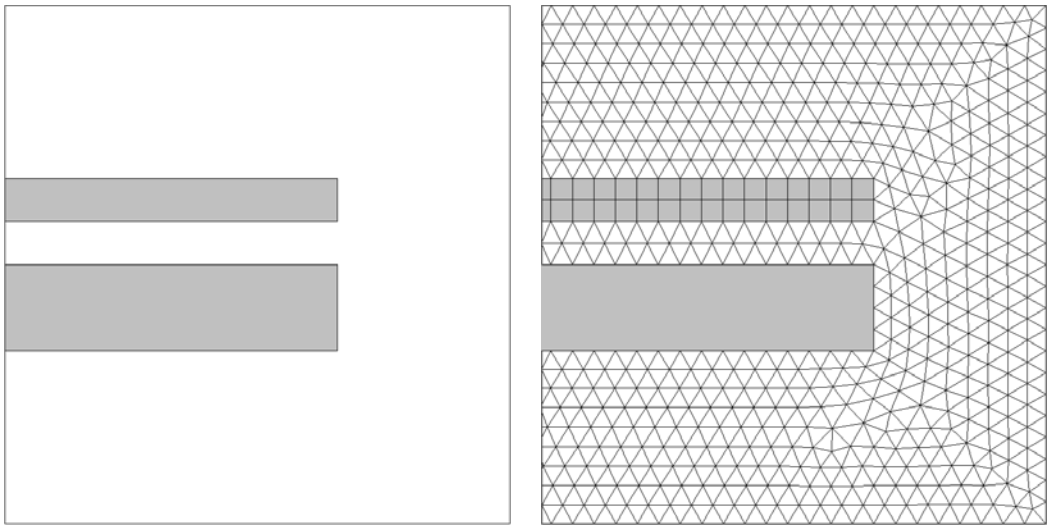

(a) Without mesh (b) With mesh

Figure 3.4: Enlarged model view.

becomes unstable which indicates pull-in. The voltage is applied to the cantilever beam and the bottom fixed plane is grounded. In this model no contact surfaces are specified, therefore the cantilever can pull right through the fixed ground plane. This is not a problem since the simulator cannot find a stable solution unless the voltage is less than the pull-in voltage. If contact is required then contact elements need to be added, which is done later on in this chapter. The results from a single voltage (17 V) simulation are presented followed by the results from the voltage sweep. This voltage is chosen since it shows large deflection because it is very close to the pull-in voltage.

Figure 3.5 shows the deflection of the cantilever upon application of a 17 V potential. The upper box shows the geometry of the undeformed cantilever. The deformed cantilever is shown directly below. The displacement of the cantilever tip is 1.01 μm. The deflection of the cantilever is magnified by a factor of 10 in Figure 3.5 so that the shape of the displacement can be easily observed. Figure 3.6 shows the deflection of the cantilever tip, where the electrostatic mesh has been morphed to coincide with the deflection of the cantilever. The elements between the plates have become smaller as the gap between the plates has decreased.

Figure 3.5: Cantilever displacement.

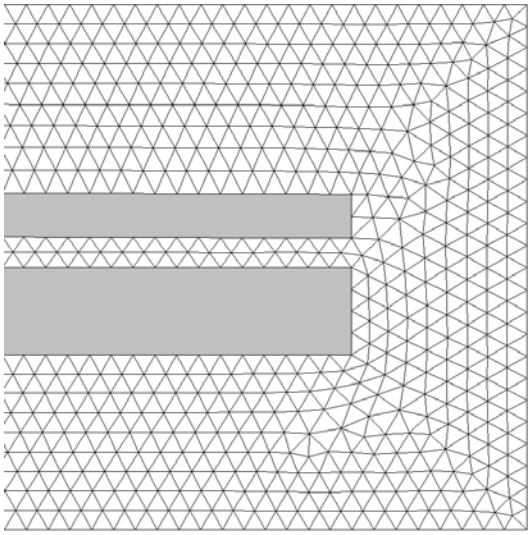

Figure 3.6: Morphed electrostatic mesh.

Figure 3.7 shows the force of the cantilever along the cantilever length. The length of the arrow corresponds linearly to the magnitude of the force. As expected the force is greatest at the tip of the cantilever that is experiencing the maximum deflection.

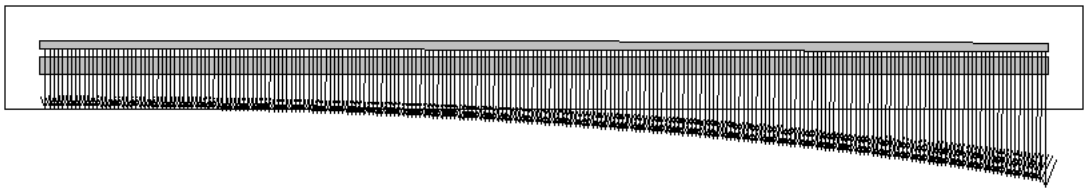

Figure 3.7: Force on cantilever beam.

Figure 3.8 shows the voltage contours surrounding the deformed cantilever. The cantilever is at a potential of 17 V as expected and the fixed ground plane is at a

potential of 0 V. Figure 3.9(a) is a contour plot of the electric field intensity. As expected the magnitude is the largest in the gap with fringing fields having increasingly smaller magnitudes. The maximum field is 8.54 V/μm. This is consistent with a 1.99 μm gap with 17 V across it. Figure 3.9(b) is a vector plot of the electric field. The vector magnitude is a linear function. The direction of the field is from the top plate (17 V) to the bottom plate (0 V).

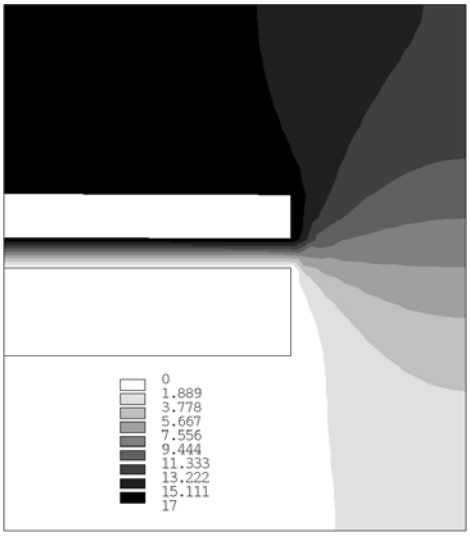

Figure 3.8: Voltage contours.

The voltage is varied from 0 V until the pull-in voltage is obtained. At pull-in the solution becomes unstable and the simulator cannot produce a solution. Figure 3.10 is a plot of the tip deflection versus the applied voltage and Figure 3.11 is a plot of the capacitance versus the applied voltage. The capacitance values given by ANSYS have units of pF/μm. This is equivalent to having a beam with a height of 1 μm. These values are quite small and have been scaled by a factor of 1000 in Figure 3.11. This is equivalent to having a beam with a height of 1000 μm. Any scale factor could have been used and the results are applicable as long as the plane-strain conditions are met ($h \geq 5w$). All capacitance plots in this chapter have been scaled by this factor.

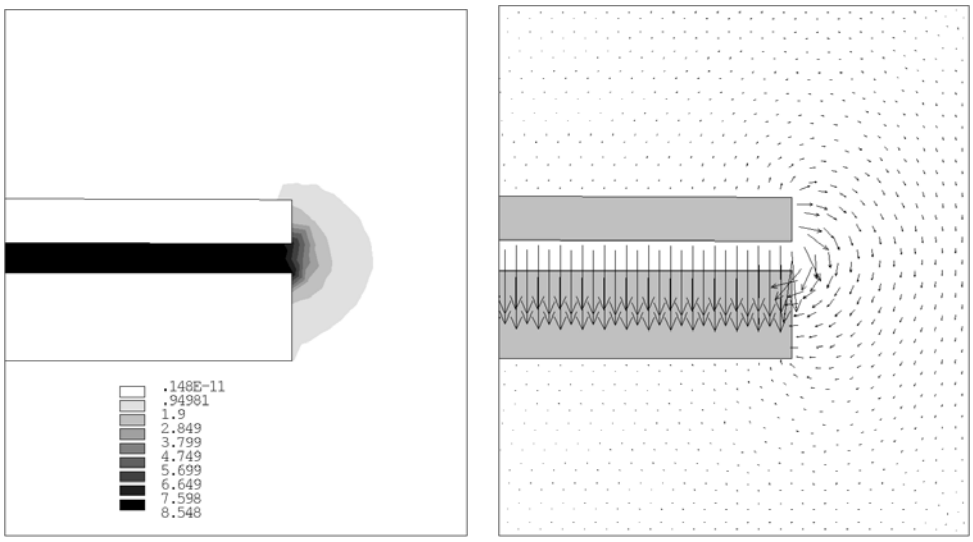

(a) Intensity contours (b) Vector plot

Figure 3.9: Electric field.

The maximum deflection of the cantilever tip was 1.31 μm at a voltage of 17.5 V. This corresponds to a 43% tip deflection of the original gap. The simulation found a solution for the beam with an applied voltage of 17.5 V, but could not converge on a solution with an applied voltage of 17.6 V. This indicates that the pull-in voltage of the beam is between these two voltages. The initial capacitance of the beam is 1.05 pF with an applied voltage of 0 V. The maximum capacitance is 1.30 pF with a voltage of 17.5 V. This corresponds to a capacitance ratio of 1.24:1. Using the simple parallel plate capacitor formula, Equation 3.1, the capacitance for this structure is 1.03 pF. This is very close (1.6% difference) to the original capacitance calculated by the simulator. The theoretical value is slightly smaller because it neglects fringing which the simulator takes into account. However, the values are close enough to give confidence in the validity of the simulator. The pull-in voltage, based on the approximation in Equation 3.8, was found to be 17.44 V. This is within 0.3% (best case) and 0.9% (worst case) of the result obtained from the simulator (17.5 V - 17.6 V).

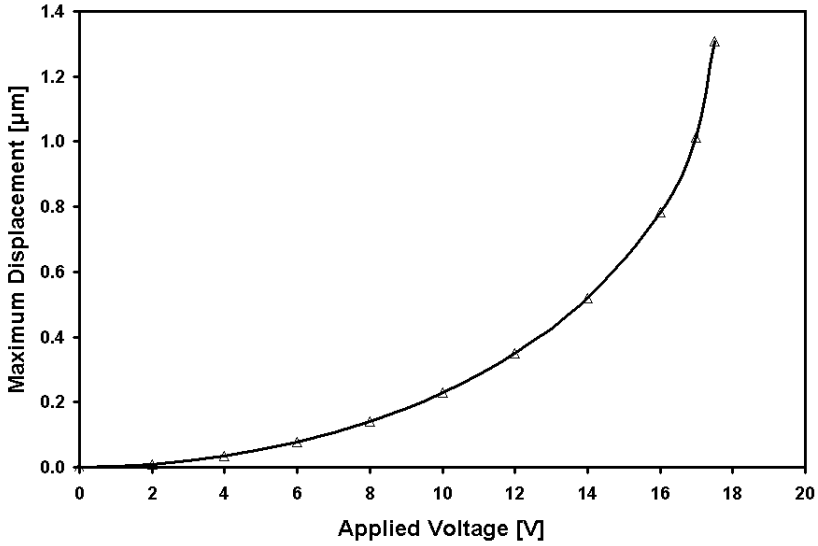

Figure 3.10: Tip deflection of verification beam.

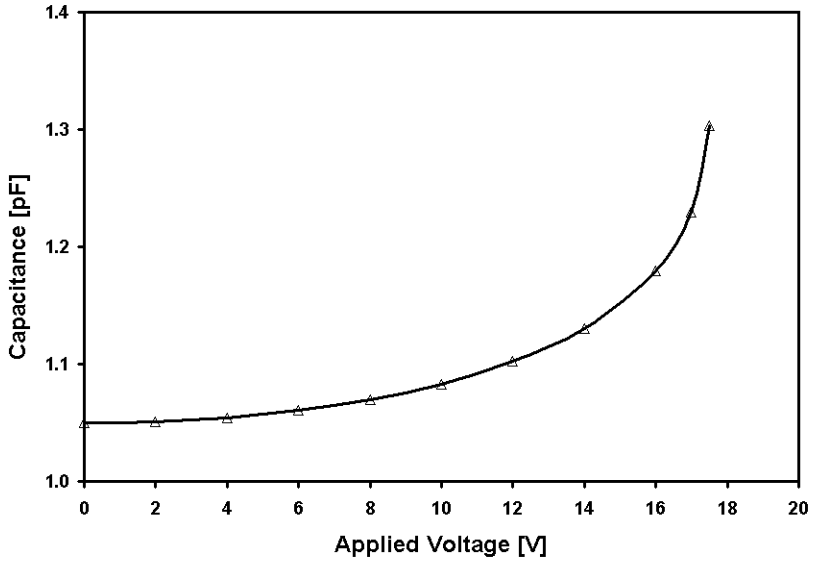

Figure 3.11: Capacitance of verification beam.

3.4 Two-Plate Capacitor Investigation

3.4.1 Cantilever Beams

The two-plate capacitors (Figure 3.1(a)) listed in Table 3.2 are analyzed next to determine the effect of changing various dimensions. The first capacitor in the table is the capacitor presented in the previous verification. The other three capacitors have one dimension that has been changed from the verification capacitor.

Table 3.2: Two-plate cantilever beam capacitor dimensions.

Dimension Set	1	2	3	4
Beam Length (l) [μm]	350	350	350	500
Beam Width (w) [μm]	3	3	4	3
Air Gap (d) [μm]	3	4	3	3

The maximum displacement (tip deflection) of the capacitors is shown in Figure 3.12. Set 1, 3, and 4 all have a maximum deflection of approximately 1.31 μm. This is expected since they have the same 3 μm air gap. Set 2 has a maximum deflection of approximately 1.70 μm. The larger deflection is a result of the larger air gap. In all cases the tip deflects approximately 43% of the original gap before pull-in. The pull-in voltage for Set 2 and 3 was determined to be between 26.9 V and 27.0 V. The pull-in voltage from Equation 3.8 is 26.84 V, which agrees quite well. The pull-in voltage of Set 4 was between 8.5 V and 8.6 V. The pull-in voltage is lower than other capacitors because the beam is longer. The pull in voltage from Equation 3.8 is 8.54 V, which is very close.

The capacitance of the four capacitors is shown in Figure 3.13. Set 1 and 3 have the same initial (1.05 pF) and final (1.30 pF) capacitance, as expected since they have the same air gap and beam length. The capacitance ratio for these two capacitors is 1.24:1. Set 2 has a smaller initial (0.79 pF) and smaller final (0.98 pF)

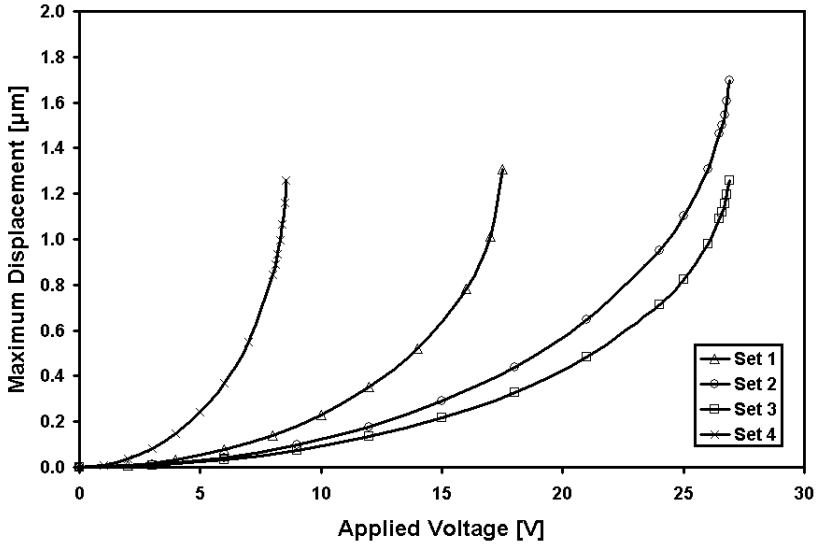

Figure 3.12: Beam deflection of cantilever beam two-plate capacitors.

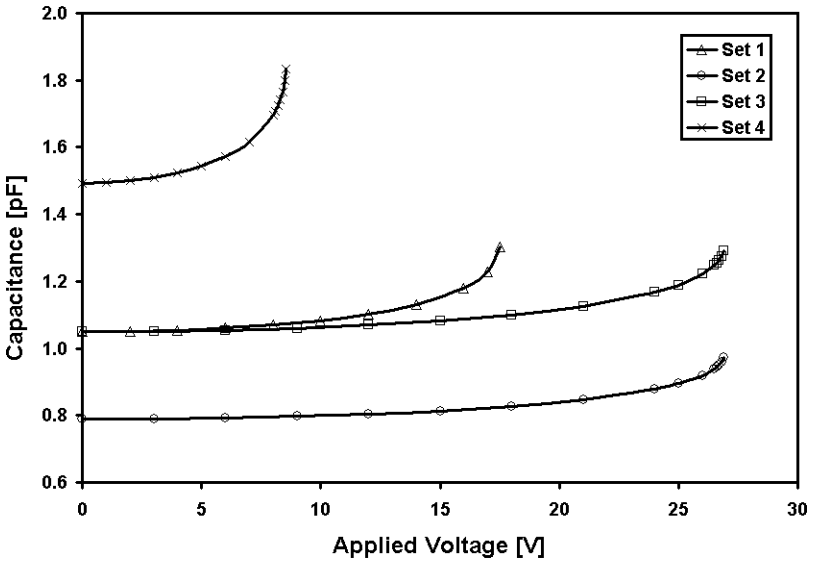

Figure 3.13: Capacitance of cantilever beam two-plate capacitors.

capacitance, since the air gap is larger. The capacitance ratio for this capacitor is also 1.24:1. Set 4 has a larger initial (1.49 pF) and larger final (1.85 pF) capacitance, since the beam length is larger. The capacitance ratio for this capacitor is also 1.24:1.

The above results suggest that all two-plate capacitors with one fixed edge will have a maximum tip displacement of approximately 43% of the original gap before pull-in occurs. This limits the capacitance ratio to approximately 1.24:1.

3.4.2 Fixed-Fixed Beams

A single fixed-fixed beam, two-plate capacitor (Figure 3.1(b)) with dimensions the same as the verification case is also presented. The maximum displacement (beam centre) is shown in Figure 3.14. The capacitance change is shown in Figure 3.15.

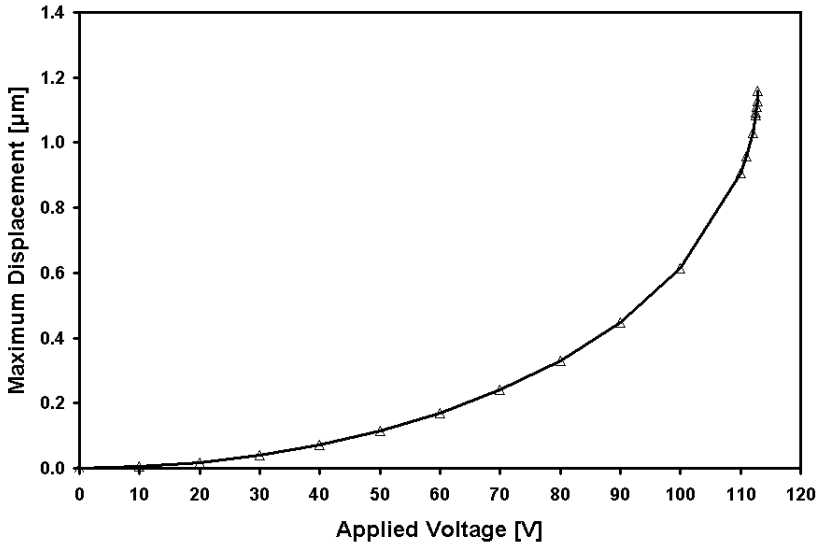

Figure 3.14: Beam deflection of fixed-fixed beam two-plate capacitor.

The capacitor has a maximum deflection of 1.16 μm and a pull-in voltage between 112.9 V and 113.0 V. With the same dimensions, the cantilever beam capacitor had a maximum deflection of 1.31 μm. The pull-in voltage from Equation 3.9 is 113.52 V, which agrees quite well. The initial capacitance is 1.05 pF and the final capacitance

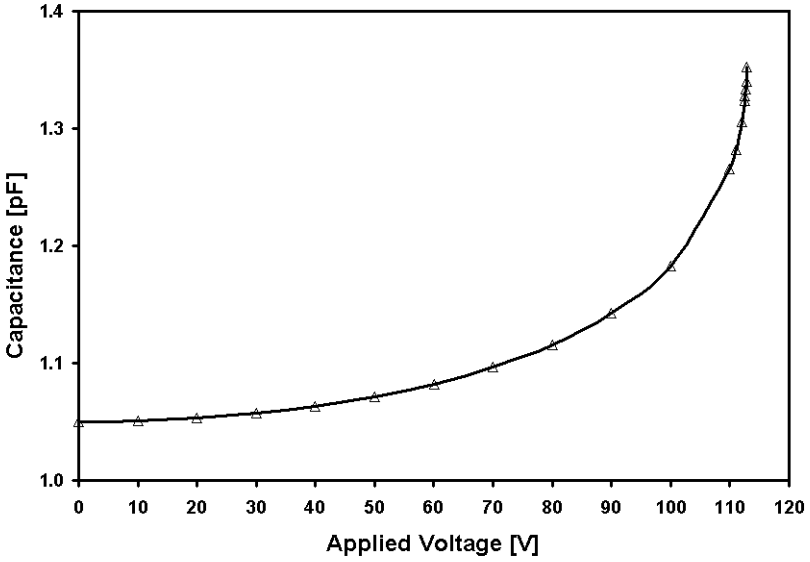

Figure 3.15: Capacitance of fixed-fixed beam two-plate capacitor.

is 1.35 pF. This corresponds to a capacitance ratio of 1.28:1.

The results from the fixed-fixed beam capacitor suggest that the capacitor has a smaller maximum displacement but a larger capacitance ratio, than the cantilever beam case. The centre of the beam will have a maximum displacement of approximately 39% of the original gap before pull-in occurs. This corresponds to a capacitance ratio of 1.28:1.

3.5 Three-Plate Capacitor Investigation

It has been shown that a three-plate configuration can be used to increase the tuning ratio [5]. In this configuration the middle plate is free to move and the surrounding plates are fixed. A cantilever beam three-plate configuration is shown in Figure 3.16(a) and a fixed-fixed beam configuration is shown in Figure 3.16(b).

A voltage applied between the movable middle plate and the top plate causes the middle plate to deflect towards the top plate. This reduces the capacitance between the middle plate and the bottom plate. The beam is being pulled away from the other electrode in the capacitance gap. If the actuator gap is larger than

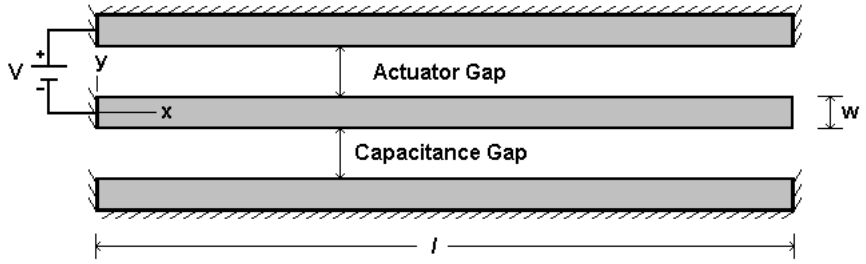

(a) Cantilever beam

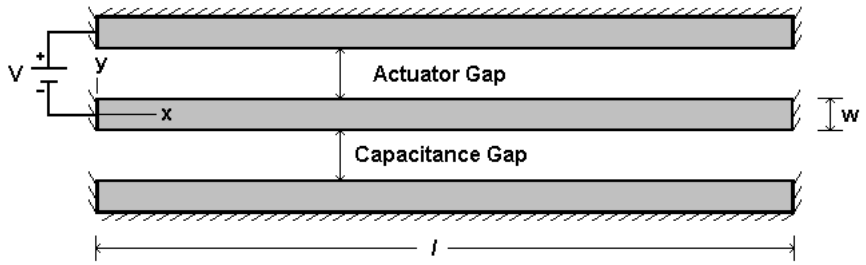

(b) Fixed-fixed beam

Figure 3.16: Three-plate capacitor configurations.

the capacitance gap, an increase in tuning ratio over the two-plate capacitor can be achieved. For an increase in tuning ratio, for the cantilever beam case, the actuator gap must be larger than 1.24 times the capacitance gap. For the fixed-fixed beam case, the actuator gap must be larger than 1.28 times the capacitance gap. For a given actuator gap, as the capacitance gap decreases, the tuning ratio increases.

Another advantage of the three-plate capacitor is that the RF and control signals can be separated. In the two-plate capacitor case, these signals are on the same line and require RF chokes to combine the two signals.

Theoretically, the beam in the three-plate capacitor could be made to deflect towards both electrodes, and is the approach taken by Dec et al. [5]. This leads to a further increase in tuning ratio, but this technique requires coupling of RF and control signals as well as a method to switch the control signal between the two electrodes.

3.5.1 Cantilever Beams

Simulations of two three-plate cantilever beam variable capacitors are presented next. The dimensions of the two capacitors are shown in Table 3.3. The two capacitors differ only by the actuator gap.

Table 3.3: Three-plate cantilever beam capacitor dimensions.

Dimension Set	1	2
Beam Length (l) [μm]	350	350
Beam Width (w) [μm]	3	3
Actuator Gap [μm]	3	6
Capacitance Gap [μm]	1	1

The maximum displacement (tip deflection) of the capacitors is shown in Figure 3.17 and the capacitance change is shown in Figure 3.18. The maximum

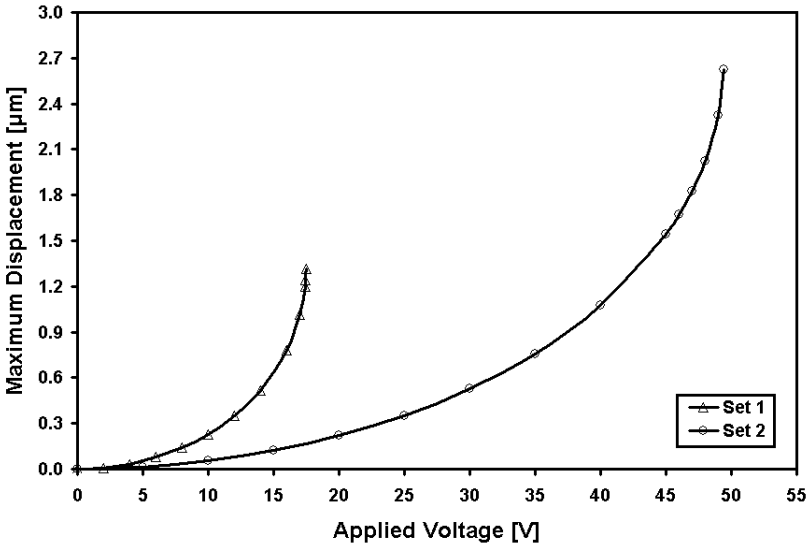

Figure 3.17: Beam deflection of cantilever beam three-plate capacitors.

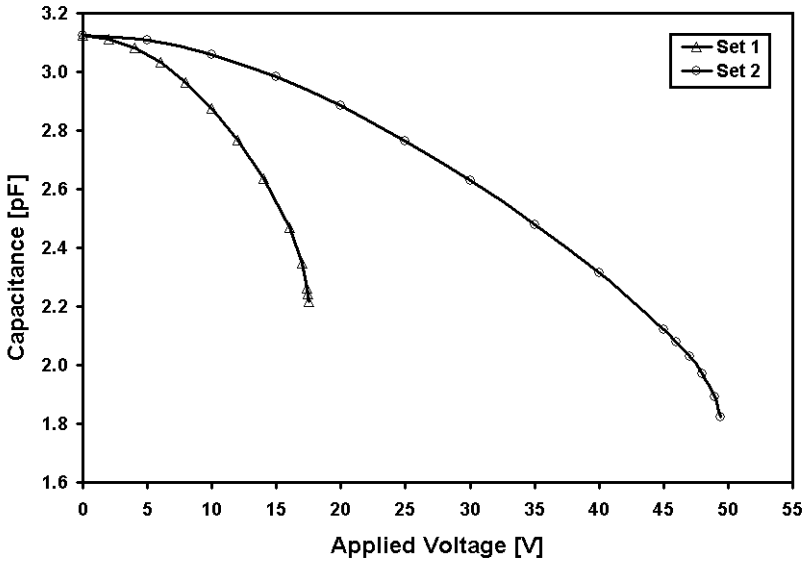

Figure 3.18: Capacitance of cantilever beam three-plate capacitors.

deflection for Set 1 is 1.31 μm which is expected for a 3 μm actuator air gap. For Set 2 the maximum deflection is 2.62 μm due to an actuator gap that is double the Set 1 actuator gap. The pull-in voltage for Set 1 is between 17.5 V and 17.6 V as expected. For Set 2 the pull-in voltage is between 49.4 V and 49.5 V. Equation 3.8 predicts a pull-in voltage of 49.32 V. The maximum capacitance (3.12 pF) is the same for both dimension sets and is consistent with a 1 μm capacitance gap. The minimum capacitance of Set 1 is 2.22 pF, which corresponds to a capacitance ratio of 1.41:1. The minimum capacitance of Set 2 is 1.82 pF, which corresponds to a capacitance ratio of 1.71:1. With both set dimensions the tuning ratio has been increased over the two-plate capacitor tuning ratio. With three-plate variable capacitors the trade-off is an increase in tuning ratio for an increase in actuation voltage.

3.5.2 Fixed-Fixed Beams

Simulation results for a fixed-fixed beam three-plate capacitor (Figure 3.16(b)) with geometry the same as the Set 1 dimensions is shown. The maximum deflection of the beam, which occurs at the beam centre, is identical to the two-plate fixed-fixed beam

capacitor shown in Figure 3.14. The capacitance variation is shown in Figure 3.19.

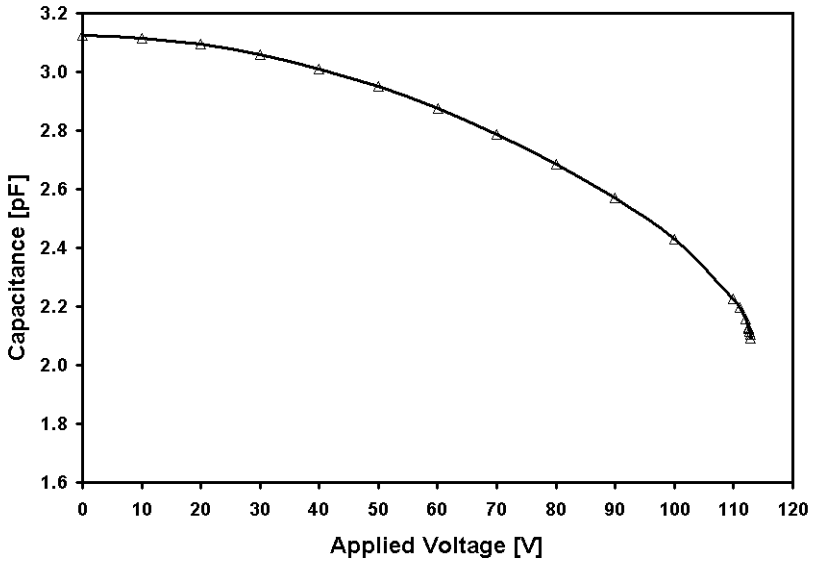

Figure 3.19: Capacitance of fixed-fixed beam three-plate capacitor.

As in the two-plate fixed-fixed beam case the beam has a maximum displacement of 1.16 μm and a pull-in voltage between 112.9 V and 113.0 V. The initial (maximum) capacitance 3.12 pF and the final (minimum) capacitance is 2.09 pF. This corresponds to a tuning ratio of 1.49:1. As in the two-plate capacitor case, the fixed-fixed beam capacitance ratio is slightly larger than the cantilever beam capacitance ratio.

3.6 Capacitors With Contact Surfaces

3.6.1 Two-Plate Cantilever Beams

A two-plate cantilever beam variable capacitor with a contact surface is shown in Figure 3.20. The contact surface prevents the movable beam from making contact with the fixed bottom plate if voltages larger than the pull-in voltage are applied. The movable beam cannot pass through the contact surface. The maximum beam

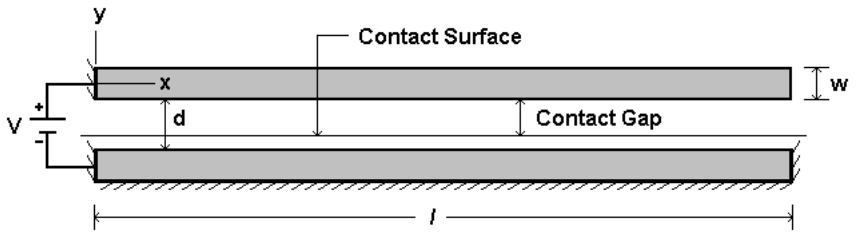

Figure 3.20: Two-plate cantilever beam capacitor with a contact surface.

displacement cannot be larger than the contact gap. In an actual device, this surface has been realized in capacitors using stoppers [36], and in switches using a dielectric material [43]. The addition of a contact surface allows the capacitor to function with voltages greater than the pull-in voltage, which can lead to an increase in tuning range.

Two configurations are simulated with geometries listed in Table 3.4. The capacitors have the same geometries as the case without the contact surface. Two different contact surfaces are selected based on the two different behaviors that are possible. The first scenario occurs when the contact gap is less than or equal to the maximum displacement which occurs just before pull-in. For a cantilever beam with a 3 μm air gap this was determined to be 1.31 μm. The second scenario occurs when

Table 3.4: Dimensions for two-plate cantilever beam capacitors with a contact surface.

Dimension Set	1	2
Beam Length (l) [μm]	350	350
Beam Width (w) [μm]	3	3
Air Gap (d) [μm]	3	3
Contact Gap [μm]	1.31	2.50

the contact gap is greater than the maximum displacement before pull-in. In this case pull-in occurs as the beam collapses onto the contact surface after the pull-in voltage has been reached. A contact gap of 2.5 μm was selected for this scenario.

For the Set 1 dimensions the maximum displacement (beam tip) is shown in Figure 3.21 and the capacitance change is shown in Figure 3.22. The y-axis scales

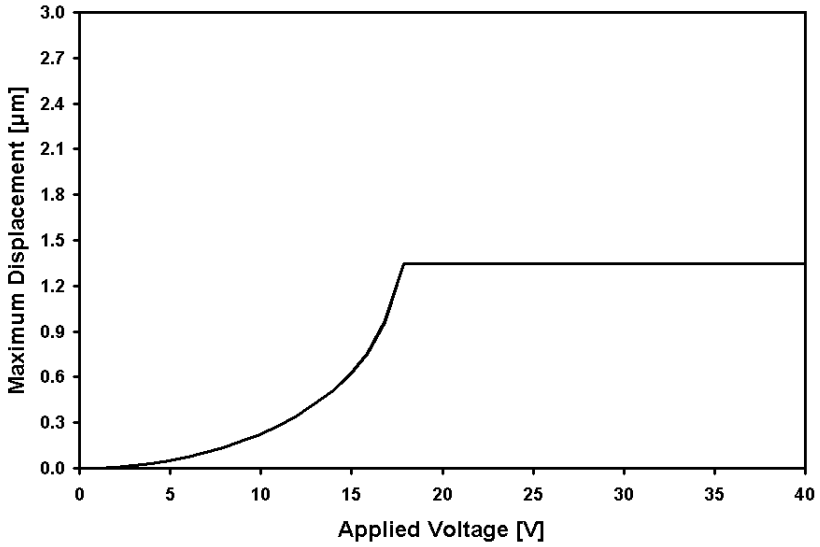

Figure 3.21: Deflection of two-plate cantilever beam capacitor with a contact surface [Set 1].

are chosen so that all contact plots could have the same scale for comparison. The applied voltage was increased from 0 V to 40 V and then decreased back to 0 V. The tip deflection increases to 1.31 μm at 17.5 V. At this position the beam tip is touching the contact surface. As the voltage is increased past the pull-in voltage, the beam is pulled closer to the contact surface but the maximum displacement never exceeds 1.31 μm as expected. The displacement of the beam is identical regardless of whether the applied voltage was increasing or decreasing.

The capacitance of the device increases from 1.05 pF at 0 V to 1.30 pF at 17.5 V as observed previously. After contact the capacitance increases as the beam is pulled

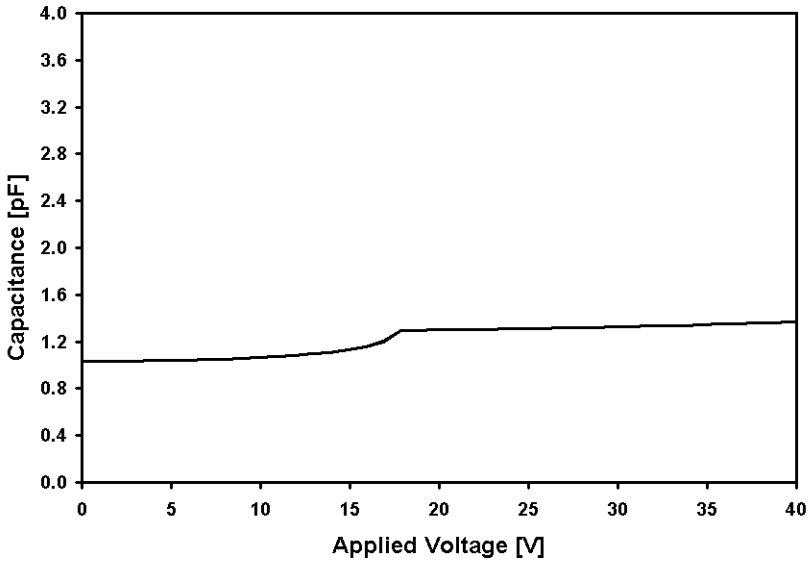

Figure 3.22: Capacitance of two-plate cantilever beam capacitor with a contact surface [Set 1].

towards the contact surface. The capacitance at 40 V is 1.37 pF. This results in a tuning range of 1.30:1.

For the Set 2 dimensions the maximum displacement (beam tip) is shown in Figure 3.23 and the capacitance change is shown in Figure 3.24. The applied voltage was increased from 0 V to 40 V and then decreased back to 0 V as in the previous simulation. As the voltage is increased from 0 V to 17.5 V the beam bends stably as shown in Figure 3.25(a) [36]. The tip deflection is 1.31 μm at 17.5 V. When the voltage is increased past the pull-in voltage, the beam suddenly collapses onto the contact surface and is supported by the beam tip (Figure 3.25(b)). This causes a sudden increase in capacitance at 17.5 V. Between 17.5 V and 32.0 V, only the beam tip is in contact with the contact surface [36]. The capacitance is increasing because the beam is being pulled towards the contact surface. At 32.0 V the beam flattens against the contact surface and is no longer only supported by the tip. Increasing the voltage beyond 32.0 V causes the beam to "zip" along the contact surface as shown in Figure 3.25(c) [36]. As the beam flattens against the contact surface, the

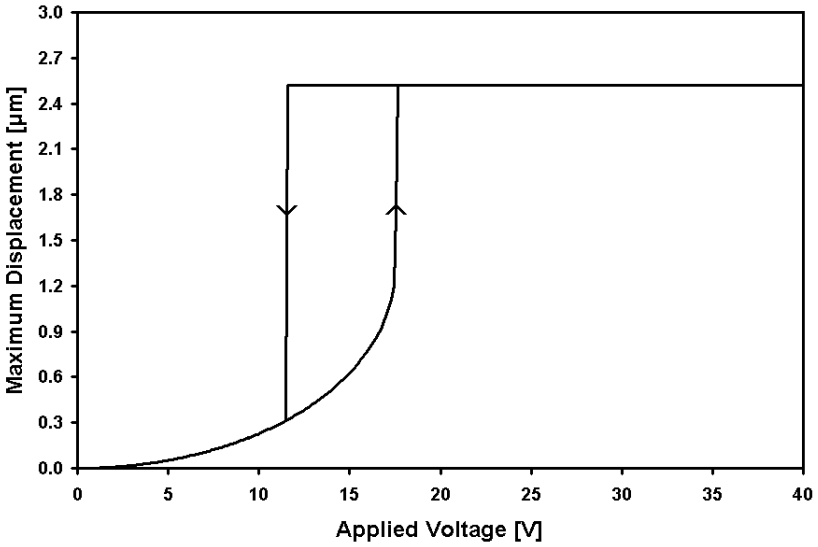

Figure 3.23: Deflection of two-plate cantilever beam capacitor with a contact surface [Set 2].

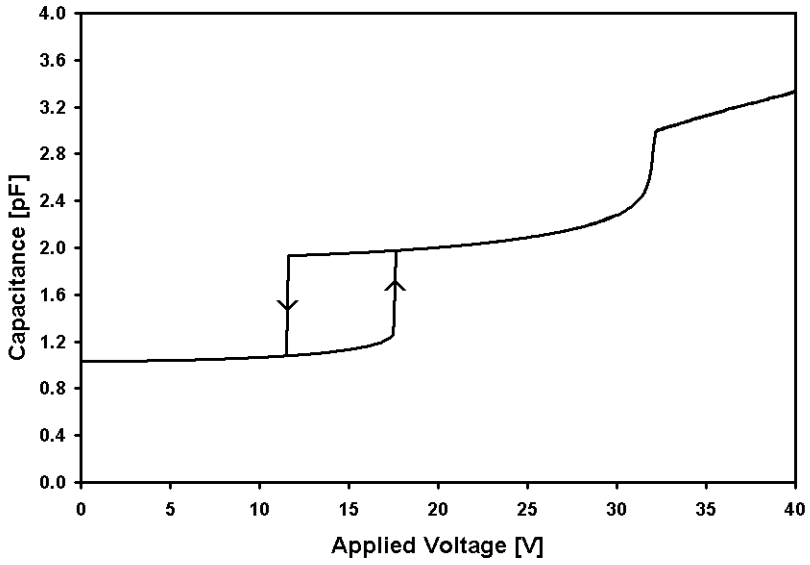

Figure 3.24: Capacitance of two-plate cantilever beam capacitor with a contact surface [Set 2].

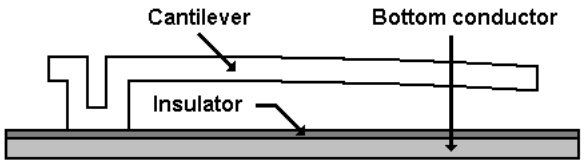

(a) Beam bends stably before pull-in

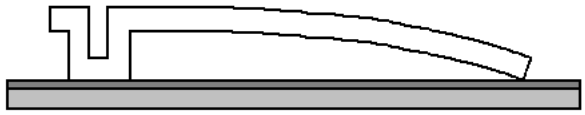

(b) Beam collapses to contact surface supported by beam tip

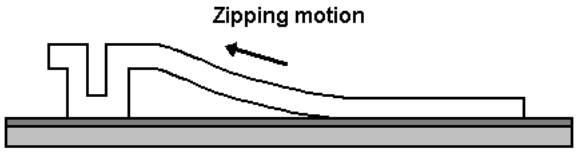

(c) Tip flattens and beam "zips" along in contact with the substrate

Figure 3.25: Beam deflection with increasing voltage [36].

capacitance continues to increase.

When the voltage is decreased, the voltage must be made smaller than the pull-in voltage in order for the beam to be released from the contact surface. The beam does not release from the contact surface until the voltage is lowered below 11.6 V. This result is known as hysteresis and is explained as follows. When the beam is in contact with the contact surface, the gap between the beam and the fixed bottom electrode is smaller than it was just prior to pull-in. The voltage must therefore be reduced to a voltage lower than the pull-in voltage for the beam to be released from the contact surface [44].

The capacitance at 40 V is 3.31 pF, which corresponds to a tuning ratio of 3.15:1. The capacitance ratio has been increased drastically, but the capacitance change is now discontinuous due to the pull-in phenomena. This results in hysteresis, which

is a problem since the capacitance can be different values for a given voltage. It should be noted that the capacitor with Set 1 dimensions is only supported by the tip between 17.5 V and 40 V. The beam does not flatten against the contact surface until approximately 51 V. The voltage required is greater because it is farther from the fixed bottom plate due to the location of the contact surface.

In addition to increasing the capacitance ratio, stoppers have been successfully employed to control the beam bending characteristics and customize the capacitance versus voltage curve. This method has been used to obtain linear capacitance versus voltage and linear frequency versus voltage for a VCO application [36].

3.6.2 Two-Plate Fixed-Fixed Beams

The simulations from the previous section were repeated with a fixed-fixed beam as shown in Figure 3.26. The beam dimensions are listed in Table 3.5. The contact

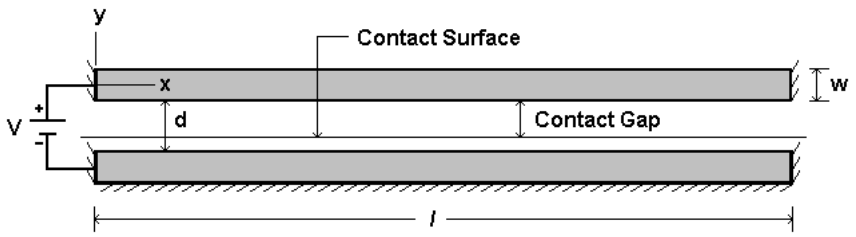

Figure 3.26: Two-plate fixed-fixed beam capacitor with a contact surface.

gap for Set 1 was set to 1.16 μm. This is the maximum deflection before pull-in for a fixed-fixed beam with a 3 μm gap.

For Set 1, the maximum displacement of the beam is shown in Figure 3.27 and the capacitance change is shown in Figure 3.28. The voltage was increased from 0 V to 260 V and then decreased back to 0 V. The centre of the beam has a displacement of 1.16 μm at a voltage of 112.9 V. At this voltage the centre of the beam comes in contact with the contact surface. As the voltage is increased the contact surface limits the maximum displacement to 1.16 μm.

Table 3.5: Dimensions for two-plate fixed-fixed beam capacitors with a contact surface.

Dimension Set	1	2
Beam Length (l) [μm]	350	350
Beam Width (w) [μm]	3	3
Air Gap (d) [μm]	3	3
Contact Gap [μm]	1.16	2.50

The increasing voltage pulls the beam against the contact surface, which causes an increase in capacitance. The capacitance of the device increases from 1.05 pF at 0 V to 1.35 pF at 112.9 V. The capacitance at 260 V is 1.50 pF. This results in a tuning range of 1.43:1. This ratio is substantially larger than the cantilever beam case. This is due to the fact that the fixed-fixed beam capacitor is not supported by the tip, as in the cantilever beam case. More of the beam comes into contact with

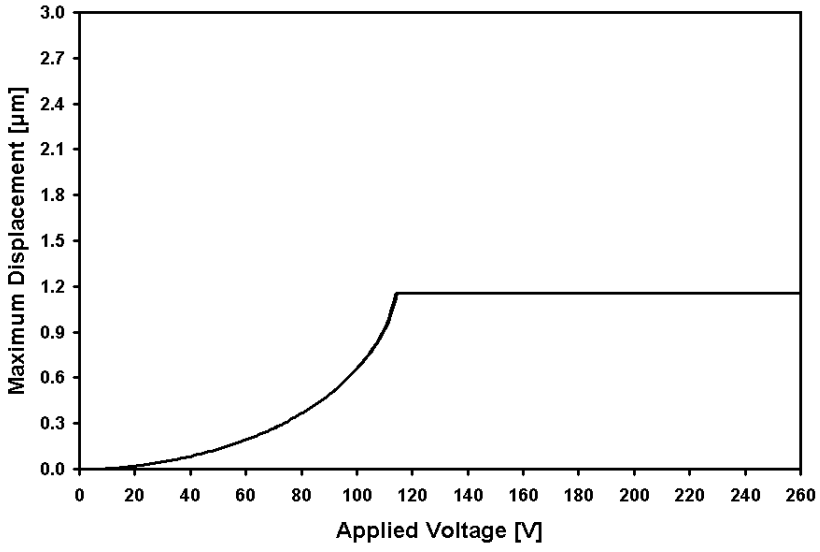

Figure 3.27: Deflection of two-plate fixed-fixed beam capacitor with a contact surface [Set 1].

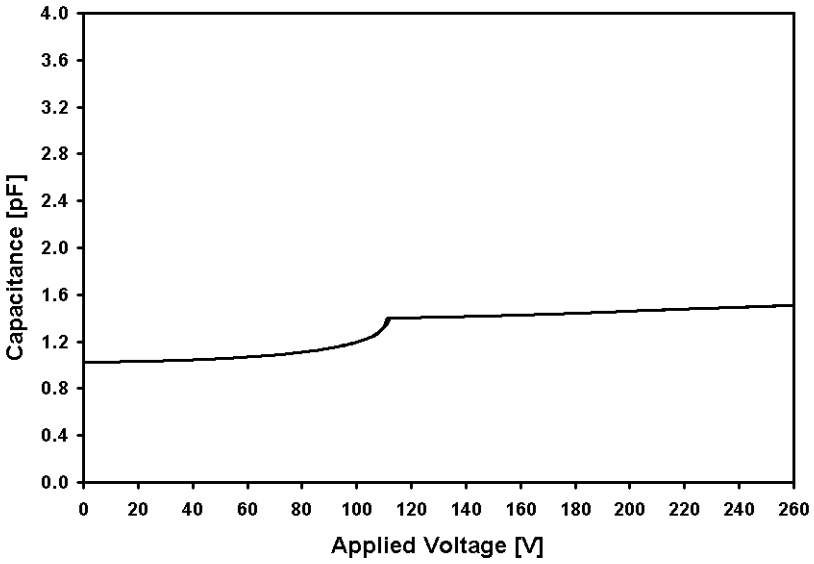

Figure 3.28: Capacitance of two-plate fixed-fixed beam capacitor with a contact surface [Set 1].

the contact surface, which results in a larger capacitance ratio.

For the Set 2 dimensions the maximum displacement (beam centre) is shown in Figure 3.29 and the capacitance change is shown in Figure 3.30. The applied voltage was increased from 0 V to 260 V and then decreased back to 0 V as in the Set 1 simulation. The beam deflects stably towards the contact surface until pull-in occurs at 112.9 V. The beam then collapses onto the contact surface. As the voltage is increased the beam continues to bend and "zips" along the contact surface. Since the beam is fixed on both ends and is never supported by the tip, there are not three regions of operation as in the cantilever beam case.

The maximum capacitance is 3.87 pF, which results in a capacitance ratio of 3.69:1. Hysteresis occurs in the fixed-fixed beam case also. The beam is released from the contact surface at a voltage of 77.0 V. It is worthy to note that the capacitance after pull-in is much larger for the fixed-fixed beam case than the cantilever beam case since the tip does not support the beam.

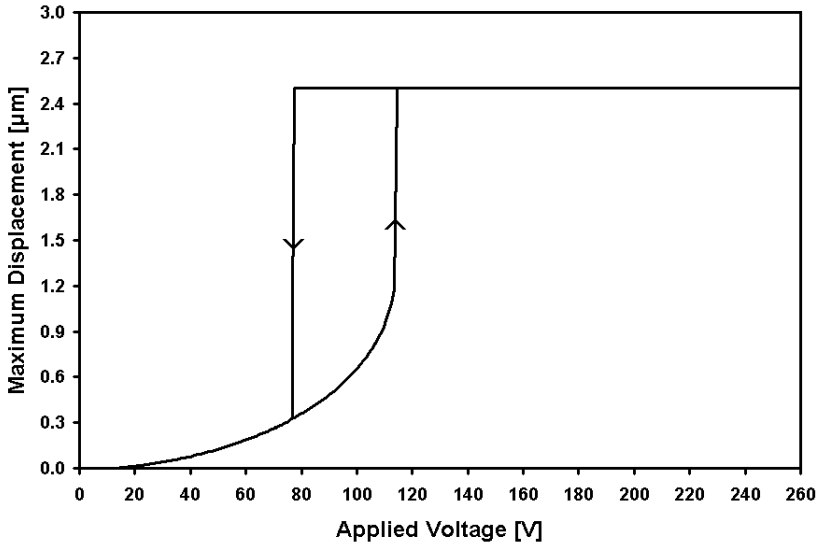

Figure 3.29: Deflection of two-plate fixed-fixed beam capacitor with a contact surface [Set 2].

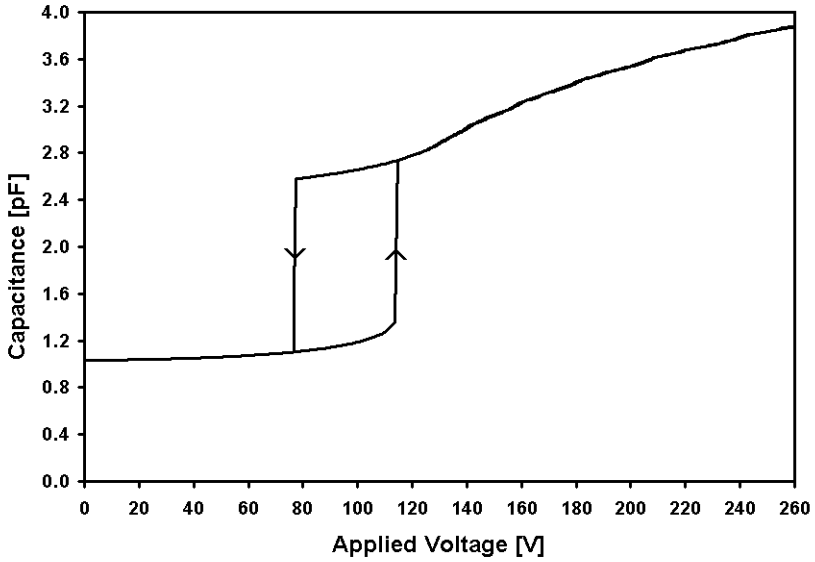

Figure 3.30: Capacitance of two-plate fixed-fixed beam capacitor with a contact surface [Set 2].

3.6.3 Three-Plate Cantilever Beams

A three-plate cantilever beam variable capacitor with a contact surface is shown in Figure 3.31. The geometries for the two dimension sets are listed in Table 3.6. For Set 1, the capacitance plot is shown in Figure 3.32. The deflection plot is

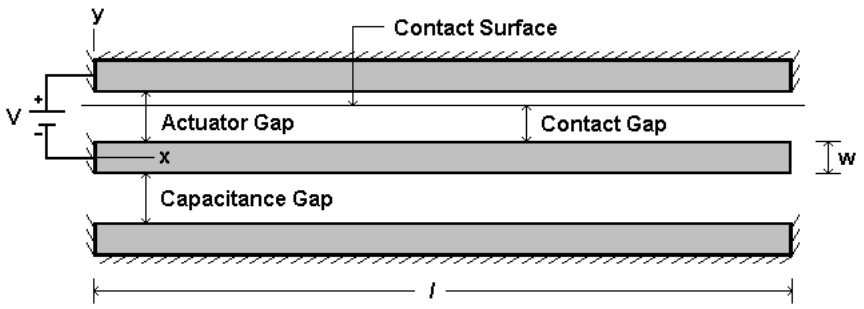

Figure 3.31: Three-plate cantilever beam capacitor with a contact surface.

Table 3.6: Dimensions for three-plate cantilever beam capacitors with a contact surface.

Dimension Set	1	2
Beam Length (l) [μm]	350	350
Beam Width (w) [μm]	3	3
Actuator Gap [μm]	3	3
Capacitance Gap [μm]	1	1
Contact Gap [μm]	1.31	2.50

identical to the two-plate capacitor case, since the gap has not been changed, and is shown in Figure 3.21. The initial capacitance is 3.12 pF and is consistent with a 1 μm capacitance gap. At 17.5 V the tip contacts the contact surface. Deflection is

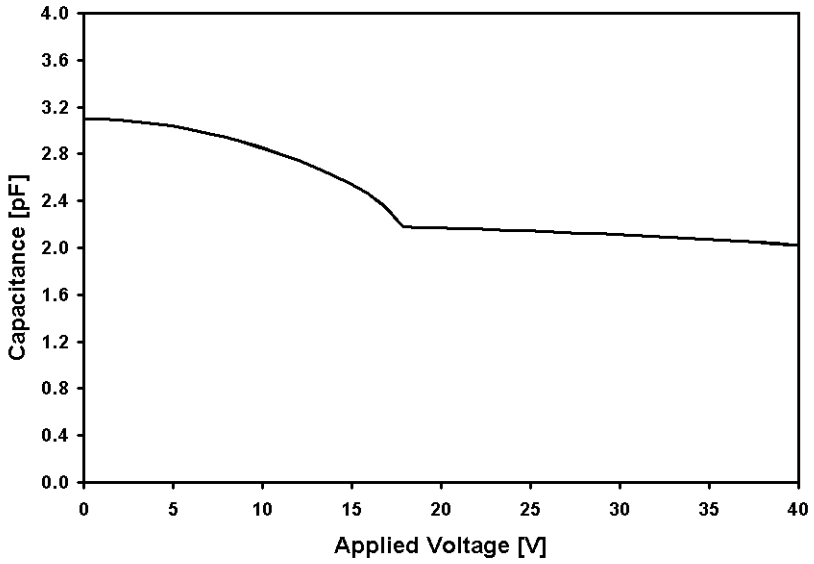

Figure 3.32: Capacitance of three-plate cantilever beam capacitor with a contact surface [Set 1].

1.31 μm and the capacitance is 2.22 pF. The capacitance continues to decrease as the beam is pulled toward the fixed top plate. The beam does not flatten against the contact surface until approximately 51 V, which is not shown in the plot. At 40 V the capacitance is 2.03 pF, which results in a capacitance ratio of 1.54:1. This is substantially larger than the 1.30:1 tuning ratio observed in the two-plate case.

For Set 2, the capacitance plot is shown in Figure 3.33. The deflection plot is identical to Figure 3.23. The underlying capacitor behavior is identical to the two-plate case (Figure 3.25). As in the two-plate case, three regions of operation are observed. The capacitance at 40 V is 1.46 pF. This corresponds to a tuning ratio of 2.14:1. This ratio is much smaller than the ratio observed for the two-plate case (3.15:1). These results suggest that if the contact surface is placed far from the movable beam (unstable operation), and the device is to be operated in the zipping region (after pull-in), then a larger capacitance ratio can be obtained from two-plate capacitors. Three-plate capacitors offer an advantage when the device operates stably and no hysteresis occurs.

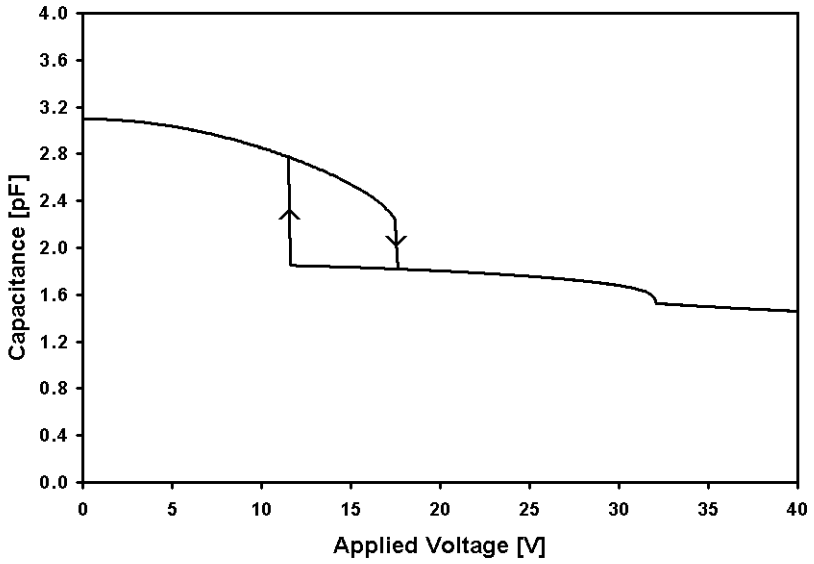

Figure 3.33: Capacitance of three-plate cantilever beam capacitor with a contact surface [Set 2].

3.6.4 Three-Plate Fixed-Fixed Beams

A three-plate fixed-fixed beam variable capacitor with a contact surface is shown in Figure 3.34. The relevant dimensions for the simulations are listed in Table 3.7. For Set 1 the change in capacitance is shown in Figure 3.35. For Set 2 the change in capacitance is shown in Figure 3.36.

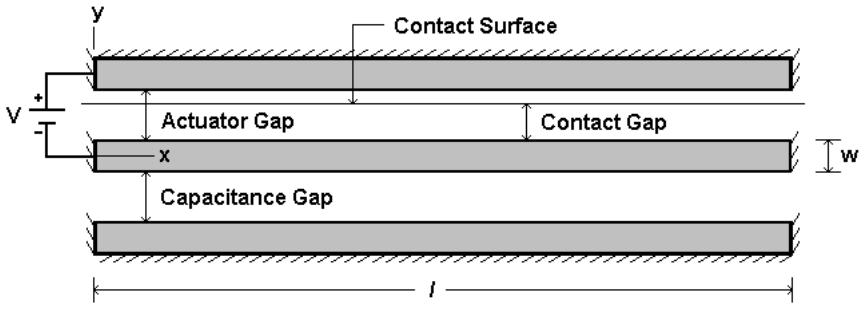

Figure 3.34: Three-plate fixed-fixed beam capacitor with a contact surface.

Table 3.7: Dimensions for three-plate fixed-fixed beam capacitors with a contact surface.

Dimension Set	1	2
Beam Length (l) [μm]	350	350
Beam Width (w) [μm]	3	3
Actuator Gap [μm]	3	3
Capacitance Gap [μm]	1	1
Contact Gap [μm]	1.16	2.50

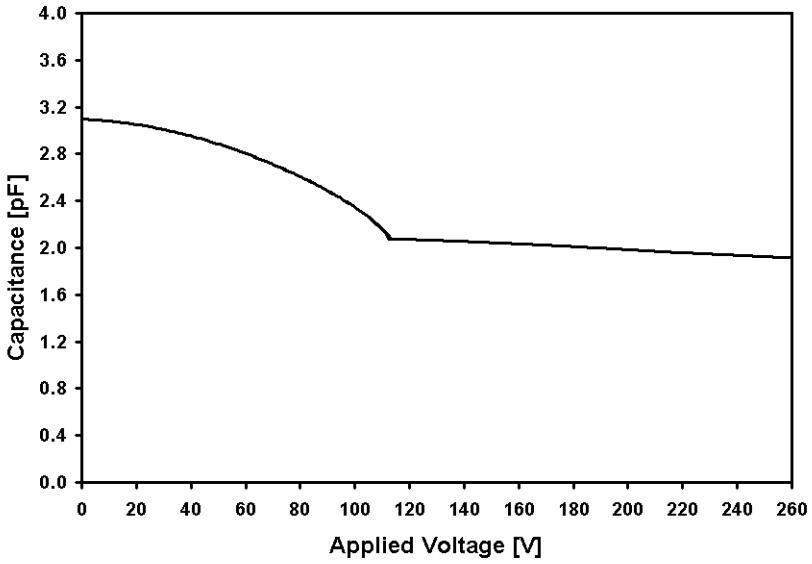

Figure 3.35: Capacitance of three-plate fixed-fixed beam capacitor with a contact surface [Set 1].

For Set 1, the displacement is identical to the two-plate case shown in Figure 3.27. The capacitance changes from 3.12 pF with no actuation voltage, to 2.09 pF at approximately 112.9 V. This corresponds to a deflection of 1.16 um, at which the

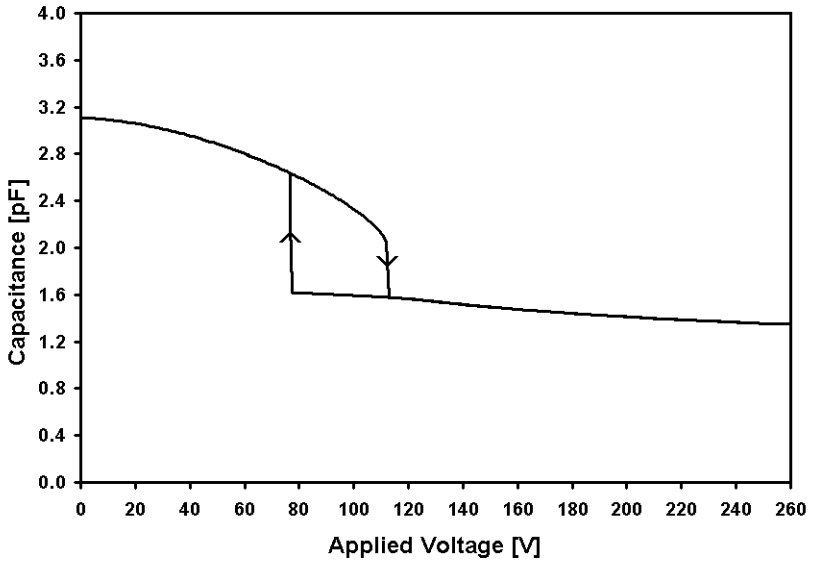

Figure 3.36: Capacitance of three-plate fixed-fixed beam capacitor with a contact surface [Set 2].

beam centre comes into contact with the contact surface. As the voltage is increased, more of the beam comes into contact with the contact surface, decreasing capacitance. The capacitance at 260.0 V is 1.90 pF, for a tuning ratio of 1.64:1.

With the contact surface 2.5 μm from the beam (Set 2), the deflection is identical to Figure 3.29. Only two regions of operation are observed since the beam does not rest on the tip as in the cantilever beam case. At 260 V the capacitance is 1.35 pF. This corresponds to a tuning ratio of 2.31:1. As in the cantilever beam case, the capacitance ratio is larger for two-plate capacitors when the contact surface is placed far from the beam.

3.7 Summary

In the previous sections both cantilever and fixed-fixed beams were investigated. The advantages of cantilever beams include low actuation voltage and the absence of residual stress. Fixed-fixed beams require increased force to actuate, but this attribute makes them attractive when the operating environment is likely to feature

large accelerations. The particular application for the beam will decide which type is more appropriate.

The advantage of two-plate capacitors is that for a minimum gap size, they can be operated with low actuation voltage relative to the other configurations that were investigated. The drawback is their limited tuning range. Three-plate capacitors can be used to increase the tuning range, but this comes at the expense of an increase in actuation voltage, given a minimum gap size. Another advantage of three-plate capacitors is the separation of RF and control signals.

Contact surfaces can also be used to increase the tuning range but this will result in an increase in actuation voltage as well. Contact surfaces can also result in additional characteristics depending on the location of the surface. If the surface is placed past the pull-in point, then hysteresis will occur which will cause the change in capacitance to be discontinuous. This is likely not an advantage when designing an analog MEMS variable capacitor, but it has been taken advantage of in the development of MEMS digital capacitors [10].

This investigation is in no means an exhaustive treatment of electrostatically actuated beams. Many other beam configurations can be used to achieve an increase in performance. For example, the fixed electrodes can be different lengths than the beam, or the gaps can be a function of the beam length [45]. Both of these methods can be utilized to increase the capacitance ratio. One of the methods will be utilized in the next chapter. As in the examples above the performance gain obtained in one category results in a loss in another category. In this case a gain in capacitance tuning ratio is usually accompanied by an increase in tuning voltage.

4. LIGA-MEMS VARIABLE CAPACITORS

4.1 LIGA-MEMS Fabrication

4.1.1 Seed Layer as a Sacrificial Layer

The fabrication steps applicable to this procedure are shown in Figure 4.1. The fabrication process begins with the structure shown in Figure 4.1(a). The bottom layer is the substrate onto which a thin metal film is applied. The thin metal film, typically 3 - 5 μm thick Ti/TiOx (titanium, oxidized titanium), will act as a seed layer during electroplating. A wide variety of substrate materials can be used. Examples of these include silicon, alumina, and quartz. A layer of polymethyl methacrylate (PMMA) several hundreds of micrometers thick is then glued and directly polymerized to the plating base [46]. PMMA is an X-ray sensitive resist that will be patterned to define the MEMS structures.

The next step is to expose the PMMA to X-ray radiation as shown in Figure 4.1(b). An absorber pattern from an X-ray transparent mask is transferred into the PMMA using highly collimated synchrotron hard X-ray radiation with a characteristic wavelength between 0.2 and 0.6 nm. The mask is typically constructed of an absorber pattern on top of a carrier foil. The absorber must have a high atomic weight and therefore a high absorption coefficient. The most common metal used is gold, but tantalum and tungsten are also used. To achieve appropriate absorption the gold layer must be at least 10 μm thick [46]. The carrier foil must have a low absorption coefficient and low thickness so it is as X-ray transparent as possible. Therefore materials with a low atomic weight are often chosen. The most common materials used are beryllium, titanium, and silicon. The thickness of the carrier foil must be chosen carefully in order to maintain high transmission levels. Beryllium

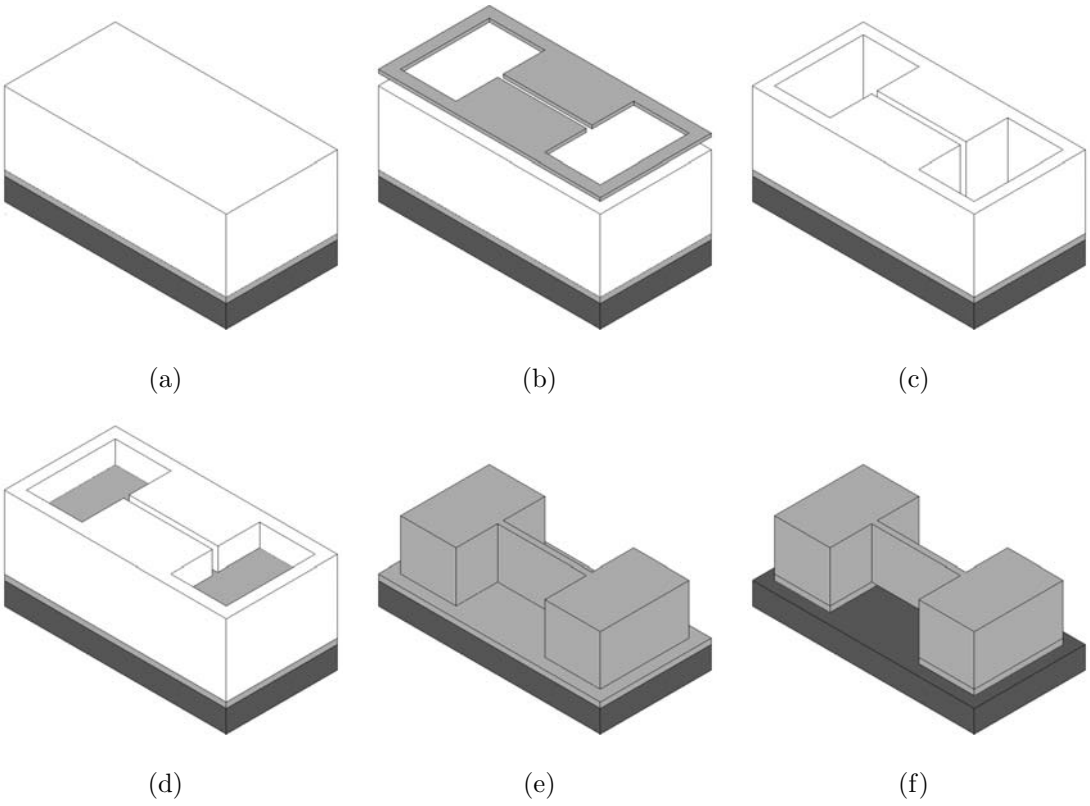

Figure 4.1: LIGA fabrication steps using the seed layer as a sacrificial layer.

layers of several 100 μm can be used but titanium is limited to a thickness of several micrometers.

The exposed regions of the resist are then dissolved using a suitable developer as shown in Figure 4.1(c). The dissolved PMMA regions are then filled with metal by micro-electroplating as shown in Figure 4.1(d). The metal deposition starts on the electrically conductive seed layer. The most commonly electroplated metal to date has been nickel due to low internal stresses in the tall metal structures, but copper and gold are finding increased usage. After electroplating, the structure is exposed to X-ray flood irradiation, which allows the remaining PMMA to be removed with developer. The resulting structure is shown in Figure 4.1(e). The titanium seed layer is then selectively etched to release the thin beam and isolate any adjacent metal structures as shown in Figure 4.1(f). Hydrofluoric (HF) acid is commonly used because it does not attack the nickel structures [46].

4.1.2 Patterned Seed Layer

The steps followed in this technique are very similar to the previous technique and are shown in Figure 4.2. The process starts in Figure 4.2(a) with a seed layer that

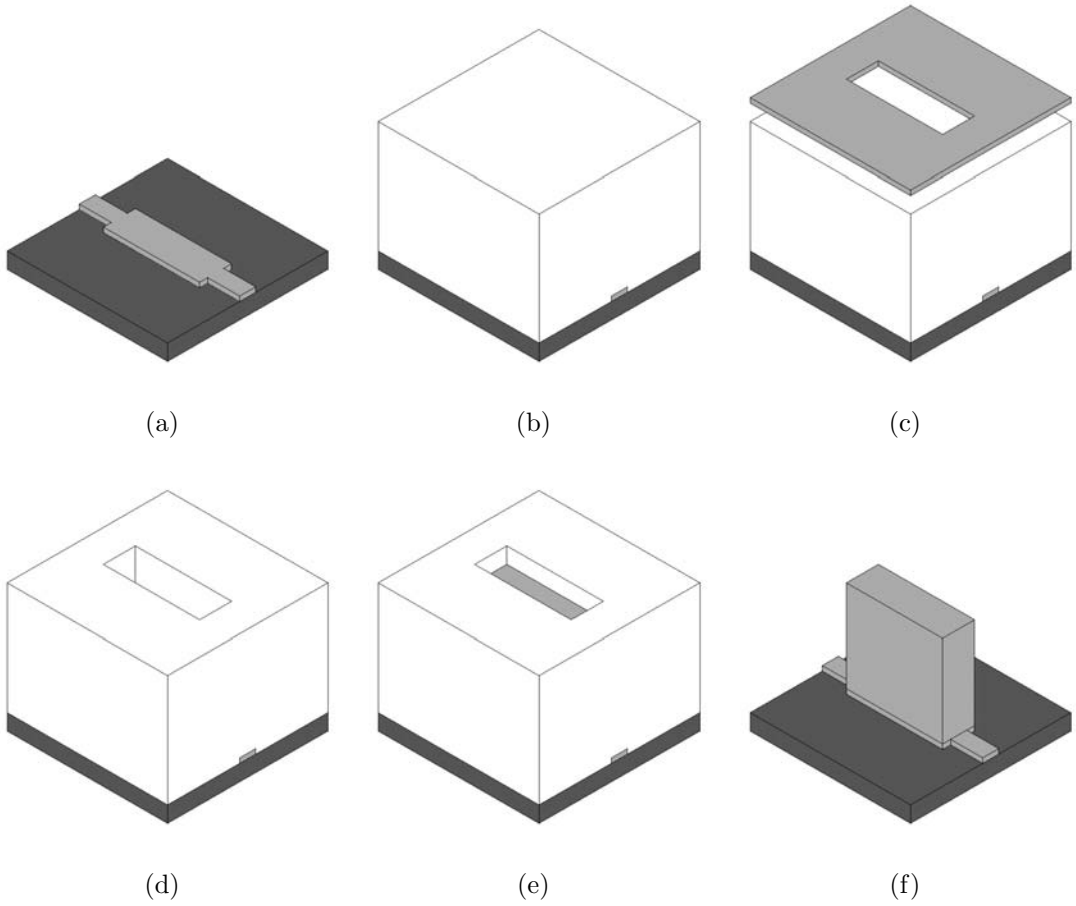

Figure 4.2: LIGA fabrication steps using a patterned seed layer.

has been patterned using a suitable lithography technique. The seed layer must be patterned because the cantilever requires electrical connections using the seed layer. In the previous fabrication technique the cantilever is connected to the large metal structures, which also provide electrical connection. The PMMA layer is then applied to the patterned seed layer as shown in Figure 4.2(b). The PMMA is then exposed using a mask in the same manner as in the previous technique. This is

shown in Figure 4.2(c). Developing the resist and electroplating follow as shown in Figure 4.2(d) and Figure 4.2(e). The remaining resist is then flood irradiated and developed to expose the final structure as shown in Figure 4.2(f). The seed layer does not need to be etched using HF acid since the seed layer was pre-patterned. The resulting structure is a freestanding cantilever with a patterned seed layer that can be used to make the appropriate electrical connections.

4.2 Capacitor Design Considerations

The remaining sections of this chapter present a class of LIGA-MEMS variable capacitors that were designed and simulated. A portion of the devices presented in this chapter were also fabricated. These devices were designed to be suitable for fabrication using the seed layer as a sacrificial layer. No devices were designed that could be produced using the patterned seed layer technique. The sacrificial layer technique was chosen for a number of reasons. The first reason is that it requires a single lithography step unlike the patterned seed layer technique, which requires two lithography steps and possibly two masks in different technologies. The second reason is that the patterned seed layer technique requires very precise alignment of the patterned seed layer with the X-ray mask. The precise alignment is necessary since the beam widths and gap sizes are small. Alignment accuracy would depend on the structures, but could be sub-micron which further complicates the process. The third reason is that there are possible problems with the adhesion of the seed layer to the substrate during actuation of the beam. During actuation, if the adhesion of the seed layer and substrate is not strong enough, the seed layer could pull away from the substrate, which would cause a failure of the device. This is not likely a problem with the sacrificial layer technique, since the beam and the connecting region is a continuous metal layer and the connecting area has comparatively large seed layer interface to the substrate. The patterned seed layer technique also does not allow rounding of the corners of the beam, which was shown to be important to stress failure in Chapter 2.

Other considerations were taken into account during the design of the capacitors.

One of the most important considerations was testability. This includes a method to make electrical connections to the capacitors. It was decided that a suitable solution would be to use CPW probes (Cascade Microtech^{TM}ACP40-W-GSG-150) connected to a network analyzer (Agilent Technologies^{TM}8722ES). A pitch of 150 μm was decided for the probes, which is a commonly used standard probe. Another testability issue is actuation voltage. If the actuation voltage is too large, it becomes problematic to apply the actuation voltage to the capacitor. The maximum bias voltage that can be applied through the above network analyzer is 40 V. Therefore no fabricated capacitors have actuation voltages greater than 40 V. Some simulated capacitors have actuation voltages greater than 40 V.

As shown in previous sections, the actuation voltage can be made arbitrarily small by reducing the beam width, or the air gap, or by increasing the beam length. If these devices are to be fabricated however, there are limitations on these parameters. The maximum aspect ratio of structures that can reliably be produced currently by LIGA is approximately 100:1. This limits the size of the air gaps and the beam width to approximately 100 times smaller than the height of the metal layer. The beam length cannot be made arbitrarily long either. Smaller beam lengths leads to smaller overall dimensions, which leads to an increase in performance. This will be shown in the following sections.

4.3 Finite Element Analysis using Ansoft HFSS

4.3.1 Motivation

A method to obtain an estimate of the important electrical parameters of the capacitors is required. In order to perform this, the system must be capable of determining the impedance parameters of an arbitrary 3-D structure at microwave frequencies. This can be accomplished using the software package Ansoft HFSS^{TM}(High Frequency Structure Simulator) [40].

With this software package, the first step is to draw the structure, then specify material characteristics for each object, and identify ports and special surface

characteristics. HFSS then generates the necessary field solutions and associated port characteristics and S-parameters (scattering parameters). The problem can be solved at one specific frequency or at several frequencies within a range. The S-parameters obtained using HFSS can be converted to Z-parameters (impedance parameters) and can then be used to determine the important electrical parameters of the capacitor. Parameters of interest include the nominal capacitance, associated inductance or electrical self-resonance and equivalent series resistance or Q-factor. The nominal capacitance at low frequencies can also be used to determine the parasitic capacitance.

Like ANSYS described in the previous chapter, HFSS is a finite element solver, but with EM field boundary conditions. The software divides the geometric model into a large number of tetrahedra, where a single tetrahedron is a four-sided pyramid. This collection of tetrahedra is referred to as the finite element mesh. Structures with high aspect ratios, such as the devices presented here, require a dense mesh for high accuracy, which results in large computation times. This is complicated by the meshing of metals at high frequencies. Since the skin depth is very small at high frequencies, a large mesh results if the interior of the metals is to be accurately meshed. The element size required for accurate modeling would be a fraction of the skin depth and these elements would have to extend a few skin depths into the metal. This leads to prohibitive computation times. For this reason HFSS, by default, only solves inside objects with a bulk conductivity less than 10^5 S/m. Since most metals have a conductivity greater than this, they are solved using a surface approximation. For high Q-factor components, the real component of the impedance can be very small. For example, a 1 pF capacitor with a Q of 530 at 3 GHz has a impedance of approximately 0.1 - j 53.0 Ω. To obtain an accurate estimate of the Q-factor, the real component of the impedance must be determined very accurately. If the error in the real component is 0.01 Ω, the error in the Q-factor is approximately 50. With this in mind, and the fact that HFSS uses a surface approximation for metals, the real component of the impedance and therefore the Q-factor obtained using HFSS is an estimate.

4.3.2 Description

HFSS represents the model with a mesh of tetrahedra. At the vertex of each tetrahedron, HFSS stores the components of the field that are tangential to the three edges of the tetrahedron. By representing field quantities in this way, the system can transform Maxwell's Equations into matrix equations that are solved using traditional numerical methods.

HFSS is capable of multiple solution types. The type of interest for this application is a driven solution. This solution type is used for calculating the S-parameters of passive, high frequency structures such as microstrips, waveguides, and transmission lines, which are driven by a source. The source used to excite the model is called a wave port. Wave ports represent places in the geometry through which excitation signals enter and leave the structure. They are used when modeling strip lines and other waveguide structures.

HFSS starts the analysis by creating an initial mesh of the ports, the metal surfaces, and the non-metal objects. HFSS generates a solution by exciting each wave port individually. Port 1 is excited by a signal of one watt, and the other ports are set to zero watts. After a solution is generated, port 2 is set to one watt, and the other ports to zero watts and so forth. The ports must be perfectly matched to the characteristic impedance of the waveguide that each port faces in order not to allow reflection of power back into the model. This is realized by HFSS automatically by assuming that each port is virtually connected to a semi-infinitely long waveguide having the same cross-section and material properties as the part of the model exposed to the port. The two-dimensional field distributions generated for each port are used as the boundary conditions for the three-dimensional model [47].

The generalized S-matrix is then computed from the amount of reflection and transmission that occurs. This is the first step in an adaptive analysis process. HFSS automatically refines the mesh in regions where the error is high, which increases the solution's precision. A new set of generalized S-parameters is computed based on the refined mesh. This process is repeated until the change in the magnitude of

the S-parameters between iterations is smaller than a user specified value.

A generalized S-matrix describes what fraction of power associated with a given field excitation is transmitted or reflected at each port. The following discussion is valid for a network with an arbitrary number of ports n. Z_{0n} is the (real) characteristic impedance of the nth port, and V_n^+ and V_n^-, respectively, represent the incident and reflected voltage waves at port n. The wave amplitudes are defined as

$$a_n = \frac{V_n^+}{\sqrt{Z_{0n}}} \tag{4.1}$$

$$b_n = \frac{V_n^-}{\sqrt{Z_{0n}}} \tag{4.2}$$

where a_n represents a normalized incident wave at the nth port, and b_n represents a normalized reflected wave from that port [48]. The generalized scattering matrix is defined as

$$[b] = [S][a] \tag{4.3}$$

where the i, jth element is given by

$$S_{ij} = \left.\frac{b_i}{a_j}\right|_{a_k=0 \text{ for } k\neq j} \tag{4.4}$$

Therefore S_{ij} is the S-parameter describing how much of the excitation signal at port j is reflected back or transmitted to port i. For example, S_{21} is used to compute the amount of power from the port 1 excitation field that is transmitted to port 2. The phase of S_{21} specifies the phase shift that occurs as the signal travels from port 1 to port 2.

HFSS determines the characteristic impedance (Z_0) of each port from the values of power (P) and current (I) [49].

$$Z_{0n} = \frac{P}{I \cdot I} \tag{4.5}$$

The power and current are computed directly from the simulated fields. The power passing through a port is equal to [49]

$$P = \oint_s E \times H ds \tag{4.6}$$

where the surface integral is over the surface of the port. The current is computed by applying Ampere's law to a path around the port [49]

$$I = \oint_{l} H \bullet dl \tag{4.7}$$

While the net current computed in this way will be near zero, the current of interest is that flowing into the structure, I^{+}, or that flowing out of the structure, I^{-}. In integrating around the port, HFSS keeps a running total of the contributions to each and uses the average of the two in the computation of impedances [49].

The Z-parameters of the structure can be computed from the generalized S-parameters and the characteristic impedances of the ports. The Z-matrix is calculated from the S-matrix as follows [49]

$$Z = \sqrt{Z_0}(I - S)^{-1}(I + S)\sqrt{Z_0} \tag{4.8}$$

where S is the $n \times n$ generalized S-matrix, I is an $n \times n$ identity matrix, and Z_0 is a diagonal matrix having the characteristic impedance (Z_{0n}) of each port as a diagonal value. These impedance parameters will be used to determine the important electrical parameters of the capacitor.

4.3.3 Verification

To verify the simulation platform, the transmission characteristics of a LIGA microstrip stepped impedance low-pass filter are determined using HFSS. This filter was simulated, fabricated, and tested by Willke et al. [15]. The results obtained using HFSS are compared to the results obtained by Willke et al., to give confidence in the validity of the HFSS simulator for tall LIGA structures.

The layout of the stepped impedance filter [15], is shown in Figure 4.3, the relevant dimensions are shown in Table 4.1 and a scanning electron microscope (SEM) micrograph of the fabricated filter is shown in Figure 4.4. The microstrip filter was constructed using 220 μm thick electroplated nickel, on top of a 420 μm thick quartz substrate ($\epsilon_r = 3.81$ at 30 GHz). The ground plane was 0.75 μm thick gold. The filter was designed to have a 0.5 dB Chebyshev response. From presented

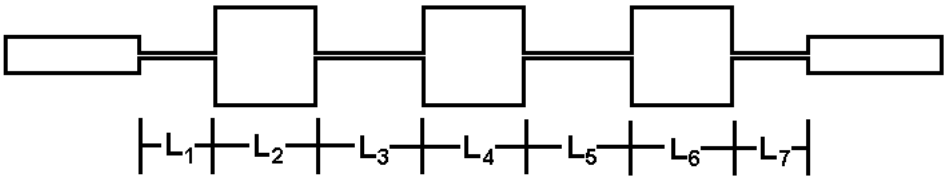

Figure 4.3: Verification model layout [15].

Table 4.1: Verification model dimensions [15].

Section	Width	Z_0	Length
1 and 7	100 μm	106 Ω	$L_1 = L_7 = 2.52$ mm
2 and 6	1.5 mm	35 Ω	$L_2 = L_6 = 2.7$ mm
3 and 5	100 μm	106 Ω	$L_3 = L_5 = 3.825$ mm
4	1.5 mm	35 Ω	$L_4 = 2.885$ mm

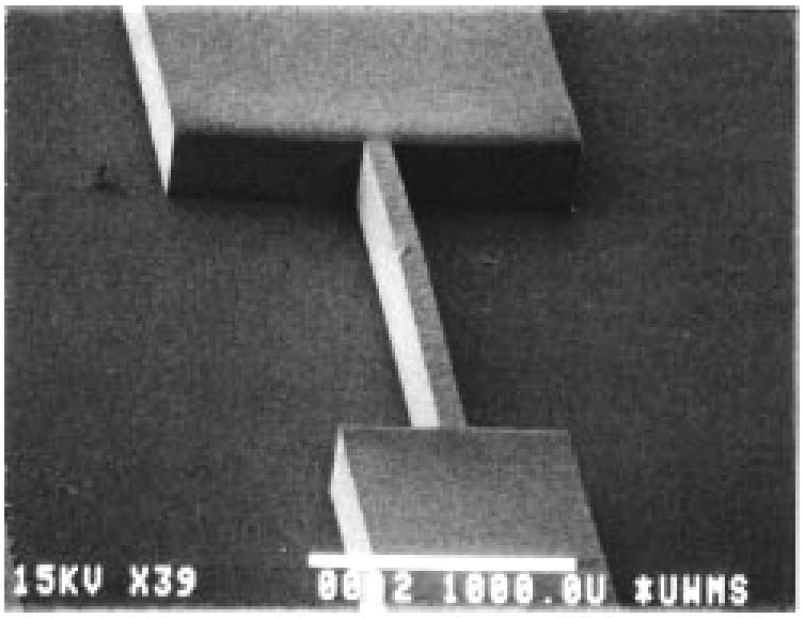

Figure 4.4: SEM micrograph of LIGA microstrip filter [15].

simulation results [15], the filter has a 3 dB cutoff frequency of 9.6 GHz and 20 dB attenuation at 12.2 GHz. The characteristic impedance of the filter sections was determined by Willke et al. using a 2-D FD analysis of the LIGA microstrip lines. The obtained characteristic impedances were used as input for the simulation of the filter using PUFF [50], which is a subnetwork calculation-based circuit analysis program for laying out and analyzing planar microstrip and stripline circuits. The simulation and test results obtained by Willke et al. are shown in Figure 4.5. The measured filter response is -3 dB at 9.22 GHz and reaches -20 dB at 11.4 GHz. The difference between simulated and measured results obtained by Willke et al. are 4.8% for the -3 dB point and 7.0% for the -20 dB point.

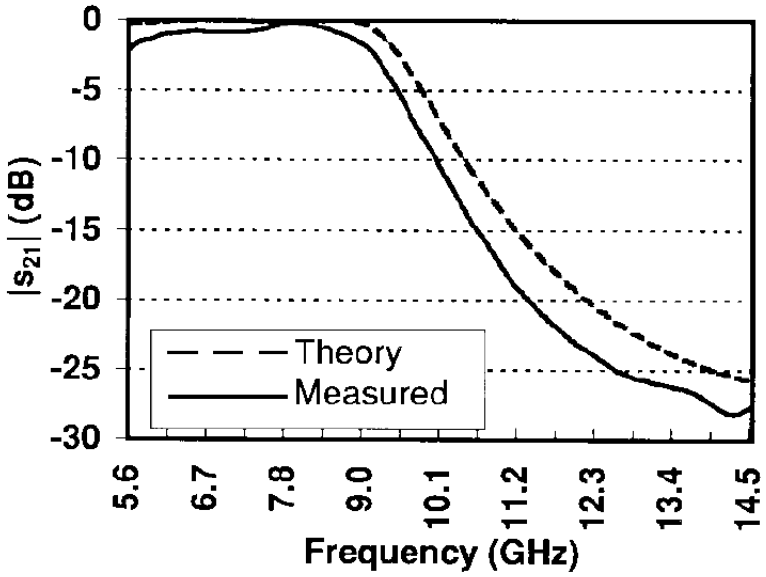

Figure 4.5: Simulation and test results for LIGA microstrip filter [15].

A full 3-D simulation of the filter was performed using HFSS. The HFSS model is shown in Figure 4.6, the material properties used in the simulation are listed in Table 4.2 and the simulation results are shown in Figure 4.7. In the model, the nickel conductors were placed on top of the quartz substrate. A large air box extends upwards from the substrate and surrounds the conductors. All outer surfaces of

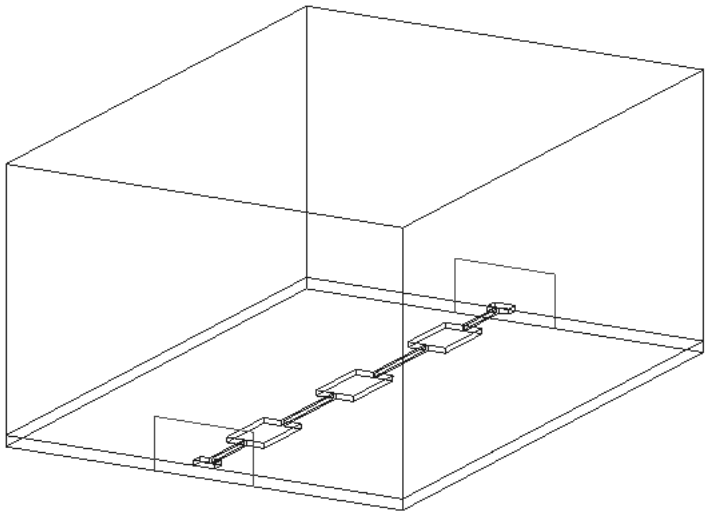

Figure 4.6: HFSS simulation model for LIGA microstrip filter.

Table 4.2: Electrical properties of materials used in verification.

Material	Nickel	Quartz	Air
Conductivity [S/m]	1.45×10^7	0	0
Rel. Permittivity (ϵ_r)	1	3.81	1
Rel. Permeability (μ_r)	600	1	1

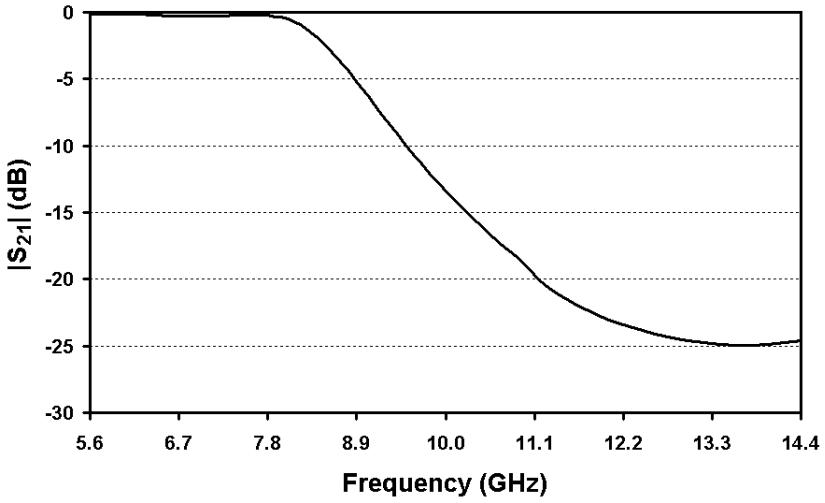

Figure 4.7: HFSS simulation results for LIGA microstrip filter.

the model interfacing the background are by default assumed perfect E boundaries (tangential component of the electric field is zero), which do not permit any energy to enter or leave. This includes the bottom surface of the substrate which is the ground plane. The ports enclose the nickel conductors and the bottom of the ports touch the ground plane. The size of the ports and air box follows the rules listed in the HFSS documentation [49]. A 10 iteration adaptive solution at 10 GHz was performed, resulting in approximately 18,000 tetrahedra. Following this, a discrete frequency sweep from 5 GHz to 15 GHz, in steps of 0.1 GHz, was performed with results shown in Figure 4.7. The simulated filter response shows -3 dB at 8.71 GHz and -20 dB at 11.14 GHz. The test results obtained by Willke et al. shows -3 dB at 9.22 GHz and -20 dB at 11.4 GHz. This results in a 5.5% difference for the -3 dB point and a 2.3% difference for the -20 dB point. The simulation results obtained using Ansoft HFSS are close enough to give confidence in the validity of the simulator for analyzing tall metal LIGA structures.

4.4 Two-Plate Capacitors

4.4.1 Cantilever Beams

Two two-plate cantilever beam capacitors were designed and simulated. A top view of the capacitors is shown in Figure 4.8 and a 3-D view is shown in Figure 4.9. Table 4.3 lists the relevant dimensions of the two capacitors. The metal height is 350 μm, an obtainable value with LIGA.

The capacitors are composed of three structures, a capacitance electrode and two ground structures. The ground structure on the right is included to facilitate testing with standard ground-signal-ground (GSG) wafer probes. The capacitor features a thin vertical cantilever adjacent to the capacitance electrode. The cantilever is grounded and is the only portion of the device that is not attached to the substrate. The radius of the connection between the cantilever and the fixed ground piece is 30 μm. There is a 5 μm air gap between the substrate and the cantilever, which occurs when the cantilever is released during etching of the seed layer. The capacitors

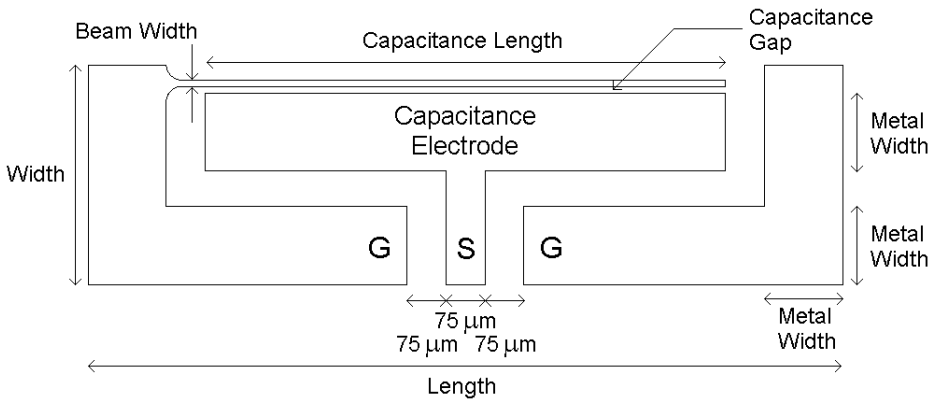

Figure 4.8: Top view of two-plate cantilever beam capacitor (capacitor A shown).

have a 345 μm thick device layer on top of a 5 μm thick titanium seed layer, for an overall height of 350 μm. Nickel and copper device layers were simulated using alumina as the substrate.

Applying a bias voltage between the capacitance electrode and the grounded cantilever causes an electrostatic force between the two. Since the cantilever is not attached to the substrate it deflects towards the capacitance electrode. This causes

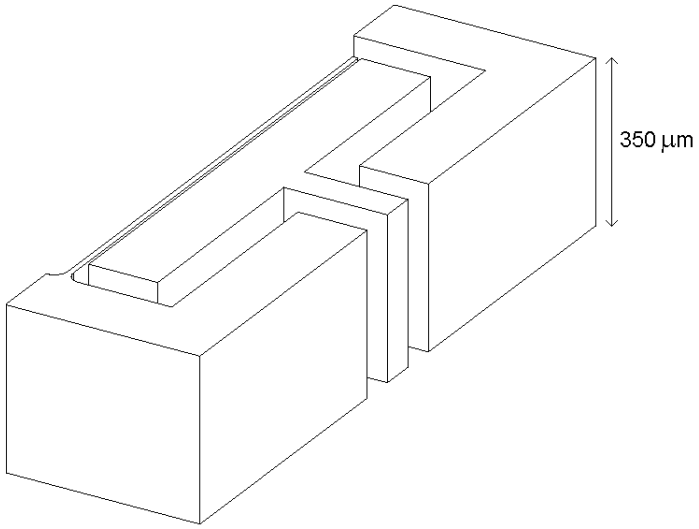

Figure 4.9: Three dimensional view of two-plate cantilever beam capacitor (capacitor A shown).

Table 4.3: Two-plate capacitor dimensions.

Capacitor	A	a
Length [μm]	1450	800
Width [μm]	414	259.5
Capacitance Length [μm]	1000	500
Metal Width [μm]	150	75
Beam Width [μm]	6	3
Capacitance Gap [μm]	3	1.5
Gap Capacitance [pF]	1.0	1.0

an increase in capacitance between the grounded cantilever and the capacitance electrode.

Capacitor A in Table 4.3 is a larger version of capacitor a. Both capacitors were designed for a gap capacitance of 1.0 pF. These geometries were selected to demonstrate the performance advantages obtainable, as the lateral dimensions of the capacitors are made smaller.

The high frequency characteristics of the devices were obtained using Ansoft HFSS. The capacitors were modeled as one-port structures with three-dimensional geometries as shown in Figure 4.9, and meshed using approximately 22,000 tetrahedral elements. This resulted in a maximum S-parameter difference of approximately 0.001 between iterations. A mesh size of approximately 22,000 tetrahedra was the maximum mesh that could be solved before the solution time became prohibitive. With 22,000 tetrahedra, the solution time on the author's computer for a single frequency solution is approximately one hour. To determine the operation of the device over a wide frequency range, a sweep of multiple frequency points was required. At one hour per point, solution times for a complete frequency sweep were extensive.

As mentioned previously, the capacitors were modeled with both nickel and copper device layers. This was done to observe the expected performance increase of

copper over nickel. A titanium seed layer was situated between the device layer and an alumina substrate. The electrical properties of the five materials are listed in Table 4.4.

Table 4.4: Electrical properties of materials used in simulations.

Material	Nickel	Copper	Titanium	Alumina	Air
Conductivity [S/m]	1.45×10^7	5.8×10^7	2.1×10^7	0	0
Rel. Permittivity (ϵ_r)	1	1	1	9.4	1
Rel. Permeability (μ_r)	600	1	1	1	1

With nickel as the device layer, the generalized S-parameters were obtained for frequencies from 1 GHz to 12 GHz in 0.25 GHz increments. A plot of S_{11} versus frequency is shown in Figure 4.10 for capacitor A and Figure 4.11 for capacitor a.

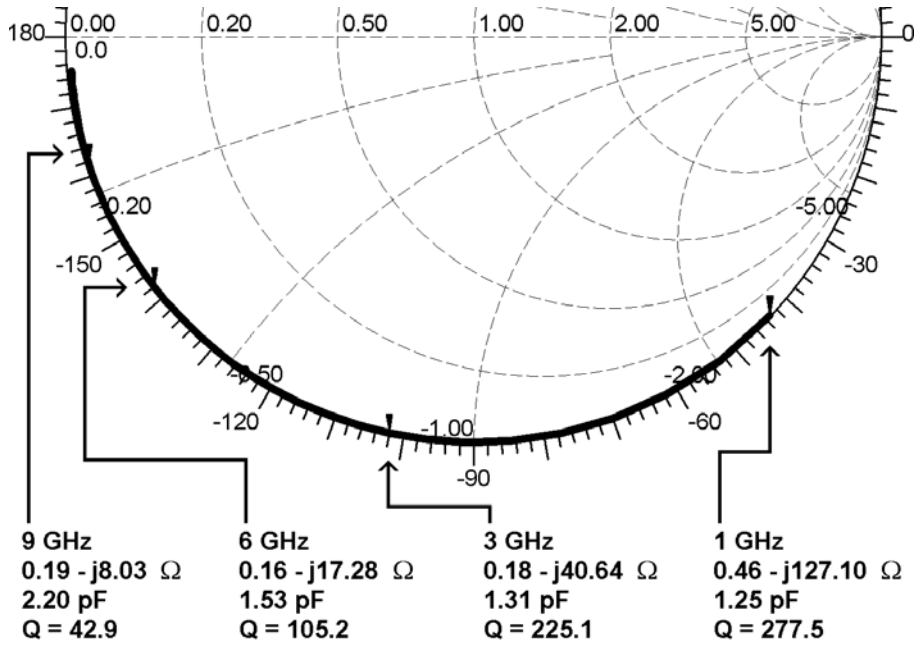

Figure 4.10: S_{11} for capacitor A with a nickel device layer.

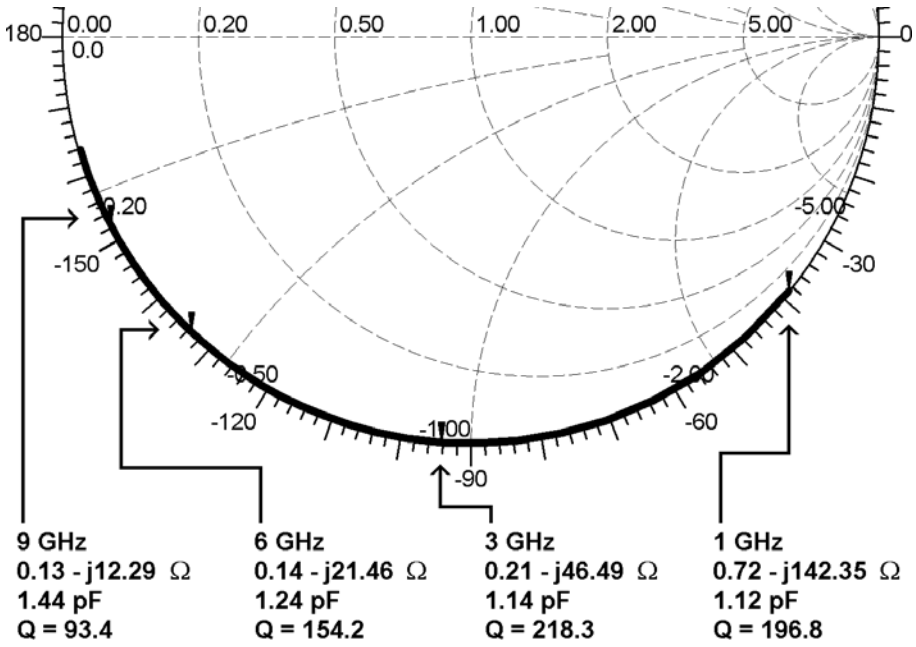

Figure 4.11: S_{11} for capacitor a with a nickel device layer.

The S-parameter data was renormalized to 50 Ω for plotting on the Smith chart. The impedance, Z_{11}, obtained from the original (not renormalized) generalized scattering parameters, is listed for a few common frequency points. The nominal capacitance value listed is obtained from the imaginary component of the impedance as follows

$$C = \frac{-1}{\omega \ \mathrm{im}(Z_{11})} \tag{4.9}$$

The Q-factor, assuming a series RC equivalent model, is the ratio of the imaginary component of the impedance to the real component.

$$Q = \left| \frac{\mathrm{im}(Z_{11})}{\mathrm{re}(Z_{11})} \right| \tag{4.10}$$

A few interesting observations can be made from these figures. The first observation is that capacitor A has a larger parasitic capacitance than capacitor a. This can be observed from the 1 GHz capacitance values. At 1 GHz the impedance from the associated inductance is very small and can be neglected. Therefore the impedance is due to the gap capacitance and the parasitic capacitance. Since the gap capacitance

is the same, the parasitic capacitance of capacitor A must be larger. This is likely due to the larger lateral dimensions of capacitor A. Capacitor A has more area between the capacitance electrode and the surrounding ground structures. The second observation is that capacitor A has a lower self-resonant frequency, indicating a larger associated inductance. This can be observed from the proximity of S_{11} to the centre-line of the Smith chart at 12 GHz (last frequency point). At the centre-line of the Smith chart the imaginary component of the impedance is zero. This is the point of electrical self-resonance. At 12 GHz capacitor A is closer to the centre-line than capacitor a, which implies a lower self-resonant frequency.

A summary of the results for the two capacitors at operational frequency is listed in Table 4.5. The operational frequency was defined as the closest integer frequency below the frequency where the imaginary component of the impedance is equal to 50 Ω. The self-resonant frequency was determined using HFSS by running single

Table 4.5: Two-plate cantilever beam capacitor results with a nickel device layer.

Capacitor	A	a
Operational Frequency [GHz]	2	2
Nominal Capacitance [pF]	1.27	1.13
Q-factor	269.9	222.0
Self-resonant Frequency [GHz]	13.3	18.6
Tuning Range	1.19:1	1.21:1
Tuning Voltage [V]	0-6.0	0-3.0

frequency simulations at various frequencies and locating the frequency where the imaginary component is equal to zero. The Q-factor for capacitor A is larger than the Q-factor for capacitor a at lower frequencies. This is likely due to the increased metal width of capacitor A, which results in lower resistance. At higher frequencies, the Q-factor of capacitor a becomes larger since capacitor a has a smaller associated

inductance. A plot of the capacitance change is shown in Figure 4.12. This plot was obtained by adding the static parasitic capacitance obtained using HFSS to the results obtained from ANSYS simulations. The tuning voltage is 0 - 6.0 V for capacitor A and 0 - 3.0 V for capacitor a. The tuning range is 1.19:1 for capacitor A and 1.21:1 for capacitor a. The tuning range is larger for capacitor a due to the fact that it has smaller parasitic capacitance.

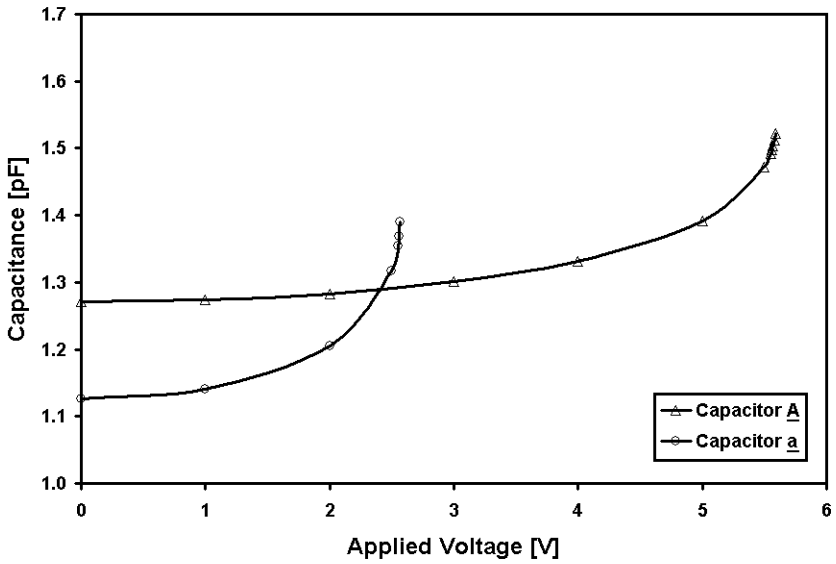

Figure 4.12: Capacitance change of the two-plate cantilever beam nickel devices at operational frequency.

With copper as a device layer, a summary of results at operational frequency is listed in Table 4.6. The mechanical parameters for copper used in the simulations were $E = 128$ GPa, and $v = 0.31$. The differences between the copper structures and the nickel structures are found in the Q-factor and the tuning voltage range. As expected, the Q-factor of the copper devices is significantly larger than the nickel devices. This results from the increase in conductivity of copper over nickel. The tuning voltage of the copper structures is smaller due to a lower elastic modulus.

Table 4.6: Two-plate cantilever beam capacitor results with a copper device layer.

Capacitor	A	a
Operational Frequency [GHz]	2	2
Nominal Capacitance [pF]	1.27	1.13
Q-factor	503.6	420.1
Self-resonant Frequency [GHz]	13.3	18.6
Tuning Range	1.19:1	1.21:1
Tuning Voltage [V]	0-5.1	0-2.5

4.4.2 Fixed-Fixed Beams

Two two-plate fixed-fixed beam capacitors, with geometries identical to the dimensions shown in Table 4.3 were simulated. The purpose was to highlight the differences in high frequency behavior between cantilever and fixed-fixed beam capacitors. A 2-D top view of the structures is shown in Figure 4.13. A 3-D representation is shown in Figure 4.14.

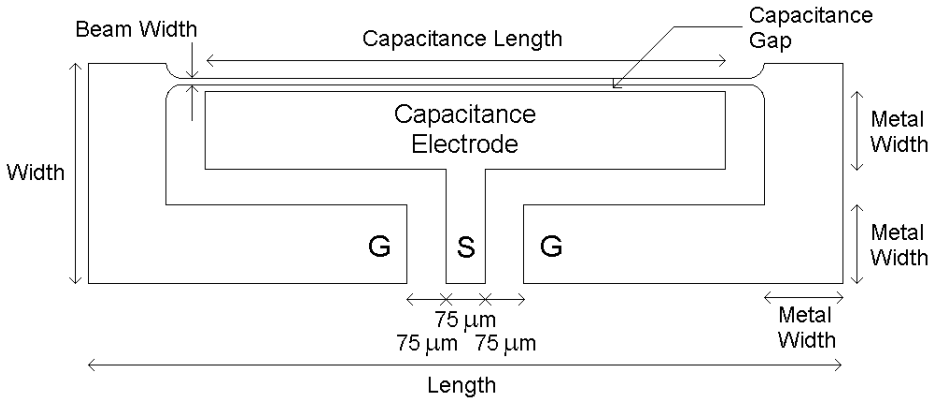

Figure 4.13: Top view of two-plate fixed-fixed beam capacitor (capacitor A shown).

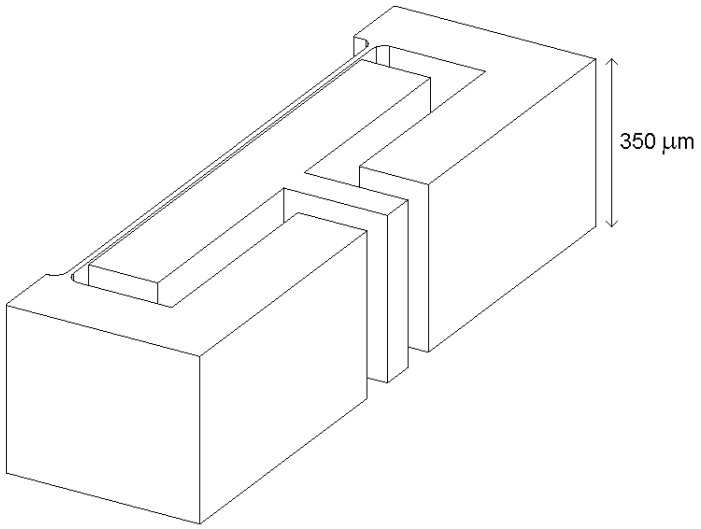

Figure 4.14: Three dimensional view of two-plate fixed-fixed beam capacitor (capacitor A shown).

The fixed-fixed beam capacitor is composed of only two structures as both ground pieces are attached to the beam. As in the cantilever beam case, nickel and copper device layers were simulated. Since the geometries are virtually identical to the cantilever beam capacitors, the gap capacitance for both fixed-fixed beam capacitors is also 1.0 pF. With nickel as the device layer, the capacitors were simulated at frequencies from 1 GHz to 12 GHz in 0.25 GHz increments. A plot of S_{11} versus frequency is shown in Figure 4.15 for capacitor A and Figure 4.16 for capacitor a.

As in the cantilever beam case, capacitor A has a larger parasitic capacitance and a smaller self-resonant frequency (larger associated inductance) than capacitor a. A summary of the results for the two capacitors at operational frequency is listed in Table 4.7. The main differences at higher frequencies between the cantilever and fixed-fixed beam capacitors are found in the self-resonant frequency and the Q-factor. The self-resonant frequency and the Q-factor of the fixed-fixed beam configuration is significantly higher. Since the gap capacitance and the parasitic capacitance is the same in both cases, the associated inductance of the fixed-fixed beam capacitor must be significantly smaller. The series resistance of the fixed-fixed beam capacitor

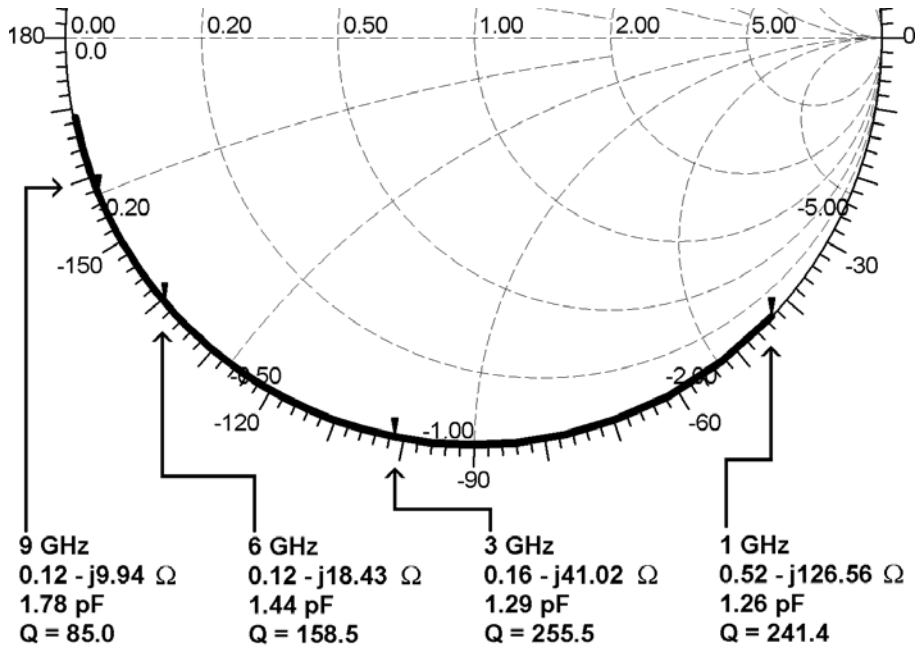

Figure 4.15: S_{11} for capacitor A with a nickel device layer.

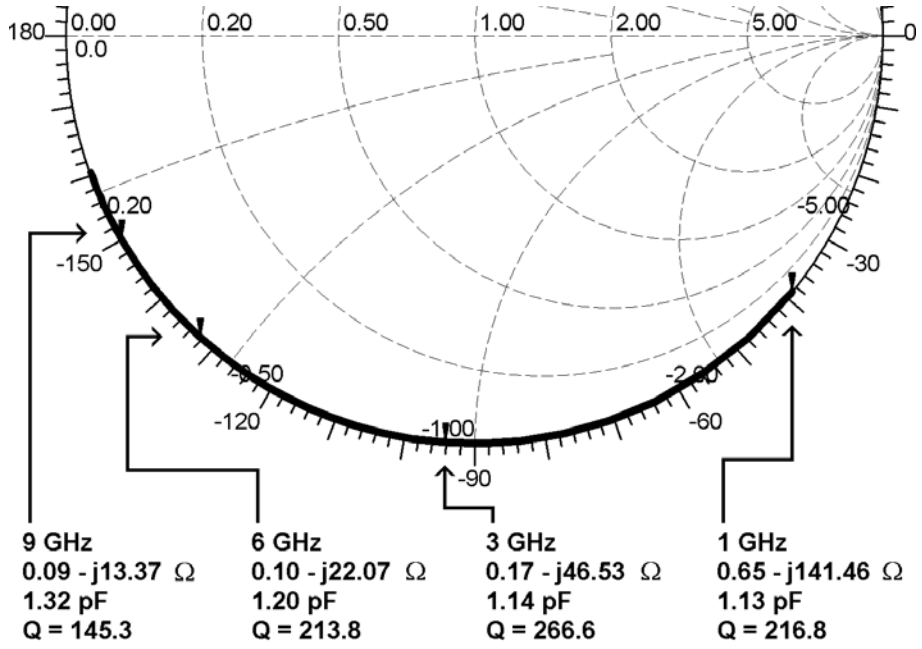

Figure 4.16: S_{11} for capacitor a with a nickel device layer.

Table 4.7: Two-plate fixed-fixed beam capacitor results with a nickel device layer.

Capacitor	A	a
Operational Frequency [GHz]	2	2
Nominal Capacitance [pF]	1.27	1.13
Q-factor	269.4	258.2
Self-resonant Frequency [GHz]	19.6	22.8
Tuning Range	1.22:1	1.25:1
Tuning Voltage [V]	0-39.0	0-19.5

appears to smaller as well. The reduction in inductance and resistance is due to both ends of the beam being grounded as opposed to one end.

Taking parasitic capacitance into account, a plot of the capacitance change is shown in Figure 4.17. The tuning voltage is 0 - 39.0 V for capacitor A and

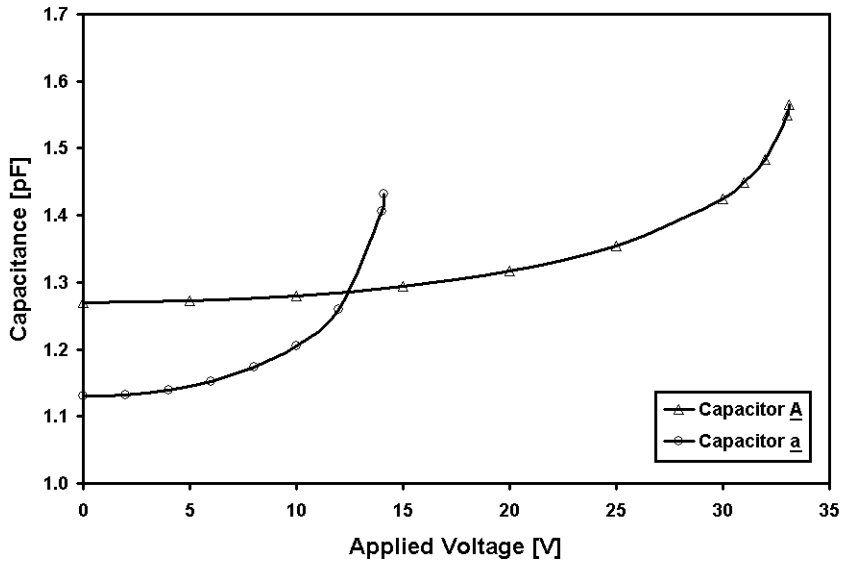

Figure 4.17: Capacitance change of the two-plate fixed-fixed beam nickel devices at operational frequency.

0 - 19.5 V for capacitor a. The tuning range is 1.22:1 for capacitor A and 1.25:1 for capacitor a. As shown in Chapter 3, the actuation voltage has been increased by a factor of 6.5 in the fixed-fixed beam case, and the tuning range has also been increased.

With copper as a device layer, a summary of results at operational frequency is listed in Table 4.8. As in the cantilever beam case, the Q-factor of the copper capacitors has been increased, while the tuning voltage has been decreased.

Table 4.8: Two-plate fixed-fixed beam capacitor results with a copper device layer.

Capacitor	A	a
Operational Frequency [GHz]	2	2
Nominal Capacitance [pF]	1.27	1.13
Q-factor	567.0	469.0
Self-resonant Frequency [GHz]	19.6	22.8
Tuning Range	1.22:1	1.25:1
Tuning Voltage [V]	0-33.0	0-16.5

4.5 Three-Plate Capacitors

4.5.1 Cantilever Beams

Six three-plate cantilever beam capacitors were designed and simulated. A 2-D top-view is shown in Figure 4.18, and a 3-D representation is shown in Figure 4.19. The relevant dimensions of the six capacitors are shown in Table 4.9. The capacitors are composed of four structures, an actuator electrode, a capacitance electrode, and two ground structures. The ground structure on the right is included to facilitate testing with standard wafer probes. In this configuration, the thin cantilever is situated between the two electrodes, and anchored to the ground piece on the left.

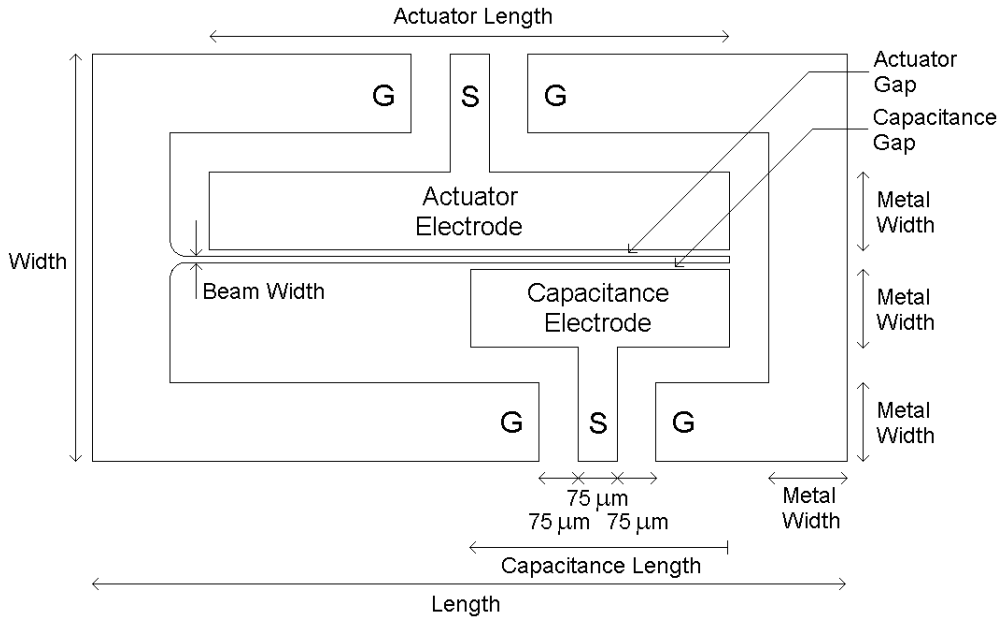

Figure 4.18: Top view of three-plate cantilever beam capacitor (capacitor B shown).

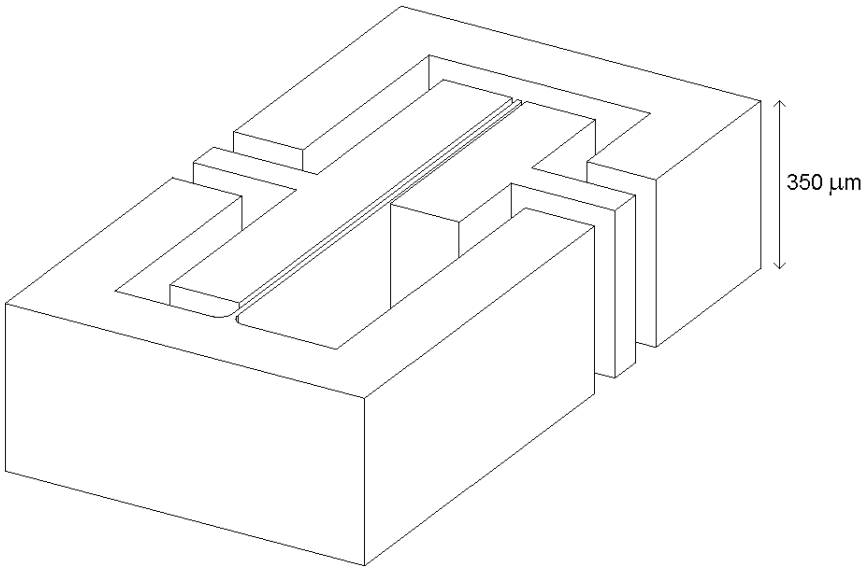

Figure 4.19: Three dimensional view of three-plate cantilever beam capacitor (capacitor B shown).

Table 4.9: Three-plate capacitor dimensions.

Capacitor	A	B	a	b	c	d
Length [μm]	1450	1450	800	800	800	800
Width [μm]	765	765	457.5	457.5	457.5	457.5
Actuator Length [μm]	1000	1000	500	500	500	500
Capacitance Length [μm]	1000	500	500	250	125	75
Metal Width [μm]	150	150	75	75	75	75
Beam Width [μm]	6	6	3	3	3	3
Capacitance Gap [μm]	3	3	1.5	1.5	1.5	1.5
Gap Capacitance [pF]	1.0	0.5	1.0	0.5	0.25	0.15

Applying a bias voltage between the actuator electrode and the grounded cantilever causes an electrostatic force between the two, which results in a deflection of the cantilever towards the actuator electrode. The capacitance between the cantilever and the grounded electrode is decreased. As shown in Chapter 3, this method can be used to increase the tuning range of the capacitor. This is only valid if the actuator gap is larger than the capacitance gap. For all capacitors in this section, the actuator gap is double the capacitance gap. Making the actuator gap larger than the values in Table 4.9 would result in an increase in tuning range at the expense of an increase in actuation voltage.

Capacitors A and a were designed for a gap capacitance of 1.0 pF, and have capacitance gap dimensions exactly the same as in the two-plate capacitor configurations. Both of these capacitors have capacitance lengths equal to the actuator lengths. In order for the capacitors to operate at higher frequencies, the capacitance lengths of capacitors B, b, c and d have been made smaller than the actuator lengths. This reduces the capacitance between the grounded cantilever and the capacitance electrode. Capacitors B and b were designed for a gap capacitance of 0.5 pF. Capacitors c and d have a gap capacitance of 0.25 pF and 0.15 pF respectively.

The capacitors were modeled as two-port structures with three-dimensional geometries as shown in Figure 4.19. With nickel as the device layer, the generalized S-parameters were obtained for the six devices. For capacitors A, B, a, and b, a frequency sweep from 1 GHz to 12 GHz was performed using 0.25 GHz increments. For capacitors c and d the upper limit of the frequency sweep was 15 and 18 GHz respectively. For capacitors A and a, the S_{11} versus frequency plots were identical to the plots shown for the two-plate cantilever beam capacitor configuration (Figure 4.10 and Figure 4.11). A plot of S_{11} versus frequency is shown in Figure 4.20 for capacitor B, Figure 4.21 for capacitor b, Figure 4.22 for capacitor c and Figure 4.23 for capacitor d.

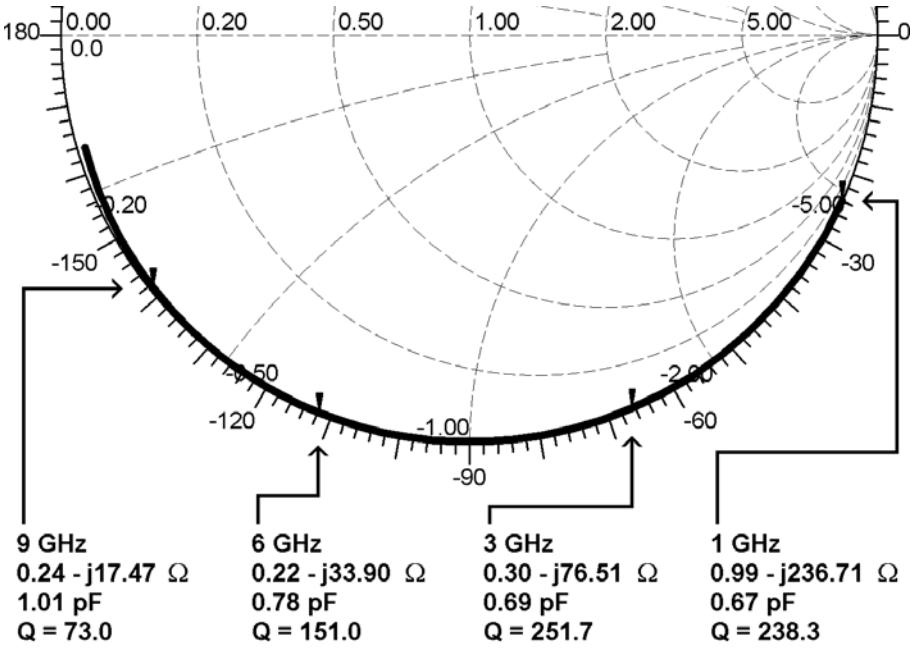

Figure 4.20: S_{11} for capacitor B with a nickel device layer.

A summary of the results for the six capacitors at operational frequency is listed in Table 4.10. For capacitors A and a, the tuning range and tuning voltage is larger than the two-plate capacitor configurations as expected. Neglecting parasitic capacitance, the tuning range for the capacitors should increase as the capacitance

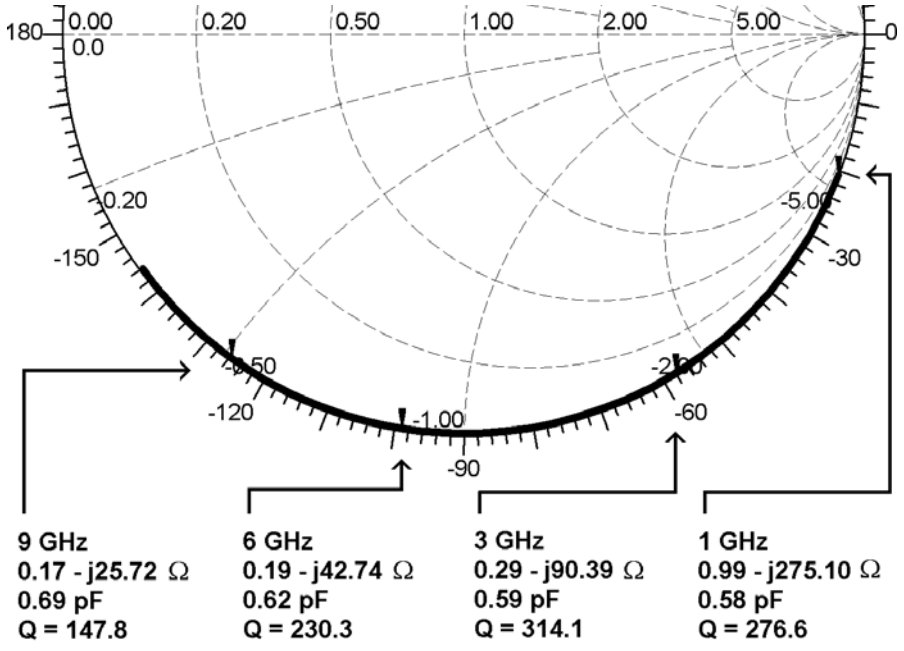

Figure 4.21: S_{11} for capacitor b with a nickel device layer.

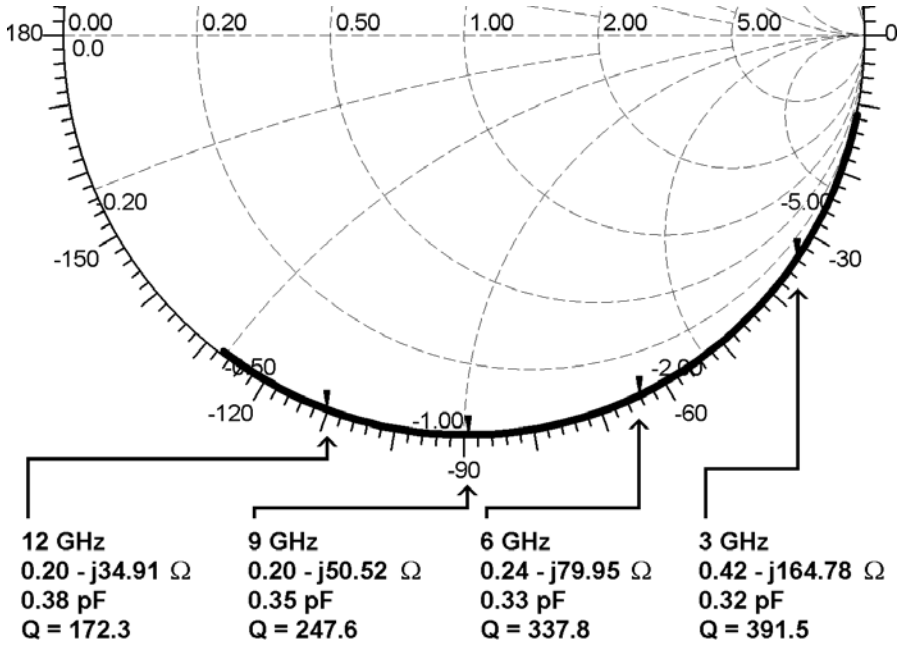

Figure 4.22: S_{11} for capacitor c with a nickel device layer.

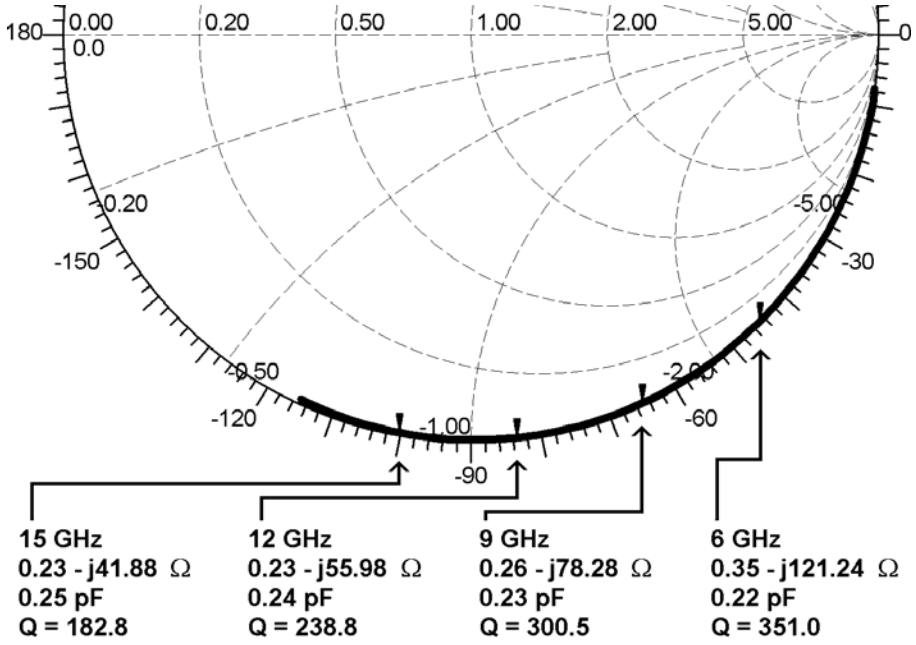

Figure 4.23: S_{11} for capacitor d with a nickel device layer.

Table 4.10: Three-plate cantilever beam capacitor results with a nickel device layer.

Capacitor	A	B	a	b	c	d
Operational Frequency [GHz]	2	4	2	5	9	13
Nominal Capacitance [pF]	1.27	0.71	1.13	0.61	0.35	0.24
Q-factor	269.9	220.2	222.0	262.2	247.6	219.0
Self-resonant Frequency [GHz]	13.3	14.5	18.6	21.5	27.8	33.7
Tuning Range	1.23:1	1.33:1	1.26:1	1.43:1	1.43:1	1.38:1
Tuning Voltage [V]	0-15.8	0-15.8	0-7.3	0-7.3	0-7.3	0-7.3

length is decreased. This is seen by comparing the tuning range of A to B and a to b. Since the deflection of the beam is largest at the end of the beam, as the capacitance length is made smaller, the tuning ratio increases. Capacitors c and d do not continue to show an increase in tuning range due to the parasitic capacitance. As the capacitance length is made smaller, the ratio of capacitance to parasitic

capacitance also decreases. This has the tendency to reduce the capacitance ratio. These two effects are opposing one another, which is why capacitors b and c have maximum tuning ranges.

By significantly reducing the capacitance length (capacitors c and d), the capacitance is made smaller, which permits high Q, high frequency operation. These two capacitors could be used in the 9 - 13 GHz frequency region due to their large self-resonant frequencies (27.8 GHz - 33.7 GHz).

Taking parasitic capacitance into account, a plot of the capacitance change of the six devices is shown in Figure 4.24. With copper as a device layer, a summary of results at operational frequency is listed in Table 4.11. As in the two-plate capacitor configurations, the Q-factor of the copper capacitors has been increased, while the tuning voltage has been decreased.

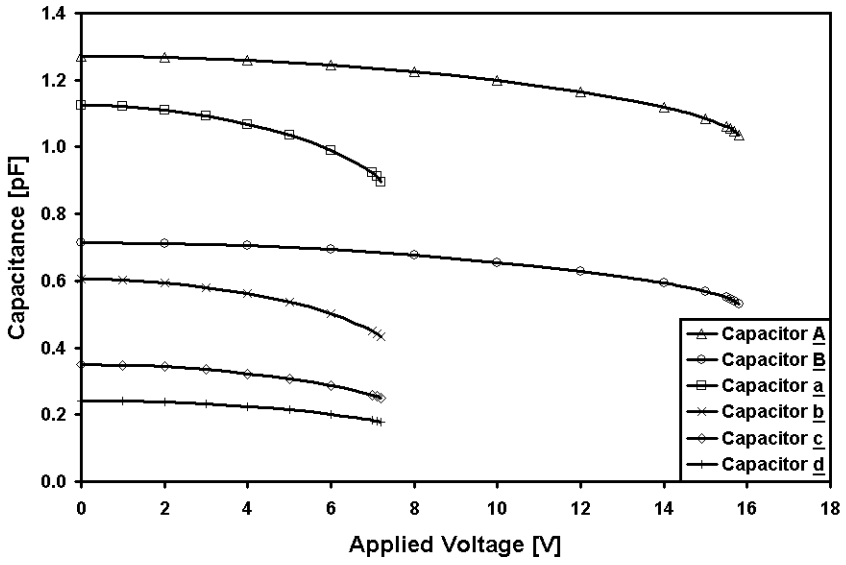

Figure 4.24: Capacitance change of the three-plate cantilever beam nickel devices at operational frequency.

Table 4.11: Three-plate cantilever beam capacitor results with a copper device layer.

Capacitor	A	B	a	b	c	d
Operational Frequency [GHz]	2	4	2	5	9	13
Nominal Capacitance [pF]	1.27	0.71	1.13	0.61	0.35	0.24
Q-factor	503.6	343.9	420.1	435.6	406.4	389.3
Self-resonant Frequency [GHz]	13.3	14.5	18.6	21.5	27.8	33.7
Tuning Range	1.23:1	1.33:1	1.26:1	1.43:1	1.43:1	1.38:1
Tuning Voltage [V]	0-13.2	0-13.2	0-6.1	0-6.1	0-6.1	0-6.1

4.5.2 Fixed-Fixed Beams

Six three-plate fixed-fixed beam capacitors, with geometries identical to the dimensions shown in Table 4.9 were simulated. A 2-D top view of the structures is shown in Figure 4.25. A 3-D representation is shown in Figure 4.26.

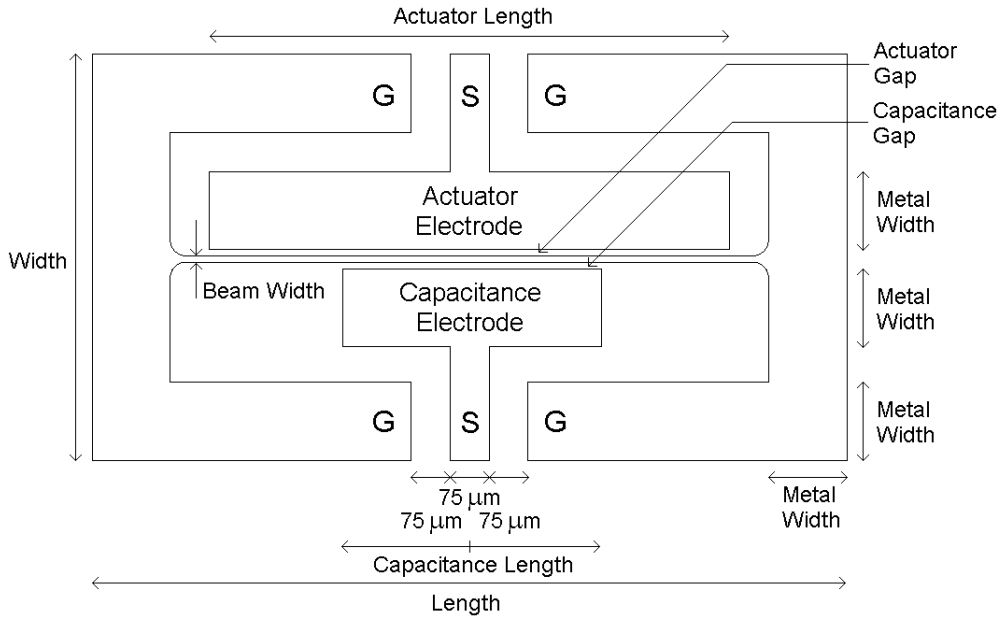

Figure 4.25: Top view of three-plate fixed-fixed beam capacitor (capacitor B shown).

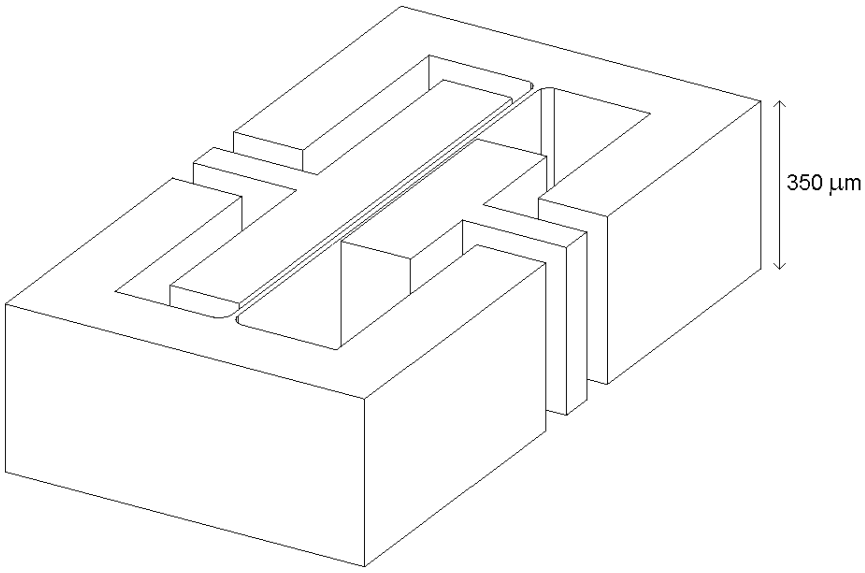

Figure 4.26: Three dimensional view of three-plate fixed-fixed beam capacitor (capacitor B shown).

The fixed-fixed beam capacitor is composed of only three structures as both ground pieces are attached to the beam. The devices were simulated at the same frequencies as in the cantilever beam case, using both nickel and copper device layers. For capacitors A and a, the S_{11} versus frequency plots were identical to the plots shown for the two-plate fixed-fixed beam capacitor configuration (Figure 4.15 and Figure 4.16). A plot of S_{11} versus frequency is shown in Figure 4.27 for capacitor B, Figure 4.28 for capacitor b, Figure 4.29 for capacitor c, and Figure 4.30 for capacitor d.

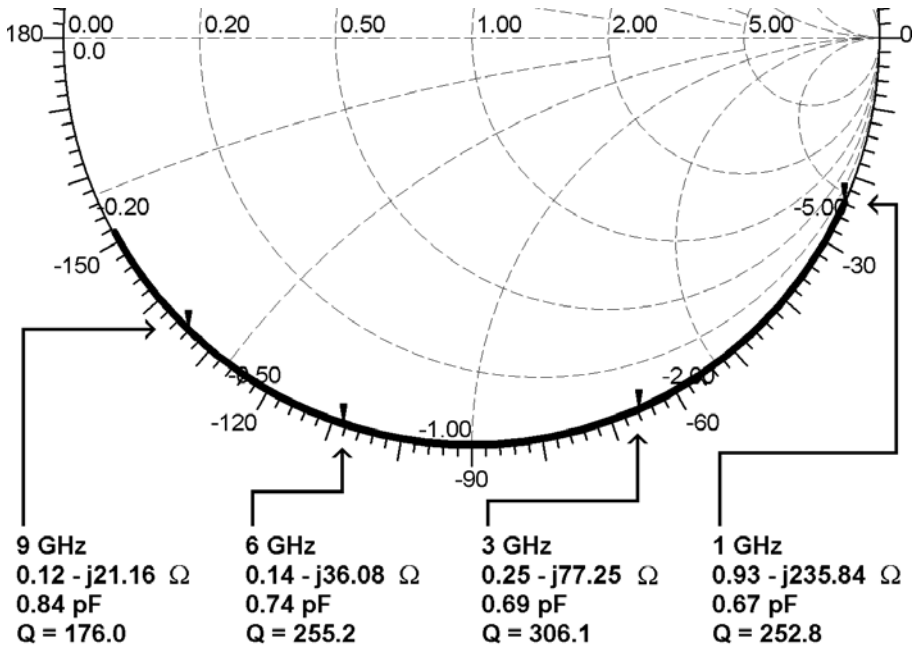

Figure 4.27: S_{11} for capacitor B with a nickel device layer.

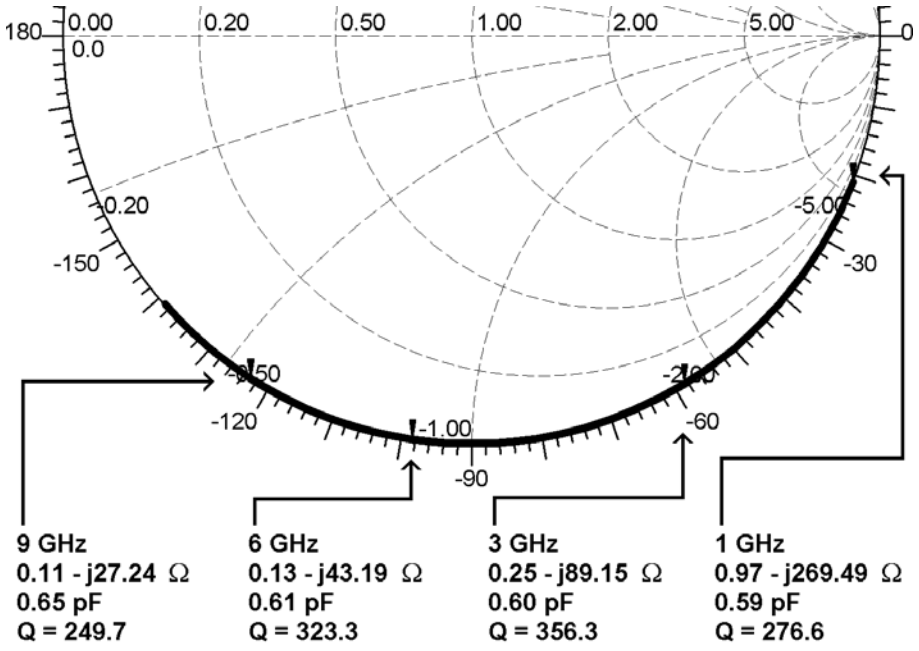

Figure 4.28: S_{11} for capacitor b with a nickel device layer.

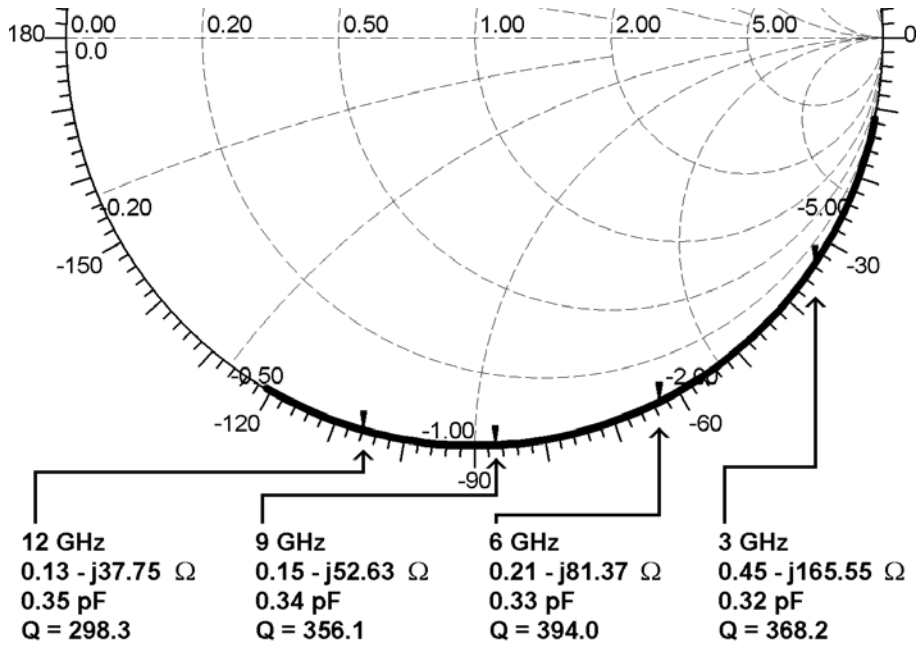

Figure 4.29: S_{11} for capacitor c with a nickel device layer.

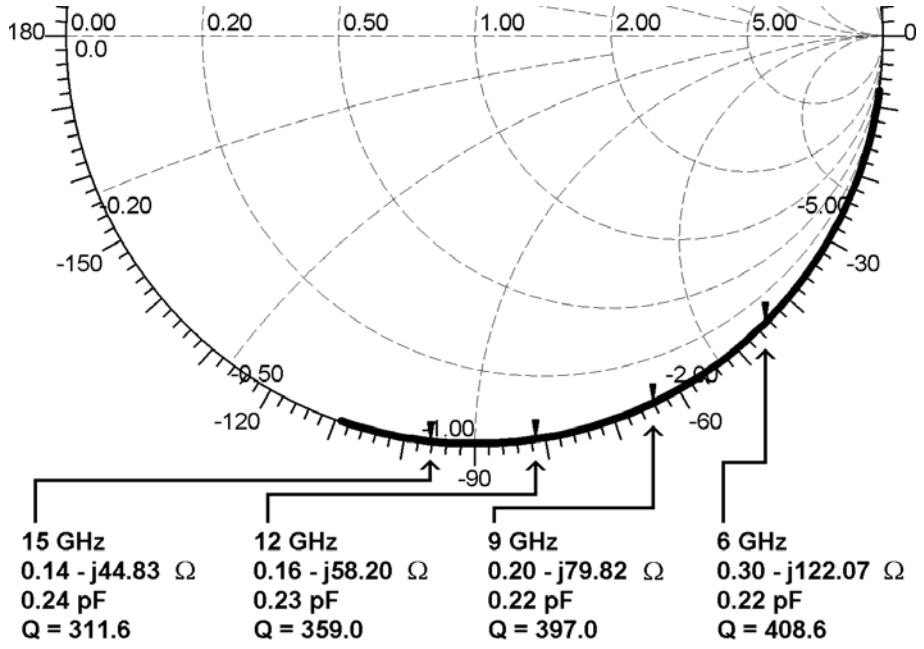

Figure 4.30: S_{11} for capacitor d with a nickel device layer.

A summary of the results for the six capacitors at operational frequency is listed in Table 4.12. Taking parasitic capacitance into account, a plot of the capacitance change of the six devices is shown in Figure 4.31.

Table 4.12: Three-plate fixed-fixed beam capacitor results with a nickel device layer.

Capacitor	A	B	a	b	c	d
Operational Frequency [GHz]	2	4	2	5	9	13
Nominal Capacitance [pF]	1.27	0.70	1.13	0.61	0.34	0.23
Q-factor	269.4	298.1	258.2	343.4	356.1	343.7
Self-resonant Frequency [GHz]	16.3	19.6	22.8	28.8	37.8	45.7
Tuning Range	1.29:1	1.41:1	1.37:1	1.51:1	1.48:1	1.41:1
Tuning Voltage [V]	0-93.9	0-93.9	0-40.1	0-40.1	0-40.1	0-40.1

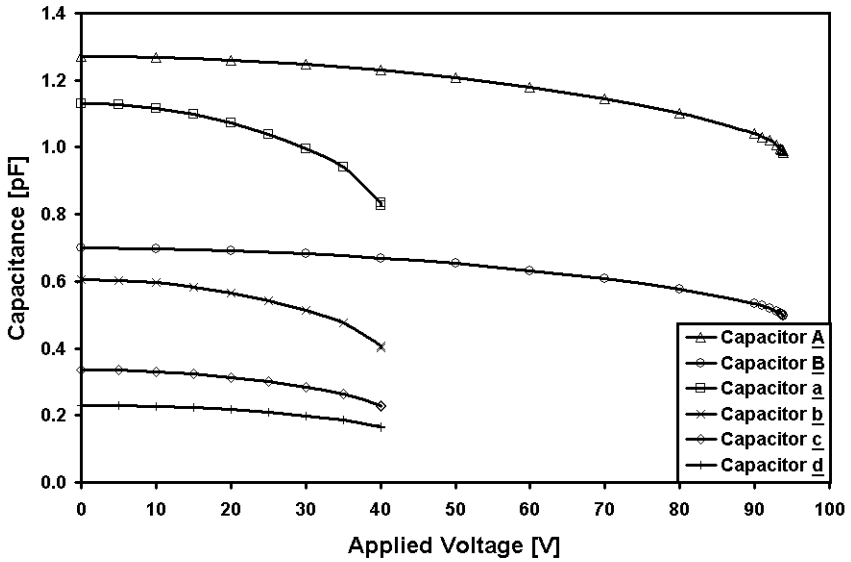

Figure 4.31: Capacitance change of the three-plate fixed-fixed beam nickel devices at operational frequency.

With copper as a device layer, a summary of results at operational frequency is listed in Table 4.13. As in the two-plate capacitors, the self-resonant frequency and Q-factor of the fixed-fixed beam configuration is significantly higher.

Table 4.13: Three-plate fixed-fixed beam capacitor results with a copper device layer.

Capacitor	A	B	a	b	c	d
Operational Frequency [GHz]	2	4	2	5	9	13
Nominal Capacitance [pF]	1.27	0.70	1.13	0.61	0.34	0.23
Q-factor	567.0	506.9	469.0	493.4	635.5	610.7
Self-resonant Frequency [GHz]	16.3	19.6	22.8	28.8	37.8	45.7
Tuning Range	1.29:1	1.41:1	1.37:1	1.51:1	1.48:1	1.41:1
Tuning Voltage [V]	0-79.4	0-79.4	0-33.9	0-33.9	0-33.9	0-33.9

4.6 Summary

LIGA-MEMS variable capacitors with different geometries were designed and simulated. Two-plate capacitors were shown to be capable of operation with low tuning voltages, but have a small tuning range. Three-plate capacitors are capable of increased tuning range at the expense of an increase in actuation voltage. In all configurations, two different sizes of capacitors were simulated. The capacitors with smaller lateral dimensions showed a decrease in associated inductance which leads to an increase in self-resonant frequency and Q-factor at higher frequencies. Capacitors with cantilever and fixed-fixed beam configurations were simulated. The fixed-fixed beam capacitors have larger tuning voltages as expected, but also showed an increase in self-resonant frequency and Q-factor, which was attributed to a decrease in associated inductance and resistance, due to both ends of the beam being fixed. By reducing the length of the capacitance electrode, the capacitance decreases, but

an increase in tuning voltage is obtained. A reduction in the length of the actuator electrode could also have been used to increase the tuning range but would lead to an increase in tuning voltage. Capacitors were simulated with both nickel and copper device layers, with copper device layers showing an increase in Q-factor and a decrease in tuning voltage.

5. CAPACITOR FABRICATION AND TESTING

5.1 Mask Layout

The devices were fabricated at Forschungszentrum Karlsruhe (FZK), a national laboratory in Germany. Samples were processed by IMT (Institute for Microstructure Technology), including the X-ray exposure at the FZK storage ring ANKA. The first step in the fabrication of the capacitors was to design and layout a mask. A picture of the overall mask is shown in Figure 5.1. The overall layout size of standard

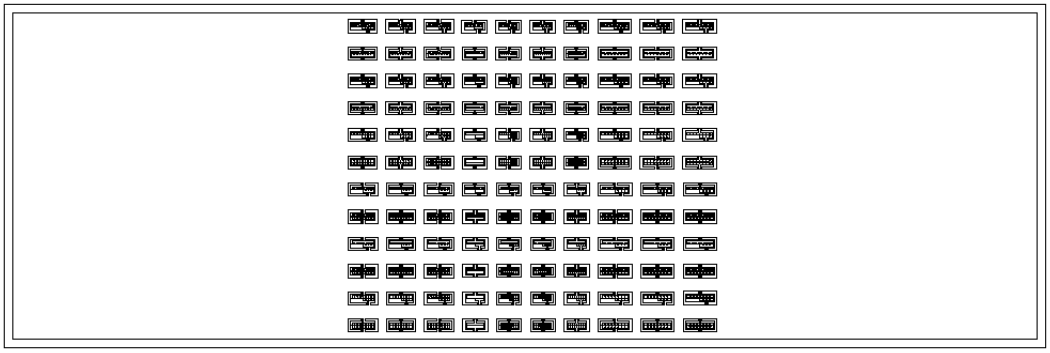

Figure 5.1: Mask layout.

masks used at the IMT is 20 mm by 60 mm. This is the size of the outer rectangle in Figure 5.1. The area allotted for the capacitors was approximately 40% of the overall mask, which was shared with another user.

The mask layout includes 60 capacitors with varied sizes and feature geometries. A larger view of all the capacitors is shown in Figure 5.2. The capacitors are composed in 2 identical grids (A-F; a-f) of 6 rows and 10 columns to ensure redundancy

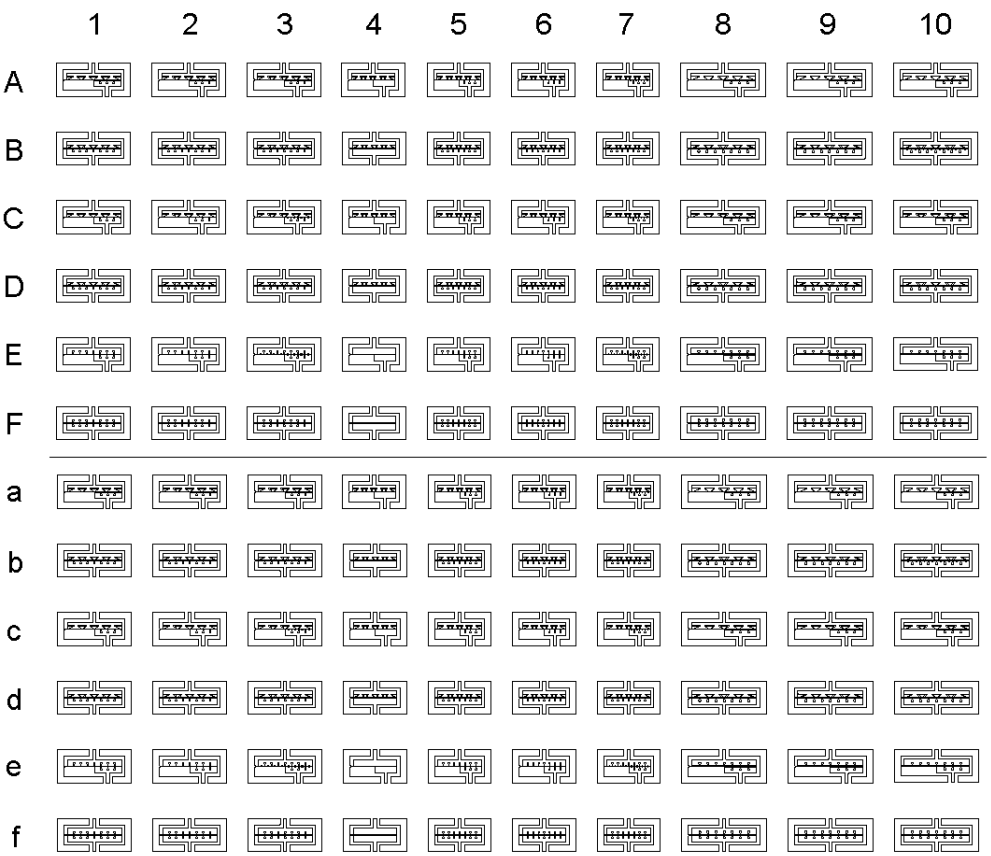

Figure 5.2: Capacitor grid from mask layout.

for every individual device.

The capacitors were designed for a metal height of 350 μm. Usually, the developed resist voids are electroplated to 70% of the resist height. Therefore a 500 μm thick resist foil could be used. A design constraint placed on the capacitors was that they were not to have actuation voltages greater than 40 V, as the network analyzer that was used has a maximum bias voltage of 40 V. It was therefore decided that no fixed-fixed beam capacitors would be included in the layout. For an initial fabrication attempt, feature sizes required for fixed-fixed beam actuation voltages below 40 V would be too small.

All capacitors were designed with a gap capacitance of either 1.0 pF or 0.5 pF. The 1.0 pF designs are in rows B, D, and F. The 0.5 pF designs are in the remaining

rows A, C, and E. The capacitor pairs (A-B, C-D, and E-F), in the same column, have identical layouts except that the 0.5 pF designs have capacitance electrode lengths that are half as long as the 1.0 pF designs.

Three sizes of capacitors were developed. The smallest capacitors are in columns 4-7, columns 1-3 contain larger devices, and the largest capacitors are in columns 8-10. Capacitors E4 and F4 are identical to the large three-plate cantilever beam capacitors A and B from simulations. A summary of specific capacitor dimensions from the layout, is listed in Table 5.1. The labels are consistent with the simulated capacitors as shown in Figure 4.18. The metal width for all devices is 150 μm (Figure 4.18).

Table 5.1: Capacitor dimensions from layout.

Columns	1-3	4-7	8-10
Length [μm]	1700	1450	1950
Width [μm]	768.75	765	772.5
Actuator Length [μm]	1250	1000	1500
Beam Width [μm]	7.5	6	9
Actuator Gap [μm]	7.5	6	9
Capacitance Gap [μm]	3.75	3	4.5

Stoppers limiting the beam deflection were added to some of the capacitors in the layout to ensure no electrical short can occur during actuation. Capacitors in rows E and F have no stoppers. Capacitors in rows A and B have stoppers that are placed far from the beam. Capacitors in rows C and D have stoppers that are placed close to the beam. For the devices with stoppers placed far from the beam, the stopper gap is 2/3 of the actuator gap. For stoppers placed close to the beam, the stopper gap is 1/3 of the actuator gap. The two different stopper gap locations were chosen to test devices with and without hysteresis.

The layout and desired structure height requires extremely high aspect ratios (structure height / minimum feature size). This is very challenging for any micro-fabrication process. In order to improve the probability of successfully fabricated devices as given in Figure 4.18 some modifications were made to the general layout of the capacitors as shown in Figure 5.3 (capacitor E7). Capacitor E7 is a 0.5 pF design and has no stoppers. Two changes were made to improve fabrication. The

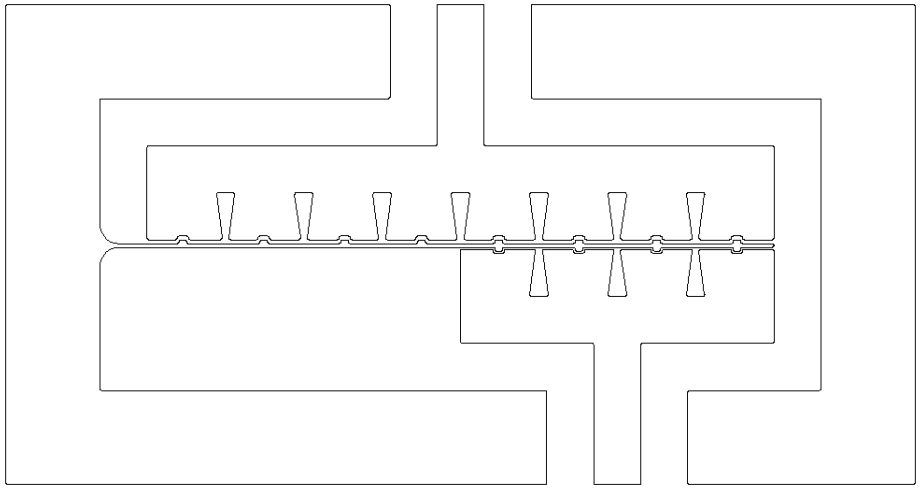

Figure 5.3: Layout of capacitors E7 and e7.

first change is that periodic widening was added to the beam. This takes the form of periodic "bumps" on the beam. This increases the mechanical stability of the long and high, but narrow PMMA/metal walls by raising the geometrical moment of inertia. It also slightly increases the diffusion of developer into the resist. The adjacent electrodes follow the profile of the beam to minimize the effects on the capacitance by maintaining the gap width. The second change are the triangular voids in the actuator and capacitance electrodes (resist relief), which relates to triangularly supported PMMA walls. This is done for two reasons. First, it will tend to anchor the small gap resist so it is not broken off or deformed during development and electroplating. Second, it will allow the HF acid to get into the small gap while

etching the seed layer.

Figure 5.4 is the layout of capacitor C7. This is a 0.5 pF capacitor with stoppers close to the beam. The stoppers are the large triangles that are embedded within

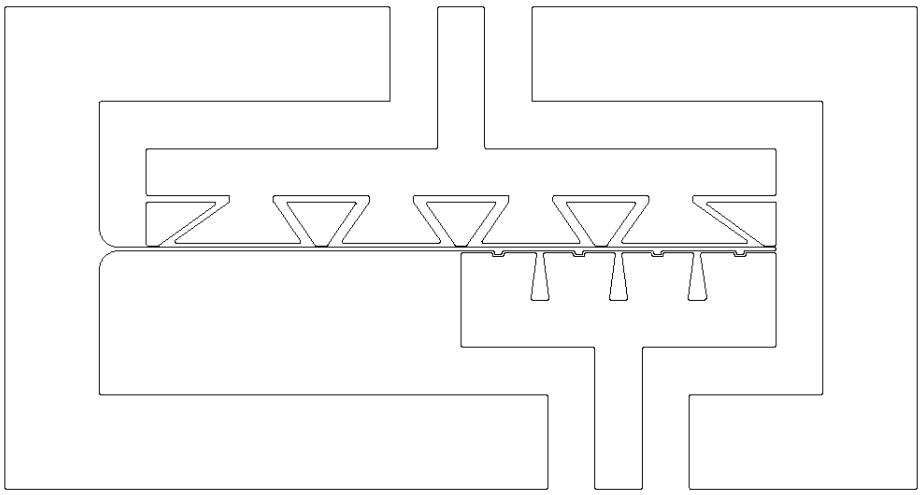

Figure 5.4: Layout of capacitors C7 and c7.

the actuator electrode. These triangles are electrically isolated from the actuator electrode. The triangle tips lie between the beam and the actuator. This prevents the beam from deflecting further than the tips of the triangles.

For the smallest capacitors (columns 4-7), column 4 is the originally designed capacitors without resist relief or periodic widening of the beam. Columns 5 and 6 are identical and contain resist relief. Column 7 contains resist relief and periodic widening of the beam. For the next larger capacitors (columns 1-3), columns 1 and 2 are identical and contain resist relief. Column 3 contains resist relief and periodic widening of the beam. For the largest capacitors (columns 8-10), columns 8 and 9 are identical and contain resist relief. Column 10 contains resist relief and periodic widening of the beam.

5.2 Capacitor Fabrication

It was decided that for an initial attempt, 100 μm tall structures would be fabricated. These devices are very challenging to fabricate due to the required high aspect ratios of the beams and gaps and it was felt that 350 μm might be too ambitious for an initial attempt. IMT X-ray lithography processes were used for fabrication, and X-ray exposure was done using the 2.5 GeV ANKA storage ring and beamline Litho-2. The substrate used was a 1 mm thick alumina wafer with a 3 μm oxidized titanium seed layer and 150 μm layer of PMMA photoresist. This sample was exposed to X-rays through a mask consisting of 20 μm thick gold absorbers on a 2.7 μm thick titanium membrane. Following the irradiation, the exposed resist was developed with GG developer. The voids in the resist were filled with electroplated nickel to a thickness of 100 μm. The remaining resist was then flood exposed and removed using another step of development. The structure was then descummed in oxygen plasma and wet etched with 5% HF acid for 2 minutes to remove the seed layer, electrically isolating the capacitor structures. This isotropic etching also underetches all structures, selectively releasing the thin beam, while still providing good adhesion of the large metal parts.

An optical micrograph of all the fabricated devices is shown in Figure 5.5. An enlarged view of devices b4, b5, c4, and c5 is shown in Figure 5.6.

A scanning electron microscope (SEM) micrograph of capacitor f10 is shown in Figure 5.7. This picture demonstrates the large aspect ratios that have been obtained using the LIGA process. The capacitance gap of this specific device is approximately 1.6 μm with a metal height of 100 μm. This results in an aspect ratio of 62. Other devices have an even larger aspect ratio. Figure 5.7 also indicates that the capacitance gap, beam width, and actuator gap slightly vary from the specifications in the layout due to process influences such as thermal effects and resist swelling. For this particular device (f10), the values for the three parameters are approximately 1.6 μm, 11.9 μm, amd 6.0 μm respectively. The values of these parameters in the layout are 4.5 μm, 9.0 μm, and 9.0 μm respectively. From this

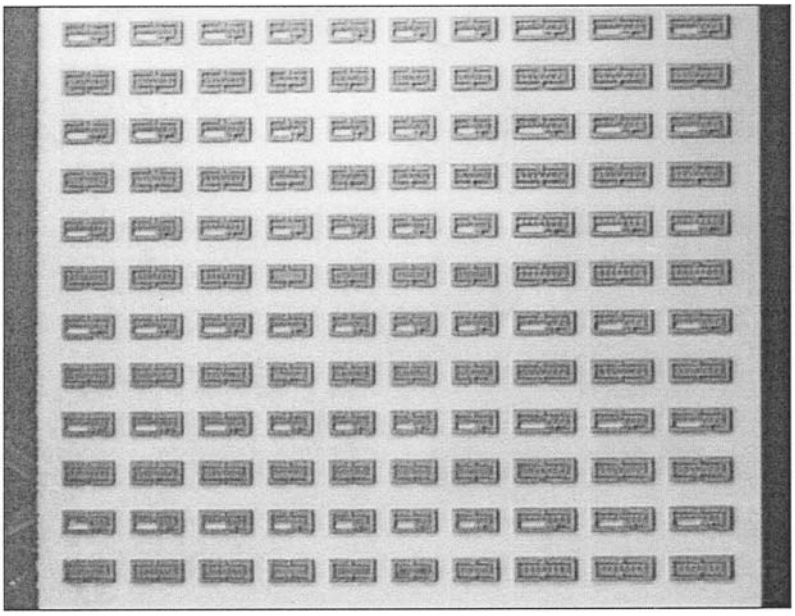

Figure 5.5: Optical micrograph of all devices (FZK/IMT).

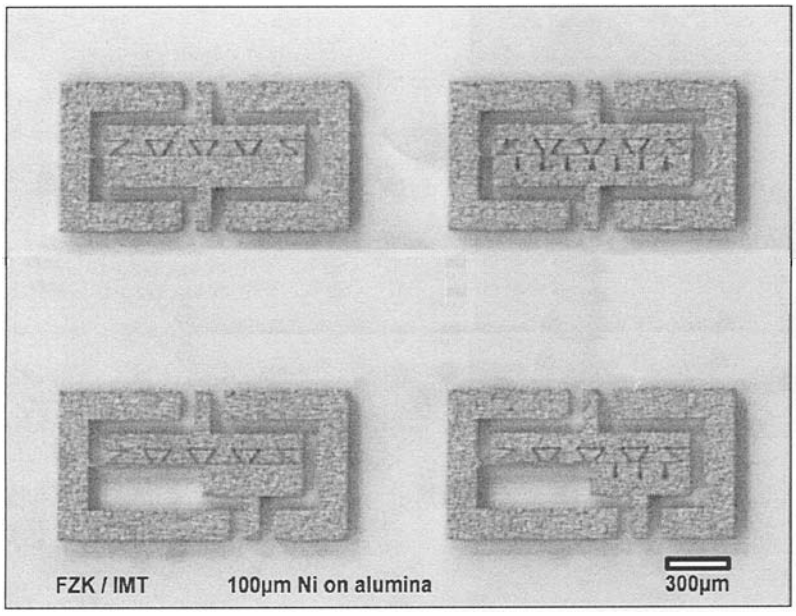

Figure 5.6: Optical micrograph of capacitors b4, b5, c4, and c5 (FZK/IMT).

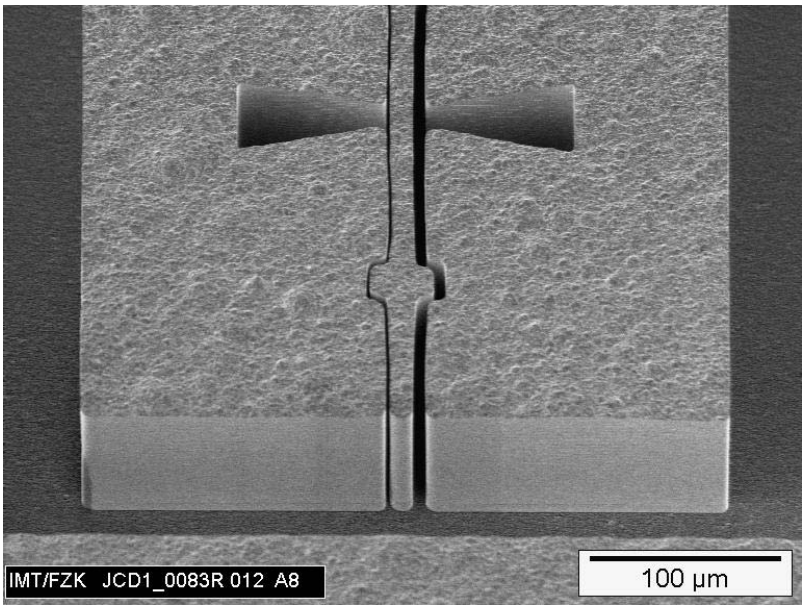

Figure 5.7: SEM micrograph of capacitor f10 (FZK/IMT).

picture the electrode voids and periodic widening of the beam can be easily observed. As well the rounding of the corners was done to prevent the photoresist from cracking during processing.

Some devices were lost during X-ray lithography due to resist breaking and loss of resist adhesion. Additional devices were deformed during the electroplating process which can be attributed to resist swelling, thermal expansion and evacuation effects. The only devices without deformations were the devices with periodic widening of the beam and triangular voids in the actuator and capacitance electrodes. The deformation can be seen in Figure 5.8, which is an SEM micrograph of capacitor c10. This is a 0.5 pF device with stoppers close to the beam. The deformation of the beam as well as the actuator electrode can be easily seen. This might have been avoided with modified plating conditions and relaxed geometrical requirements. The fabricated devices with no apparent deformations were capacitors f3, E10, F10, e10, and f10. All devices with stoppers had deformations present. This was likely due to the close proximity of the stoppers to the beam.

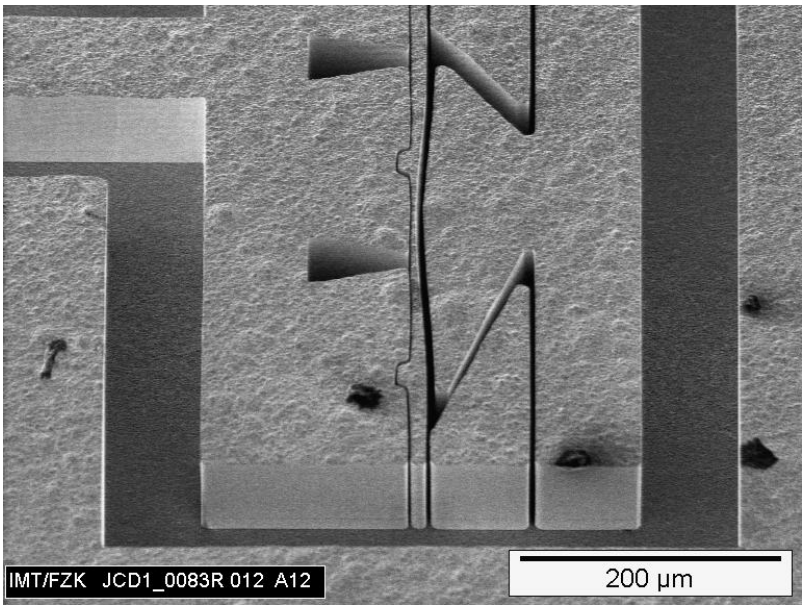

Figure 5.8: SEM micrograph of capacitor c10 (FZK/IMT).

5.3 Capacitor Testing

The capacitors that were free of deformations were tested using an Agilent 8722ES vector network analyzer. The analyzer was connected to the devices using a coaxial cable terminated with a Cascade ACP40-W-GSG-150 microprobe. This is a tungsten ground-signal-ground (GSG) probe with a pitch (centre-to-centre spacing of adjacent probe fingers) of 150 μm and a maximum frequency of 40 GHz. Tungsten probes were used because the nickel surface was found to be too hard for the standard beryllium copper (BeCu) probes. The microprobe is attached to a micropositioner, which provides fine motion for positioning the probe onto the capacitor.

Calibration of the test setup must be performed to eliminate the influence of the test setup on the measurement results. The calibration procedure used is a commonly used procedure called a short-open-load-thru (SOLT) calibration. By measuring known impedance standards, the effects of the test setup can be automatically removed by the vector network analyzer. To perform this, a Cascade 005-016 calibration impedance standard substrate (ISS) was used. This substrate

provides the short, load, and thru standards. The open standard is implemented with the probes in the air. Since the measurements to be made are 1-port measurements, the thru standard is not used, as it is only relevant to 2-port measurements. These 3 known impedances, short-open-load, are used to eliminate the effects of the test setup from the measurement results.

Early during testing, it was determined that many of the devices that were not deformed, had structures that were not electrically isolated. The impedance of the device on the capacitance gap side was inductive, indicating that the beam was connected to the capacitance electrode. This is due to some seed layer metal remaining between the beam and capacitance electrode after HF etching. The impedance of these devices on the actuator gap side was capacitive as expected, indicating that the seed layer had been adequately removed from the actuator gap. Of the 5 devices that were not deformed, only device f10 did not have any adjacent structures that were electrically connected. The real component of the measured impedance is shown in Figure 5.9 and the imaginary component is shown in Figure 5.10.

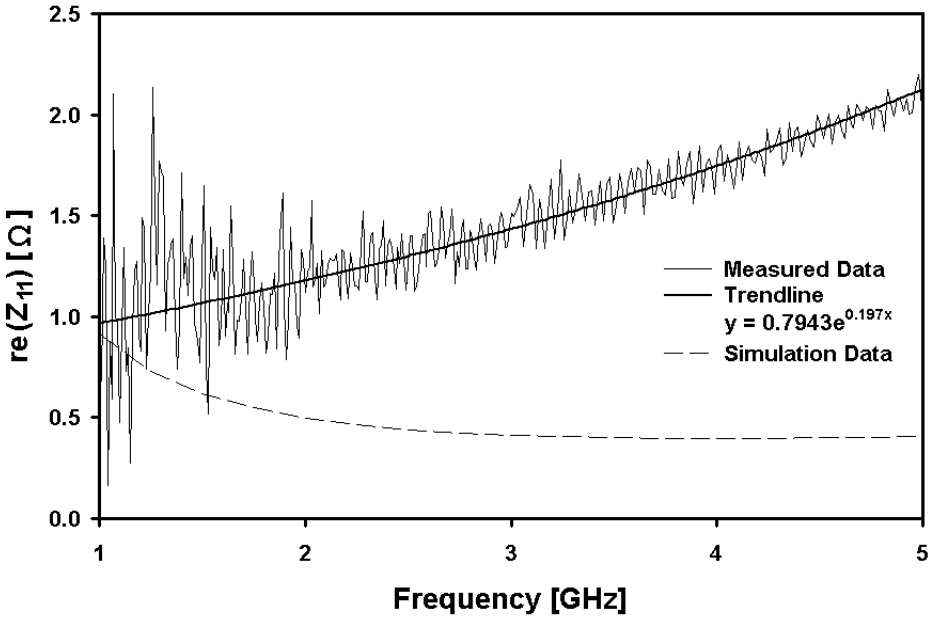

Figure 5.9: Real component of impedance re(Z_{11}) of capacitor f10.

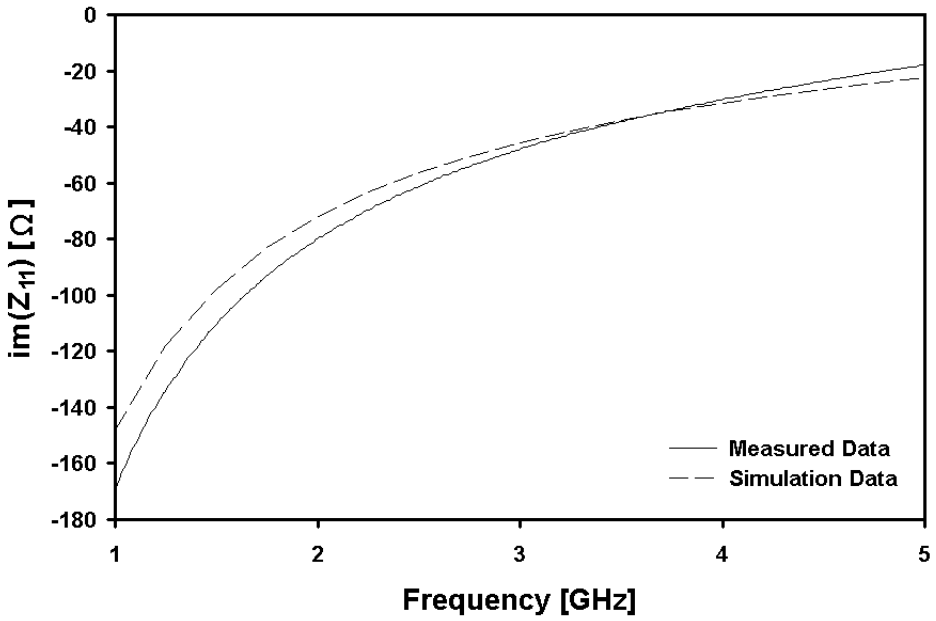

Figure 5.10: Imaginary component of impedance im(Z_{11}) of capacitor f10.

The measurements were performed over 2 frequency bands. The chosen frequency bands were 1 - 3 GHz and 3 - 5 GHz. In general, the measurement is more accurate if the calibration is done over a smaller frequency range because the input bandwidth of the network analyzer's receiver will be smaller.

The real component of the impedance is quite erratic (especially at low frequencies), but appears to follow a definite trend as shown with the trendline. When the frequency is low, the magnitude of the impedance is large, therefore the error in the small real component of the impedance will be larger at low frequencies. The trendline was created by finding the least squares fit through points using the equation $y = ae^{bx}$, where a and b are constants. In the trendline equation in Figure 5.9, x is the frequency in GHz and y is the real component of the impedance in ohms. An exponential trendline was used because it resulted in a closer fit to the measured data than other approximation methods such as polynomials or powers.

The Q-factor was determined from the impedance results according to Equa-

tion 4.10, and is shown in Figure 5.11. The trendline was determined using the previously determined trendline for the real component of impedance and the measured results for the imaginary component of impedance.

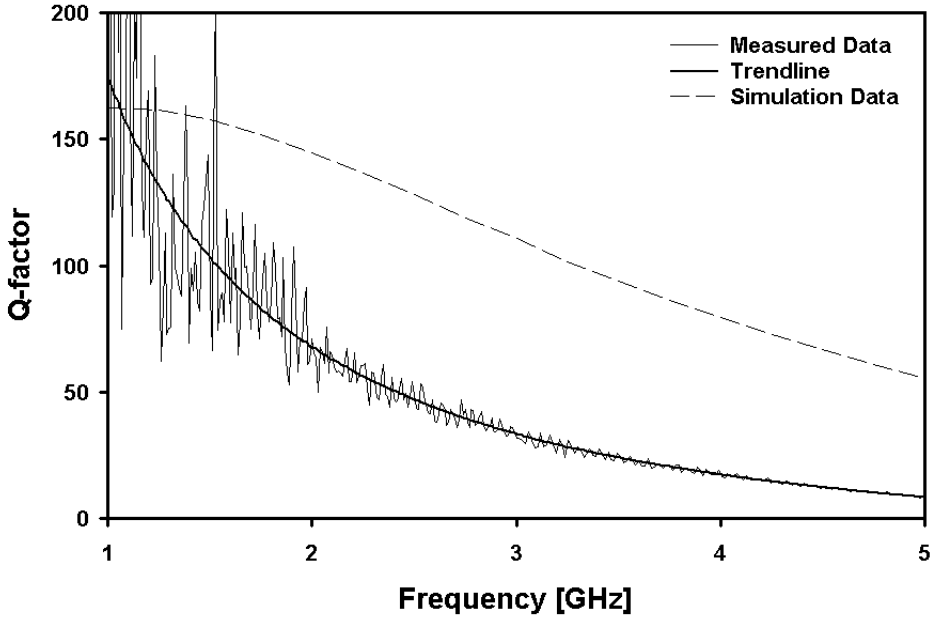

Figure 5.11: Q-factor of capacitor f10.

Since the fabricated capacitors were shorter than those simulated in Chapter 4, a simplified version of capacitor f10 was simulated using HFSS for comparison to measured results. The real component of the impedance is shown in Figure 5.9, the imaginary component of the impedance is shown in Figure 5.10 and the Q-factor is shown in Figure 5.11.

The simulated version had a capacitance gap of 1.6 μm, a beam width of 11.9 μm and an actuator gap of 6.0 μm. The seed layer was 3 μm thick titanium, the metal layer was 97 μm thick nickel, and the substrate was 1 mm thick alumina. The electrical parameters were the same as those used in Chapter 4 (Table 4.4). The simulated capacitor did not include periodic widening of the beam, but it did include the triangular voids in the actuator and capacitor electrodes. The periodic

widening was not included, because the fine detail would result in a large mesh and computation times would be prohibitive.

The simulation results agree reasonably well with the measured results at lower frequencies. At 1 GHz, the measured resistance is 0.97 Ω, the measured reactance is -169.1 Ω and the measured Q-factor is 174.8. The values for the resistance and Q-factor were taken from the trendlines. The values obtained from simulation are 0.91 Ω, -148.2 Ω and 162.4 respectively. At higher frequencies, the measured and simulated values begin to differ. As the frequency increases, the resistance and reactance of the measured device increases faster than predicted during simulation. Also, the Q-factor decreases faster than predicted during simulation.

The measured S_{11} versus frequency is shown in Figure 5.12 for capacitor f10 and the simulated S_{11} versus frequency is shown in Figure 5.13. The S-parameter data was renormalized to 50 Ω for plotting on the Smith chart.

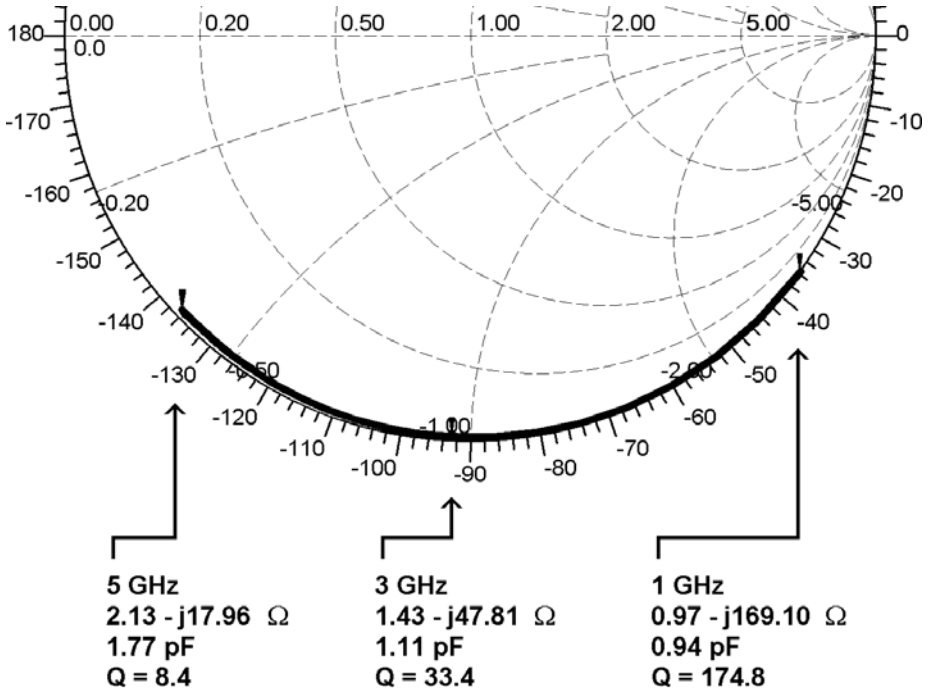

Figure 5.12: Measured S_{11} for capacitor f10.

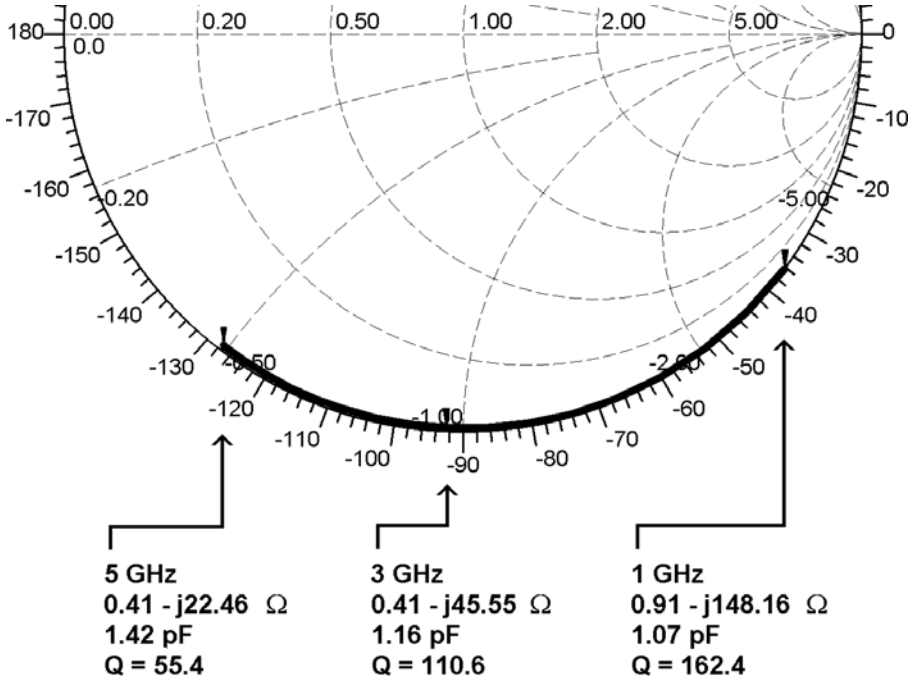

Figure 5.13: Simulated S_{11} for capacitor f10.

Actuation of device f10 was attempted, but it was determined that the beam was still connected to the substrate. Not all of the seed layer beneath the beam had been removed during the etching process. This prevented the beam from deflecting. Additional etching of the devices will be required to electrically isolate the separate structures and to release the beams from the substrate.

The difference between the measured result and the result obtained in simulation, may be due to the following:

1. There is a difference between the way the device is excited during simulations using HFSS, and during testing using microprobes. In simulations, the device is excited through the side of the capacitor. The side profile is used as a port and signals enter and exit this side profile. When testing with microprobes, small fingers are placed on the top of the capacitor and signals enter and exit the capacitor through these small probe fingers. There is a considerable difference between these excitation methods, which has not been fully characterized,

that could lead to a discrepancy in results.

2. During testing, a problem with repeatable contact was observed. The value of the real part of the impedance would differ significantly as the testing procedure was repeated. This could be due to non-optimal excitation of the tall LIGA structures with the microprobes. The microprobes are designed for use on planar circuits and might not be as accurate when using tall LIGA structures. This could be also due to the relatively large measurement spans. Smaller span spot measurements could possibly improve repeatability and reduce large fluctuations in the very small real impedance measurements.

3. The calibration standards used were planar and therefore not ideal for tall LIGA structures. Custom LIGA calibration standards could not have been included on the same mask, since the final height of the structures was unknown.

4. The geometry of capacitor f10 was simplified for simulation. The simplifications are not believed to significantly change the electrical parameters of the capacitor.

6. CONCLUSIONS

6.1 Summary of Work

The goal of this research has been the implementation of high quality MEMS variable capacitors, for frequencies up to and including X-band, that are suitable for fabrication using the LIGA process. To the author's knowledge, no dynamically operating LIGA-MEMS devices for RF applications have been previously reported. Previous efforts have concentrated on static structures such as transmission lines, filters, and couplers. Variable capacitors have been selected since the strengths of the LIGA process are believed to be able to improve the characteristics over previous MEMS variable capacitors. These strengths include large vertical aspect ratios, submicron feature sizes, and thick metal layers. The specific objectives of the research as defined in Chapter 1 are:

1. Review existing MEMS variable capacitor designs and methodologies and determine if any structures or techniques are suitable for fabrication using LIGA. During this review, the fundamental design issues of MEMS devices in general will be noted.

2. Investigate a suitable actuation technique for the LIGA-MEMS variable capacitors and a method to analyze structures using this actuation technique.

3. Design variable capacitors using the actuation technique that are capable of high performance at microwave frequencies. This requires a method for analyzing the high frequency behavior of the capacitors.

4. Fabricate the capacitors, which involves creating a suitable layout of the mask for the devices.

5. Test the capacitors and determine the performance of the capacitors in all figure-of-merit categories and compare against the simulated results.

The first objective was completed by performing a literature review of many existing MEMS variable capacitor designs. MEMS variable capacitors typically fall into one of three categories; parallel plate, lateral comb and shunt mounted. All three types are applicable for fabrication using LIGA and have their own strengths and weaknesses. Most planar parallel plate designs have focused on the lower end of the microwave frequency range (1 - 3 GHz) with capacitance values between approximately 1 and 4 pF. Lateral comb capacitors have been targeted for frequencies in the 100 MHz to 1 GHz frequency range with capacitance values between approximately 1 and 10 pF. To the author's knowledge there are no existing MEMS parallel plate or lateral comb capacitors that are designed for the 3 - 10 GHz frequency region with Q-factors greater than 100. Existing shunt mounted capacitors have been designed for the 10 - 40 GHz region. These capacitors are capable of high Q operation (greater than 100), but have small capacitance values (0.1 - 0.3 pF).

During the literature review, the fundamental design issues of MEMS devices were encountered. Accurate material properties are essential in order to obtain accurate simulation results. LIGA nickel was found to have mechanical properties that vary significantly from bulk nickel. MEMS devices can be subject to accelerations and must be able to perform adequately during these accelerations. The design should not limit them to stationary operation. Stress levels present in a MEMS device during actuation and fabrication are very important. Large stresses during actuation can lead to premature failure of a MEMS device. MEMS devices featuring electrostatic actuation with small gaps are susceptible to the breakdown of air. It has been determined that 65 V/μm should not be exceeded for gaps smaller than 4 μm.

Electrostatic actuation was selected for multiple reasons. These include design simplicity, fast actuation rates, very low (if not zero) power consumption, and no reliance on any special materials. The finite element software package ANSYS is an effective method to analyze MEMS devices that feature electrostatic actuation.

Multiple parallel plate variable capacitors were designed that are capable of high performance at microwave frequencies. The various capacitors were designed to operate at frequencies from approximately 2 - 13 GHz and have Q-factors greater than 200 with nickel device layers and greater than 400 with copper device layers. In addition, various techniques were employed to increase the tuning range of the capacitors. These include three-plate designs, decreased capacitance lengths, and the addition of stoppers. The simulation results suggest that the LIGA process has the potential to create parallel plate variable capacitors that are suitable for frequencies up to and including X-band with high Q-factors (greater than 100). The finite element software package Ansoft HFSS was found to be an effective method for determining the high frequency electromagnetic characteristics of the devices.

The layout for a mask was created which included capacitors with various geometries. In order to increase the probability of successfully fabricated devices, two changes were made to the simulated capacitors of Chapter 4. The beam was widened periodically and triangular voids were added to the actuator and capacitance electrodes. The Institute for Microstructure Technology, Forschungszentrum Karlsruhe fabricated the capacitors. It was decided that for an initial attempt, 100 μm tall structures would be fabricated since these devices are very challenging to fabricate due to the required high aspect ratios of the beams and gaps and it was felt that 350 μm might be too ambitious for an initial attempt.

Many devices were lost during the X-ray lithography process and during the electroplating process. It was found that many of the devices that were not deformed had structures that were not electrically isolated. Capacitor f10 was tested and the results compared reasonably well with simulation results at lower frequencies. Differences between measured and simulated results, at higher frequencies, can likely be attributed to differences in excitations, non-optimal excitation of the tall LIGA structures with the microprobes, non-optimal calibration standards, and simplified simulation geometries. The capacitors require additional etching to release the beams from the substrate so that actuation can be attempted.

6.2 Recommendations for Further Study

The following research should be completed to more thoroughly investigate the subject:

1. The source or sources of the difference between simulated and measured results at higher frequencies should be determined. Smaller span spot measurements could possibly improve repeatability and reduce fluctuations in the real impedance and Q-factor.

2. Additional etching of the capacitors should be performed and the change in impedance with the application of an actuation voltage should be measured.

3. Other capacitor types such as lateral comb and shunt mounted configurations could be designed for the LIGA process to determine if LIGA offers an advantage for these configuration types.

4. In order to integrate tall LIGA structures with traditional planar structures, efficient LIGA-planar transitions should be designed and tested. This could possibly aid in testing as conventional planar testing procedures could be used.

REFERENCES

[1] J.J. Yao, "RF MEMS from a device perspective," *Journal of Micromechanics and Microengineering*, vol. 10, pp. R9–R38, December 2000.

[2] Hector J. De Los Santos, *Introduction to Microelectromechanical (MEM) Microwave Systems*. Boston, MA: Artech House, 1999.

[3] J.H. Comtois, V.M. Bright, and M.W. Phipps, "Thermal microactuators for surface-micromachining processes," *Proceedings of SPIE - The International Society for Optical Engineering*, vol. 2642, pp. 10–21, 1995.

[4] D.J. Young and B.E. Boser, "A Micromachined Variable Capacitor for Monolithic Low-Noise VCOs," in *Solid State Sensor and Actuator Workshop*, (Hilton Head, SC), pp. 86–89, 1996.

[5] A. Dec and K. Suyama, "Micromachined electro-mechanically tunable capacitors and their applications to RF IC's," *IEEE Transactions on Microwave Theory and Techniques*, vol. 46, pp. 2587–2596, 1998.

[6] J. Jou, C. Liu, and J. Schutt-Aine, "Development of a wide tuning range two-parallel-plate tunable capacitor for integrated wireless communication systems," *International Journal of RF and Microwave Computer Aided Design*, vol. 11, pp. 322–329, 2001.

[7] J. Yao, S. Park, and J. DeNatale, "High tuning ratio MEMS based tunable capacitors for RF communications applications," in *Solid State Sensor and Actuator Workshop*, (Hilton Head, SC), pp. 124–127, 1998.

[8] R.L. Borwick III, P.A. Stupar, J. DeNatale, R. Anderson, C. Tsai, K. Garrett, and R. Erlandson, "A high Q, large tuning range MEMS capacitor for RF filter systems," *Sensors and Actuators, A: Physical*, vol. 103, pp. 33–41, 2003.

[9] Z. Feng, H. Zhang, K.C. Gupta, W. Zhang, V.M. Bright, and Y.C. Lee, "MEMS-based series and shunt variable capacitors for microwave and millimeter-wave frequencies," *Sensors and Actuators, A: Physical*, vol. 91, pp. 256–265, 2001.

[10] L. Dussopt and G.M. Rebeiz, "High-Q millimeter-wave MEMS varactors: Extended tuning range and discrete-position designs," in *IEEE MTT-S International Microwave Symposium Digest*, pp. 1205–1208, 2002.

[11] E.W. Becker, W. Ehrfeld, D. Münchmeyer, H. Betz, A. Heuberger, S. Pongratz, W. Glashauser, H.J. Michel, and R.v. Siemens, "Production of separation nozzle system for uranium enrichment by a combination of X-ray lithography and galvanoplastics," *Naturwissenschaften*, vol. 69, pp. 520–523, November 1982.

[12] E.W. Becker, W. Ehrfeld, P. Hagmann, A. Maner, and D. Münchmeyer, "Fabrication of microstructures with high aspect ratios and great structural heights by synchrotron radiation lithography, galvanoforming, and plastic moulding (LIGA process)," *Microelectronic Engineering*, vol. 4, pp. 35–36, May 1986.

[13] http://presse.fzk.de/aktuelles/bilderdienst/bilder/bild9.gif.

[14] http://presse.fzk.de/aktuelles/bilderdienst/bilder/bild11.gif.

[15] T.L. Willke and S.S. Gearhart, "LIGA micromachined planar transmission lines and filters," *IEEE Transactions on Microwave Theory and Techniques*, vol. 45, pp. 1681–1688, 1997.

[16] K.Y. Park, J.C. Lee, J.H. Kim, B. Lee, N.Y. Kim, J.Y. Park, G.H. Kim, J.U. Bu, and K.W. Chung, "A new three-dimensional 30 GHz bandpass filter using the LIGA micromachined process," *Microwave and Optical Technology Letters*, vol. 30, pp. 199–201, 2001.

[17] A.A. Kachayev, D.M. Klymyshyn, S. Achenbach, and V. Saile, "High vertical aspect ratio LIGA microwave 3-dB coupler," in *International Conference on MEMS, NANO and Smart Systems*, pp. 38–43, 2003.

[18] J.R. Davis, *Metals Handbook: Desk Edition*. Materials Park, OH: ASM International, second ed., 1998.

[19] E. Mazza, S. Abel, and J. Dual, "Experimental determination of mechanical properties of Ni and Ni-Fe microbars," *Microsystem Technology*, vol. 2, pp. 197–202, 1996.

[20] W.Sharpe, D.Lavan, and R.Edwards, "Mechanical Properties of LIGA-deposited nickel for MEMS," in *International Conference on Solid State Sensors and Actuators*, pp. 607–610, 1997.

[21] T.Bucheit, T.Christenson, D.Schmale, and D.Lavan, "Understanding and tailoring the mechanical properties of LIGA fabricated materials," in *MRS Symposium Proceedings*, vol. 546, pp. 121–126, 1998.

[22] L.S. Stephens, K.W. Kelly, S. Simhadri, A.B. McCandless, and E.I. Meletis, "Mechanical property evaluation and failure analysis of cantilevered LIGA nickel microposts," *Journal of Microelectromechanical Systems*, vol. 10, pp. 347–359, September 2001.

[23] J.M. Gere and S.P. Timoshenko, *Mechanics of Materials*. Boston, MA: PWS Publishing Company, fourth ed., 1997.

[24] P.M. Osterberg and S.D. Senturia, "M-TEST: a test chip for MEMS material property measurement using electrostatically actuated test structures," *Journal of Microelectromechanical Systems*, vol. 6, pp. 107–118, June 1997.

[25] S.O. Kasap, *Materials Science and Engineering: First Principles and Design, Revised Edition, An Elementary Course for Engineers, Materials Scientists and Engineering Physicists, Special Custom Published Textbook*. Saskatoon, SK: University of Saskatchewan Printing Services, 1996.

[26] H.S. Cho, K.J. Hemker, K. Lian, J. Goettert, and G. Dirras, "Measured mechanical properties of LIGA Ni structures," *Sensors and Actuators, A: Physical*, vol. 103, pp. 59–63, 2003.

[27] J.L. Everhart, *Engineering Properties of Nickel and Nickel Alloys*. New York, NY: Plenum Press, 1971.

[28] ANSYS Version 7.0, ANSYS, Inc., Southpointe, 275 Technology Drive, Canonsburg, PA 15317.

[29] ANSYS 7.0 Documentation, ANSYS, Inc. Theory Reference.

[30] P.G. Slade and E.D. Taylor, "Electrical breakdown in atmospheric air between closely spaced (0.2 μm-40 μm) electrical contacts," *IEEE Transactions on Components and Packaging Technologies*, vol. 25, pp. 390–396, September 2002.

[31] R.T. Lee, H.H. Chung, and Y.C. Chiou, "Arc erosion behaviour of silver electric contacts in a single arc discharge across a static gap," *IEE Proceedings: Science, Measurement and Technology*, vol. 148, pp. 8–14, January 2001.

[32] J.M. Torres and R.S. Dhariwal, "Electric field breakdown at micrometre separations," *Nanotechnology*, vol. 10, no. 1, pp. 102–107, 1999.

[33] K.E. Petersen, "Dynamic Micromechanics on Silicon: Techniques and Devices," *IEEE Transactions on Electron Devices*, vol. ED-25, pp. 1241–1250, October 1978.

[34] R. Anderson, *Fundamentals of vibrations*. New York, NY: Macmillan, 1967.

[35] W.S. Best, A. Karnik, and J. Parkes, "Integrated Design and Simulation of RF-MEM Devices." Coventor presentation, January 2002.

[36] E.S. Hung and S.D. Senturia, "Tunable Capacitors with Programmable Capacitance-Voltage Characteristic," in *Solid State Sensor and Actuator Workshop*, (Hilton Head, SC), pp. 292–295, 1998.

[37] Coventor, Inc., 4001 Weston Parkway, Cary, NC 27513.

[38] J.R. Gilbert, R. Legtenberg, and S.D. Senturia, "3D Coupled Electro-Mechanics for MEMS: Applications of CoSolve-EM," in *Proceedings of MEMS*, (Amsterdam), pp. 122–127, 1995.

[39] ANSYS 7.0 Documentation, ANSYS, Inc. Verification Manual.

[40] Ansoft HFSS Version 8.5, Ansoft Corporation, 225 West Station Square Drive, Suite 200, Pittsburgh, PA 15219.

[41] S. Moaveni, *Finite Element Analysis: Theory and Application with ANSYS*. Upper Saddle River, NJ: Prentice Hall, 1999.

[42] T. Itoh, *Numerical Techniques for Microwave and Millimeter-Wave Passive Structures*. New York, NY: John Wiley and Sons, Inc., 1989.

[43] J.B. Muldavin and G.M. Rebeiz, "High-isolation CPW MEMS shunt switches - Part 1: modeling," *IEEE Transactions on Microwave Theory and Techniques*, vol. 48, pp. 1045–1052, June 2000.

[44] P.M. Zavracky, S. Majumder, and N.E. McGruer, "Micromechanical switches fabricated using nickel surface micromachining," *Journal of Microelectromechanical Systems*, vol. 6, pp. 3–9, March 1997.

[45] E.S. Hung and S.D. Senturia, "Extending the travel range of analog-tuned electrostatic actuators," *Journal of Microelectromechanical Systems*, vol. 8, pp. 497–505, December 1999.

[46] W. Menz, J. Mohr, and O. Paul, *Microsystem Technology*. Verlag GmbH: Wiley-vch, 2001.

[47] A. Kachayev, "LIGA-Micromachined Tight Microwave Couplers," M.Sc., University of Saskatchewan, Saskatoon, Saskatchewan, Fall 2003.

[48] D.M. Pozar, *Microwave Engineering*. New York, NY: John Wiley and Sons, Inc., second ed., 1998.

[49] Ansoft HFSS 8.5 Documantation, Technical Notes.

[50] PUFF Version 2.0, Computer aided design for microwave integrated circuits, R. Compton and D. Rutledge, Cornell University, Ithaca, NY, 1991.